

# **Potential vorticity anomalies related to clouds and precipitation in extratropical cyclones**

A thesis submitted to attain the degree of  
Doctor of Sciences of ETH Zurich  
(Dr. Sc. ETH Zurich)

presented by

Bas Crezee  
MSc in Physics and Climate Science, Utrecht University  
born on 24 February 1988  
citizen of The Netherlands

accepted on the recommendation of

Prof. Dr. Heini Wernli, examiner  
Dr. Hanna Joos, co-examiner  
Dr. Gwendal Rivière, co-examiner

2017



# CONTENTS

---

Abstract

Zusammenfassung

- 1 Introduction 1
  - 1.1 The potential vorticity perspective 2
  - 1.2 Diabatic heating and cyclone intensification 5
  - 1.3 Microphysics and dynamics 8
  - 1.4 Aims and outline 11
- 2 Methods 13
  - 2.1 COSMO model 13
    - 2.1.1 Numerics, dynamics and initialization 14
    - 2.1.2 Microphysical heating rates 14
    - 2.1.3 Below-cloud and in-cloud process categories 17
    - 2.1.4 Other physical parameterizations 18
  - 2.2 LAGRANTO trajectory model 20
  - 2.3 Lagrangian PV budget 22
- 3 Cloud diabatic PV anomalies in an idealized extratropical cyclone 25
  - 3.1 Introduction 25
  - 3.2 Model setup 27
  - 3.3 Cyclone development 30
  - 3.4 Cloud diabatic PV budgets 32
    - 3.4.1 Total cloud diabatic PV across the warm front 32
    - 3.4.2 Detailed structure across the warm front 34
    - 3.4.3 Microphysical processes contributing to the individual anomalies 39
    - 3.4.4 Temporal evolution of diabatic PV rates of selected anomalies 42
  - 3.5 Summary and discussion 43
- 4 Cloud diabatic PV anomalies in a strong maritime extratropical cyclone 49
  - 4.1 Introduction 49
  - 4.2 Model setup 52
  - 4.3 Cyclone development 53
    - 4.3.1 Synoptic evolution 53
    - 4.3.2 Microphysical evolution 56
  - 4.4 Frontal wave stage (C1) 59
    - 4.4.1 Warm front structure 62
    - 4.4.2 Cold front structure 68

4.4.3 CDPV anomalies	74
4.5 Time evolution (C1-C3)	87
4.5.1 Cyclone structure	88
4.5.2 CDPV anomalies	91
4.5.3 How different is the Lagrangian perspective from the Eulerian perspective?	103
4.6 Comparison to the idealized cyclone	110
4.6.1 Warm front structure	111
4.6.2 CDPV anomalies	113
4.6.3 A conceptual understanding of the complex frontal mesoscale PV patterns	115
4.7 Summary	118
<b>5 Summary</b>	<b>121</b>
5.1 How important are below-cloud processes like rain evaporation, snow melting and snow sublimation for the positive and negative PV anomalies?	121
5.2 Can the mesoscale PV structure at the fronts be explained by the microphysical processes?	122
5.3 What is the general evolution of the positive and negative anomalies over time?	123
5.4 Do we require the Lagrangian perspective to answer the above questions?	124
<b>6 Final remarks &amp; outlook</b>	<b>127</b>
6.1 Final remarks	127
6.2 Outlook	128
<b>A On the role of cross-isentropic transport for the PV anomalies</b>	<b>131</b>
<b>B Another application of our method: stratosphere-troposphere exchange</b>	<b>141</b>
<b>C Additional figures</b>	<b>149</b>
<b>Bibliography</b>	<b>151</b>
<b>Acknowledgements</b>	<b>161</b>
<b>Curriculum Vitae</b>	<b>163</b>

# ABSTRACT

---

Different microphysical processes influence the dynamics of cyclones by their associated latent heating or cooling, which modifies potential vorticity (PV) from the boundary layer to slightly above the tropopause level. A new method is developed based on integrating diabatic PV changes along backward trajectories. This method allows us to decompose the Lagrangian PV change over a certain time interval into contributions from different microphysical processes, including the below-cloud processes snow sublimation, snow melting and rain evaporation. The method is first applied to an extratropical cyclone in an idealized baroclinic channel setup. The mesoscale PV structure along the bent-back front results from a complex combination of microphysical processes. The microphysical contributions to the different positive and negative anomalies are analyzed in detail. It is found that for each anomaly, typically one specific microphysical process takes the leading role in its diabatic generation. A large but rather weak low and mid-level positive anomaly is produced by depositional growth of ice and snow. Two smaller but stronger positive anomalies at lower levels are generated mainly by in-cloud condensational heating at the warm front, and below-cloud rain evaporation and snow melting 200 km further north. In addition, near-surface negative anomalies are produced by snow melting and snow sublimation, respectively.

The same method is applied to a particularly strong maritime extratropical cyclone, occurring over the Bering Sea on 12-14 December 2015. The warm-frontal structure is characterized by one strong positive PV anomaly stretching from the surface almost up to the tropopause. For this anomaly, condensation and below-cloud rain evaporation contribute most in the lower part, whereas deposition of ice and snow are more important in the upper part. Snow melting contributes very strongly in a localized region at the surface front. Snow sublimation leads to a weak negative anomaly on the cold side of the front. The cold frontal structure was found to be characterized by two strong low-level positive PV anomalies. The one on the warm side is produced due to condensation and below-cloud rain evaporation, the one on the cold side, located outside the clouds, has contributions from almost all microphysical processes. The time evolution of the anomalies showed that positive anomalies vary most over time, whereas negative anomalies stay relatively constant. The transition of the cyclone to a situation where it is embedded in a colder environment is marked by an increasing relative

importance of the ice-phase processes compared to the liquid phase processes. The general findings of this study are: (a) a complex combination of microphysical processes dictates the strength and structure of diabatic PV anomalies along the fronts; (b) below-cloud processes are relevant for both the positive and negative anomalies throughout most of the troposphere; and (c) the Lagrangian approach proved meaningful for this detailed process-based analysis of dynamically relevant mesoscale flow structures. With regard to the below-cloud process, we note their strong contributions up to 1.0 PVU to the positive low-level anomalies, their relevance for anomalies in both the warm sector (mainly rain evaporation) and the cold sector (mainly rain evaporation and snow sublimation), and the importance of snow melting in localized regions close to the surface front. Furthermore, it is shown that in the mid troposphere both the integrated diabatic PV tendencies (Lagrangian anomalies) and consideration of cross-isentropic transport in a background with a vertical PV gradient are important to understand the resulting PV anomalies. Idealized modelling has the potential to further distinguish the inherently linked effects of Lagrangian PV modification and cross-isentropic transport of low-PV air. Finally, it is shown how our novel method could lead to a better understanding of the pathways of stratosphere-troposphere exchange and the involved physical processes.

# ZUSAMMENFASSUNG

---

Verschiedene mikrophysikalische Prozesse beeinflussen die Dynamik von Zyklonen durch latentes Heizen oder Kühlen, das die potentielle Vortizität (PV) von der Grenzschicht bis knapp über die Tropopause modifizieren kann. In dieser Arbeit wurde eine neue Methode entwickelt, welche diabatische PV-Änderungen entlang von Rückwärtstrajektorien untersucht. Mithilfe dieser Methode, können Lagrangesche PV-Änderungen über ein bestimmtes Zeitintervall in Beiträge verschiedener mikrophysikalischer Prozesse unterteilt werden. Dazu gehören auch Prozesse, welche unterhalb der Wolken auftreten, wie Sublimieren und Schmelzen von Schnee und Verdunstung von Regen.

Die Methode wurde zuerst auf eine extratropische Zyklone in einem idealisierten baroklinen Kanal angewendet. Die mesoskalige PV-Struktur entlang der Bent-back-Front resultiert aus einer komplexen Kombination von mikrophysikalischen Prozessen. Typischerweise ist für jede Anomalie ein Prozess hauptverantwortlich. Eine grosse aber eher schwache positive Anomalie auf tiefen und mittleren Höhen wird durch Depositionswachstum von Eis und Schnee produziert. Zwei kleinere aber stärkere positive tiefgelegene Anomalien werden hauptsächlich durch Kondensationsheizen in den Wolken an der Warmfront generiert, sowie durch Regenverdunstung und Schneeschmelzen unterhalb der Wolken etwa 200 km weiter nördlich. Negative Anomalien nahe der Oberfläche wurden durch Schneeschmelzen und Schneesublimation produziert.

Die gleiche Methode wird auf eine besonders starke maritime extratropische Zyklone angewendet, welche vom 12. bis 14. Dezember 2015 über dem Beringmeer auftrat. Die Warmfront-Struktur der Zyklone wird durch eine einzige starke positive PV-Anomalie charakterisiert, welche sich von der Oberfläche bis fast zur Tropopause erstreckt. Zum unteren Teil dieser Anomalie trugen Kondensation und Regenverdunstung unterhalb der Wolken am meisten bei, während für deren oberen Teil vor allem Depositionswachstum von Eis und Schnee wichtig sind. Schneeschmelzen trägt sehr stark in einer lokalisierten Region an der Bodenfront bei. Schneesublimation führt zu einer schwachen negativen Anomalie auf der kalten Seite der Kaltfront. Die Kaltfront-Struktur der Zyklone wird durch zwei starke tiefgelegene PV-Anomalien charakterisiert. Diejenige auf der warmen Seite wird durch Kondensation und Regenverdunstung unterhalb der Wolken produziert, diejenige auf der kalten Seite, welche ausserhalb der Wolken liegt, beinhaltet Beiträge von fast allen mikrophysikalischen Prozessen. Die zeitliche

Entwicklung der Anomalien zeigt, dass sich die positiven Anomalien über die Zeit am meisten verändern, während die negativen Anomalien relativ konstant bleiben. Die Bewegung der Zyklone in eine kältere Umgebung führt dazu, dass die Eisphasen-Prozesse im Vergleich zu den Flüssigphasen-Prozessen an Wichtigkeit gewinnen.

Die allgemeinen Erkenntnisse dieser Arbeit sind: (a) ein komplexes Zusammenspiel verschiedener mikrophysikalischer Prozesse legt die Stärke und Struktur von diabatischen PV-Anomalien entlang der Fronten fest; (b) Prozesse unterhalb der Wolken sind in einem Grossteil der Troposphäre sowohl für die positiven als auch für die negativen Anomalien relevant; und (c) der Lagrangesche Ansatz erweist sich als eine sinnvolle Art und Weise, um diese dynamisch relevanten Anomalien auf Prozess-Ebene zu analysieren. Nennenswert sind zudem die starken Beiträge von bis zu 1.0 PVU derjenigen Prozesse, welche unterhalb der Wolken auftreten. Dazu gehört die Relevanz für die Anomalien im Warm-Sektor (Regenverdunstung) und im Kalt-Sektor (Regenverdunstung und Schneesublimation) sowie die Bedeutung von Schneeschmelzen in lokalisierten Gebieten nahe der Bodenfront.

Ausserdem wird gezeigt, dass in der mittleren Troposphäre sowohl die integrierten diabatischen PV-Tendenzen (die Lagrangeschen Anomalien) als auch die Berücksichtigung von Transport durch die Isentropen in einem Feld mit einem vertikalen PV-Gradienten wichtig sind, um die resultierenden PV-Anomalien zu verstehen. Idealisierte Modellsimulationen haben das Potential, zwischen den von Natur aus gekoppelten Effekten von Lagrangescher PV-Modifikation und Transport von Luft mit tiefer PV durch die Isentropen zu unterscheiden. Schliesslich wird gezeigt wie die neu entwickelte Lagrangesche Methode zu einem besseren Verständnis von Stratosphären-Troposphären-Austausch und den involvierten physikalischen Prozessen führen kann.



# 1

## INTRODUCTION

---

Weather forecasts have drastically improved during the last decades with a 5-day forecast today being as reliable as a 3-day forecast 30 years ago (Bauer et al., 2015). This “quiet revolution of numerical weather prediction” occurred thanks to increases in computational power (Bauer et al., 2015), increased use of weather observations (Simmons and Hollingsworth, 2002) and advances in incorporating more physical processes into the models (e.g. Arakawa, 2004). The latter lead to the development of models with increasing complexity, making it more difficult to understand model behaviour. Maybe our conceptual understanding sometimes lags behind the fast numerical advances, which made it possible to forecast weather further in advance and in greater detail. As Davis and Emanuel (1991) put it: “a proper integration of the equations of motion is not synonymous with a conceptual grasp of the phenomena being predicted”. To improve our conceptual understanding one can focus on one certain physical process and study its impact in a detailed case study of a certain weather system.

In this thesis the broad aim is to improve our conceptual understanding of the influence of different microphysical processes on extratropical cyclones. These storm systems affect mid-latitude weather through the accompanying winds and strong precipitation. Even though their formation can be understood through dry baroclinic instability, it is well established that moist processes enhance cyclogenesis (Uccellini, 1990). During the past years, there is a growing body of evidence, that not solely condensational heating, but also other in-cloud heating processes and even below-cloud cooling processes can have an important influence on the dynamics of a cyclone and its fronts (e.g. Joos and Wernli, 2012; Igel and Heever, 2014; Coronel et al., 2015).

This introductory chapter starts with section 1.1 where potential vorticity (PV) is introduced and explained why the so-called “PV framework” is so useful in this study. Section 1.2 gives a brief historical overview on our understanding of cyclone intensification and is followed by a section presenting studies that looked at the role of microphysical processes in cyclones and their associated fronts. The introduction concludes with presenting the main aims of this thesis and an outline of its content.

## 1.1 The potential vorticity perspective

In this section a brief overview of the potential vorticity (PV) perspective will be given, for a more extensive description, the reader is referred to Hoskins et al. (1985). The importance of circulation and vorticity in both the ocean and atmosphere was already recognized by Bjerknes (1902). Further developments of Bjerknes' concepts were done by Rossby (1940). Using a barotropic model - a model where density only depends on pressure - he derived that:

$$\frac{D}{Dt} \frac{\zeta_a}{h} = 0 \quad (1.1)$$

where  $\frac{D}{Dt}$  is the material derivative, which means that the absolute vorticity  $\zeta_a$  divided by the depth  $h$  of the fluid column is conserved following the flow. Extending this to a baroclinic model, consisting of a number of layers having constant potential temperature  $\Theta$ , Rossby showed that, for adiabatic frictionless motion:

$$\frac{D}{Dt} \frac{f + \zeta_\Theta}{\Delta} = 0 \quad (1.2)$$

where  $f$  is the planetary vorticity and  $\Delta$  is the mass per unit area. Rossby originally named the quantity  $\zeta_\Theta$  the potential vorticity, being the vorticity that a parcel would have when it is moved to a certain reference latitude and standard value of mass per unit area, equivalent to potential temperature as the temperature a parcel would attain when moved to a standard pressure. Later, the whole term on which the material derivative operates in Eq. 1.2 got named the potential vorticity or PV. This quantity being conserved means that moving a parcel in an adiabatic and frictionless flow, there is the potential to create vorticity through a change of latitude ( $f$ ) or through changing the separation of isentropic layers. Independently from Rossby, Ertel (1942) derived an even more general form of eq.1.2 as:

$$PV = \frac{\zeta_a \cdot \nabla \Theta}{\rho} \quad (1.3)$$

where  $\rho$  denotes air density.  $PV$  is materially conserved for three-dimensional non-hydrostatic motion, it is this *conservation principle* that makes PV a very powerful quantity for atmospheric dynamics. In addition, the incorporation of diabatic and frictional effects, and how they locally change the PV, is straightforward (Ertel, 1942):

$$\frac{D}{Dt} PV = \frac{\zeta_a \cdot \nabla \dot{\Theta}}{\rho} + \frac{\mathbf{K} \cdot \nabla \Theta}{\rho} \quad (1.4)$$

where  $\dot{\Theta}$  is the diabatic heating rate and  $\mathbf{K}$  is the frictional-force curl. It is the first term on the r.h.s. of eq. 1.4 that is important in this thesis, since it

allows to calculate PV changes from the heating and cooling due to microphysical processes.

Kleinschmidt (1957) was the first to show that from the PV field one can deduce the wind, pressure and potential temperature fields, for a few specific cases. With the development of quasi-geostrophic theory by Charney and Stern (1962), a more general form of the invertibility principle was achieved. The invertibility principle states that given proper boundary conditions, and a suitable balance condition, knowing the three-dimensional interior PV distribution is enough to derive the three-dimensional interior temperature and balanced wind fields. A balance condition is considered suitable for a certain study when the flow is indeed in balance (no convective instability or symmetric instability), and when the motions considered occur at scales that do not violate the assumptions of the balance condition. See Davis (1992b) for a comparison of different PV inversion techniques, including the method of static piecewise PV inversion, which allows one to quantify the relative contributions of different PV anomalies to the surface circulation.

This *invertibility principle* together with the *conservation principle* (eq. 1.3) and the possibility to quantify the effects of non-conservative processes like cloud diabatic heating or cooling (eq. 1.4), make PV the perfect quantity for studying the influence of microphysical processes on the dynamics of extratropical cyclones. Even though in this thesis no actual inversion is applied, the strength of our method relies on this principle. It allows us to solely look at the PV field and its microphysical contributions for studying the dynamical impact of different microphysical processes on the cyclone.

## 1.2 Diabatic heating and cyclone intensification

Manabe (1956) and Kleinschmidt (1957) were among the first to recognize the importance of condensational heating in cyclone intensification. Manabe (1956) estimated PV changes for two different precipitating systems and found that the strongest precipitating system was related with the largest PV changes. Kleinschmidt (1957) stressed the importance of the diabatically produced PV by calling this the “producing mass” of baroclinic cyclones.

Anthes et al. (1983) showed with sensitivity studies the importance of latent heating for both the minimum pressure and track of an explosive marine cyclone. Hoskins and Berrisford (1988) and Whitaker et al. (1988) both used the PV perspective in case studies, showing how strong cyclone intensification occurs when upper-level PV maxima move over low-level diabatically produced PV. Snyder and

Lindzen (1991) showed in an idealized model with convective parameterization, that under certain circumstances, diabatically produced PV can act as a surrogate for potential vorticity gradients. They observed a similar development to a dry baroclinic wave whereas no meridional PV gradient was present in the basic state. Similarly, Montgomery and Farrell (1991) showed that in certain regimes, latent heating is *required* for cyclogenesis to occur.

Through using the piecewise PV inversion technique Davis and Emanuel (1991) were able to quantify that the low-level positive PV produced by condensational heating explained about 40% of the total cyclonic circulation in the storm during its mature stage. In another case study (Davis, 1992a) this was only 20%, whereas upper-level PV and the low-level temperature anomaly contributed with 30% and 50%, respectively. Huo et al. (1999) found similar results. Using dropsonde and aircraft observations of a strong North Atlantic cyclone, Neiman et al. (1993) estimated low-level PV values up to 6 PVU locally along the bent-back front. Kuo et al. (1991) showed in a numerical case study the importance of latent

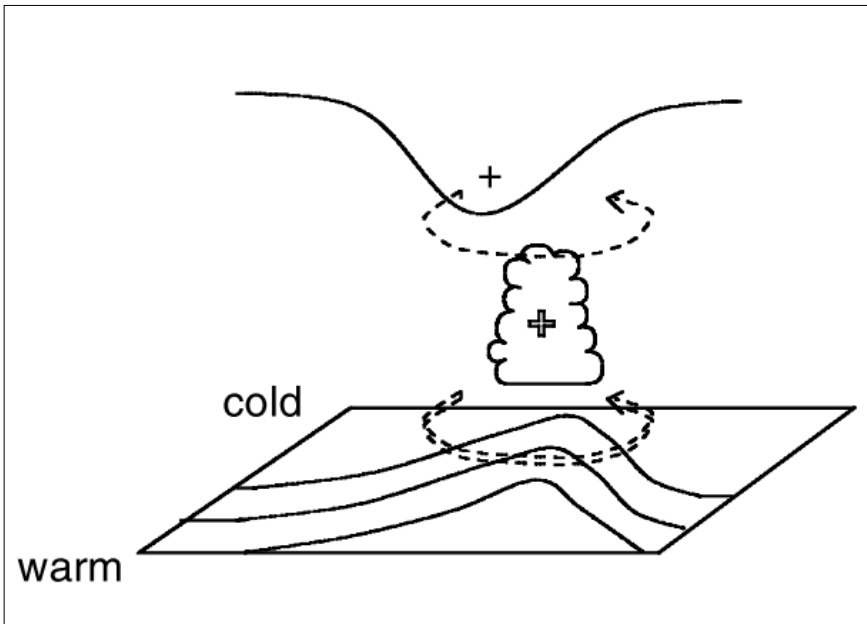


Figure 1.1: The concept of mutual interaction between three different anomalies: an upper-level PV anomaly of stratospheric origin (indicated with + at the top), a surface potential temperature anomaly (indicated with isentropes at the bottom) and a low-level diabatic PV anomaly (indicated with + in the clouds). The figure is taken from Ahmadi-Givi et al. (2004)

heating for cyclone intensification, and stressed the non-linear relation between dry dynamics and latent heat release. Ahmadi-Givi et al. (2004) looked in detail how the different diabatic anomalies interact and showed in a case study that the upper-level PV anomaly was responsible for initiating cyclogenesis, but the low-level positive PV anomaly was crucial in the intensification phase of the cyclone. The concept of mutual interaction is depicted schematically in Fig. 1.1. An upper-level PV anomaly overlies a low-level baroclinic zone and leads to the development of a surface potential temperature anomaly. The diabatically produced low-level PV anomaly enhances the cyclonic circulation and thereby advects the surface potential temperature anomaly northwards and the upper-level PV anomaly further southwards. Stoelinga (1996) found that the low-level diabatic PV anomaly in the simulated cyclone contributed about 70% to the surface winds. In addition, he showed how this low-level anomaly could couple to the upper-level PV anomaly thereby accelerating the propagation of the surface wave and slowing down the propagation of the upper-level wave. This coupling and the so-called formation of a PV tower has been studied in several other case studies (e.g. Reed et al., 1992; Rossa et al., 2000; Wernli et al., 2002). In a climatological study, Binder et al. (2016) showed the relevance of the warm conveyor belt (e.g. Browning et al., 1973; Harrold, 1973; Carlson, 1980; Wernli, 1997; Madonna et al., 2014) as a PV producer for these PV towers and found that explosively deepening cyclones are often characterized by a strong warm conveyor belt ascending close to the cyclone center.

In summary, both observational, modelling and climatological studies have shown the diabatic origin of the low-level PV anomaly, and its relevance for both surface wind fields and the evolution of the cyclone. However, most studies that looked into the origin of the low-level positive PV, used relatively simple microphysical schemes, without representing ice microphysics and/or below-cloud cooling processes. Also, few studies so far looked in detail at the different microphysical contributions involved in the low-level diabatic PV modification, even though there is plenty of evidence that below-cloud processes can be important for the evolution of a cyclone and its accompanying fronts as will be shown in the next section.

### 1.3 Microphysics and dynamics

Clough and Franks (1991), using a two-dimensional model, showed that snow sublimation is essential in keeping mesoscale frontal downdrafts saturated, thereby further enhancing descent through diabatic cooling. Parker and Thorpe

(1995) found that snow sublimation can significantly enhance the cross frontal circulation. Clough et al. (2000) highlighted the relevance of cooling through snow sublimation for the mesoscale structure of the cyclone and suggested that the microphysical parametrizations are important for the detail of the cyclone structure. Forbes and Hogan (2006) found that an underestimation of the cooling due to snow sublimation in fronts can lead to significant forecast errors.

Further, Szeto et al. (1988a) and Szeto et al. (1988b) showed that snow melting needs to be incorporated to understand mesoscale dynamics in both winter and summer storms. The snow melting induced circulations have the potential to influence surface wind speeds by several meters per second. Barth and Parsons (1996) showed that cooling due to both snow sublimation and snow melting deepens the cold air mass behind the cold front and thereby enhances the cold frontal circulation.

Huang and Emanuel (1991) investigated how cooling due to rain evaporation strengthens the frontal circulation to the north of the warm front and leads to a faster collapse of the surface gradients.

Whereas the above mentioned studies looked in detail at the dynamical effects of a single microphysical process, Joos and Wernli (2012) quantified the importance of several microphysical processes on the evolution of the PV along and below a warm conveyor belt in a North Atlantic cyclone. They found that besides condensational heating, also depositional growth of ice and snow contributed significantly to the PV maximum along the warm conveyor belt. In addition, they found that sublimating or evaporating hydrometeors below the warm conveyor belt modifies PV as well. Igel and Heever (2014) looked at the contributions of different microphysical processes to warm frontogenesis. They found that condensational heating tends to reduce the slope of the warm frontal isentropic surface, and thereby to a first order weakens the warm front. Dearden et al. (2016) showed that ice depositional growth contributed significantly to the deepening of two summertime cyclones, and how this process helps the formation of a PV tower.

Microphysical processes are also hypothesized to be important for sting jets. Sting jets are strong local low level jets that are potentially damaging (Browning, 2004). Cyclones that are prone to developing a sting jet, follow the conceptual model of Shapiro and Keyser (1990), and the sting jet emanates from the tip of the bent-back front in the frontal-fracture region (Schultz and Sienkiewicz, 2013). The importance of microphysical processes for sting jets is two-fold. On the one hand, several studies have hypothesized the importance of evaporative

cooling in bringing down high-momentum air towards the surface. Browning et al. (2015) showed this effect using Doppler radar observations, and used a model to confirm that this high momentum air originated from a sting jet. This observational finding is consistent with the occurrence of evaporative cooling along trajectories constituting the sting jet by Martínez-Alvarado et al. (2010). Besides the potential role of microphysics in bringing high-momentum down air to the surface, microphysics might impact the actual development of the sting jet through a different mechanism. Several studies (Clark et al., 2005; Gray et al., 2011; Martínez-Alvarado et al., 2012) have confirmed that downdraught conditional symmetric instability (CSI) occurs in cyclones that produce a sting jet. Those studies diagnosed the occurrence of CSI in cyclones through calculating downdraught slantwise convective available potential energy or DSCAPE (Emanuel, 1994). DSCAPE represents the potential energy available to a parcel undergoing slantwise descent along constant momentum surfaces *assuming* that it remains saturated during its descent through rain evaporation or snow sublimation. Gray et al. (2011) showed that DSCAPE is present in cyclones with sting jets, and not present in equally strong cyclones without a sting jet. This indirectly points at an important role for rain evaporation and snow sublimation in building up the instability (CSI) needed for a sting jet to occur.

## 1.4 Aims and outline

Summarizing the above, there are several studies showing the relevance of various microphysical processes for either frontal dynamics, the warm conveyor belt or sting-jets in an extratropical cyclone. However (a) most of these studies looked at only one single microphysical process, and (b) they focused only at a part of the cyclone, and not at the cyclone as a whole. Therefore, in this thesis we aim for answering the following questions for an extratropical cyclone:

1. Can the mesoscale PV structure along the fronts be explained by the microphysical processes?
2. How important are below-cloud processes like rain evaporation, snow melting and snow sublimation for the positive and negative PV anomalies?
3. Do we require the Lagrangian perspective to answer the above questions?

For answering these questions, a detailed and novel Lagrangian PV budget based on integrating diabatic PV rates along backward trajectories has been developed.

This method and a description of the numerical model are presented in Chapter 2. In Chapter 3 the PV budget method is applied to an idealized extratropical cyclone. The idealized setup serves as a perfect test case for our diagnostics and answers some of our research questions. To see how general the findings in the idealized case are, in Chapter 4, the same method is applied to a real case cyclone. In addition to comparing the results to the idealized case, here also the temporal changes in the diabatic PV budget will be studied. The conclusions are presented in Chapter 5 followed by an outlook in Chapter 6.



# 2

## METHODS

---

This chapter describes the numerical methods that form the basis of Chapters 3 and 4. It starts with section 2.1 on the COSMO model and the different micro-physical parameterizations within this model. In section 2.2 a brief description of the LAGRANTO trajectory model will be given, followed by section 2.3 which explains how the trajectory model is used for constructing a Lagrangian diabatic PV budget.

### 2.1 COSMO model

The **C**onsortium for **S**mall-scale **M**odeling (COSMO) model is a non-hydrostatic limited-area atmospheric model designed for both operational numerical weather prediction as well as scientific applications (Steppeler et al., 2003). In this thesis, two different setups of the COSMO model are used: in Chapter 3 the model is used in an idealized baroclinic channel setup as developed by Schemm et al. (2013), whereas in Chapter 4 the model is setup for a real case study and initialized by and boundary-driven with ECMWF analysis data.

The precise setup of the COSMO model for the idealized and real case will be given in sections 3.2 and 4.2, respectively. The following subsection describes the numerics, dynamics and initialization of the COSMO model, followed by a subsection on the microphysics scheme that is used for both the ideal and real case study. In subsection 2.1.4 the other physical parameterizations that are used in the real case study are described.

#### 2.1.1 *Numerics, dynamics and initialization*

The COSMO model solves the primitive thermo-hydrodynamical equations describing compressible flow in a moist atmosphere and uses several physical parameterizations to include processes that are not resolved at the gridscale or not included in the thermo-hydrodynamical equations. The grid is a rotated geographical Arakawa C-grid (Arakawa and Lamb, 1977) in the horizontal direction. The vertical coordinate system is terrain-following and staggered and the vertical spacing can be specified by the user. For initialization and as lateral boundary conditions the model can be driven by various coarse-grid models (e.g. ECMWF

analysis) or with user-specified idealized fields. For the top boundary condition the model uses a Rayleigh damping layer.

### 2.1.2 Microphysical heating rates

The formation of clouds and precipitation occurs at the subgrid-scale, therefore it needs to be parameterized in the COSMO model. The parameterization used is a one-moment bulk scheme (Doms et al., 2011), which means that only the mass in each category is a prognostic variable. Four different hydrometeor species are included. The liquid phase is represented by cloud water and rain water, whereas the solid phase is represented by the categories cloud ice and snow. Growing ice particles are transferred to the snow category through autoconversion, and similarly, cloud droplets that grow larger in size than  $50 \mu\text{m}$  are converted to the rain category. Whereas cloud ice and cloud water are assumed to have negligible fall velocities, snow and rain have terminal fall velocities that depend on the hydrometeor size. The diabatic heating rates related to the large-scale cloud scheme  $DHR_{cloud}$ , are calculated as follows (Doms et al., 2011):

$$DHR_{cloud} = \frac{L_V}{c_{pd}}(S^c + S^r) + \frac{L_S}{c_{pd}}(S^i + S^s) \quad (2.1)$$

where  $L_V$  and  $L_S$  represent the latent heat of vaporisation and of sublimation, respectively, and the S terms represent the sources and sinks for cloud water (c), rain (r), cloud ice (i) and snow (s). These terms can be split out further as follows:

$$S^c = S_c - S_{frz}^c + S_{melt}^i - S_{rim} + S_{nlh} \quad (2.2)$$

$$S^i = S_{nuc} + S_{frz}^c + S_{dep}^i - S_{melt}^i - S_{aud} - S_{cri}^i + S_{nlh} \quad (2.3)$$

$$S^r = S_{ev} + S_{shed} - S_{cri}^r - S_{frz}^r + S_{melt} + S_{nlh} \quad (2.4)$$

$$S^s = S_{aud} + S_{rim} + S_{dep}^s + S_{cri}^i + S_{cri}^r + S_{frz}^r - S_{melt}^s + S_{nlh} \quad (2.5)$$

The terms  $S_{nlh}$  represents processes that are not associated with latent heating or cooling (e.g., aggregation of cloud ice to form snow). The terms associated with latent heating and latent cooling will be discussed in more detail in the following paragraphs.

**Heating processes** The total depositional growth rate of all ice crystals  $S_{dep}^i$  is a heating process and is given by:

$$S_{dep}^i = c_{dep}^i N_i m_i^{(1/3)} (q^v - q_{si}^v) \quad \text{if } q^v > q_{si}^v \quad (2.6)$$

where  $q^v$  is the specific humidity and  $q_{si}^v$  is the saturation specific humidity with respect to ice,  $c_{dep}^i$  is a constant.  $N_i$  is the number density of cloud ice crystals and

it is prescribed as a function of temperature and  $m_i$  is the ice crystal mass, which is diagnosed from  $N_i$  and the total mass of cloud ice  $q_i$ .

Snow formation can occur through ice particles growing by deposition to become snow crystals. The conversion rate ( $S_{au}^d$ ) is calculated as follows:

$$S_{au}^d = \frac{S_{dep}^i}{1.5\{(m_s^0/m_i)^{(2/3)} - 1\}} \quad (2.7)$$

with  $m_s^0$  the initial mass of snow crystals which is set to  $m_s^0 = 3.0 \cdot 10^{-9}$  kg, corresponding to a particle diameter of approximately  $D_s^0 \simeq 300 \mu\text{m}$ . The ice crystal mass  $m_i$  is limited to a maximum value of  $m_i^{max}$  which is set to  $10^{-9}$  kg. For  $m_i = m_i^{max}$ , it can be shown that the autoconversion rate of cloud ice to snow corresponds to about 62% of the ice deposition rate.

The depositional growth rate of snow is given by the following expression:

$$S_{dep}^s = c_{dep}^s (1 + b_{dep}^s (\rho q^s)^{5/24}) (q^v - q_{si}^v) (\rho q^s)^{2/3} \quad (2.8)$$

where  $q^s$  is the mass fraction of snow,  $c_{dep}^s$  and  $b_{dep}^s$  are constant rate coefficients and  $\rho$  denotes air density.

**Cooling processes** The sublimation of snow ( $S_{dep}^s$ ) is calculated with Eq. 2.8 which results to a negative transfer rate when  $q^v < q_{si}^v$ .

Rain evaporation is calculated through:

$$S_{ev} = a_{ev} (1 + \beta_{ev} (\rho q^r)^{3/16}) (q_{sw}^v - q^v) (\rho q^r)^{1/2} \quad (2.9)$$

where  $a_{ev}$  and  $\beta_{ev}$  are constants.

The parameterization of snow melting is based on the assumption that the latent cooling due to melting as well as from condensation/evaporation is balanced by the heat flux between the particle and the air surrounding it. The transfer rate is as follows:

$$S_{melt}^s = c_{melt}^s (1 + b_{melt}^s (\rho q^s)^{2/3}) \{(T - T_0) + a_{melt}^s (q^v - q_{sw}^v(T_0))\} (\rho q^s)^{2/3} \quad (2.10)$$

where  $c_{melt}^s$ ,  $b_{melt}^s$  and  $a_{melt}^s$  are constants,  $q_{sw}^v$  is the saturation specific humidity with respect to water.

**Neglected processes** A few processes were found to have negligible contributions in the heating and cooling rates. These processes are the melting of cloud ice ( $S_{melt}^i$ ), the freezing of rain due to the collection of cloud ice to form snow ( $S_{cri}^r$ ), the freezing of rain due to heterogeneous nucleation to form snow ( $S_{frz}^r$ ), the heterogeneous nucleation of cloud ice ( $S_{nuc}$ ) and the freezing of cloud

water ( $S_{frz}^c$ ). These processes were at least two orders of magnitude smaller in magnitude compared to the dominant heating process at any time.

### 2.1.3 *Below-cloud and in-cloud process categories*

A novelty in our study is the decomposition of the different microphysical processes into in-cloud and below-cloud processes. A diabatic heating or cooling process is categorized as in-cloud when there is cloud water or cloud ice at the grid point, and as below-cloud when there is no cloud water nor cloud ice at the grid point. For simplification, some microphysical processes are grouped. For example the depositional growth of cloud ice, depositional growth of snow and the growth of cloud ice into the snow category are considered as one process. See Table 2.1b for an overview of the different process categories. Note that the term “cloud diabatic processes” is used for both in-cloud and below-cloud diabatic processes. All below-cloud processes are cooling processes, whereas most in-cloud processes are heating processes. Snow melting is an exception; it is a cooling process that can occur in as well as below clouds. Note that whereas most of the heating processes are well-constrained due to their dependence on resolved vertical ascent, the representation of the cooling processes is much more uncertain due to its dependence on the hydrometeor fall speed and hydrometeor size distributions (e.g. Forbes and Clark, 2003; Forbes and Hogan, 2006; Dearden et al., 2016). Moreover, these processes influence the vertical heating profile and thereby the strength of the diabatic PV modification. An overview of the main diabatic processes is given in Table 2.1a, and the different microphysical process categories are given in Table 2.1b.

### 2.1.4 *Other physical parameterizations*

Note that in the idealized case study (Chapter 3) turbulence, surface fluxes, convection and radiation are all switched off. The following description holds for the setup used in Chapters 4. Subgrid-scale turbulence is treated through a prognostic turbulent kinetic energy (TKE) closure including the effect of subgrid-scale condensation and thermal circulations. At the lower boundary Neumann boundary conditions are used for heat and moisture transport. The surface layer scheme uses TKE to calculate surface fluxes and includes a laminar-turbulent roughness layer. Convection is treated through a mass-flux convection scheme with a moisture convergence closure (Tiedtke, 1989). The heating rate due

Table 2.1: Diabatic processes

a: Description of the main diabatic process categories.

Category	Description
<i>CLOUD</i>	large-scale cloud scheme
<i>CON</i>	convection
<i>RAD</i>	shortwave and longwave radiation

b: Description of the subcategories for the total large-scale cloud scheme *CLOUD* split out to in-cloud and below-cloud processes and the corresponding source and sink terms from JW2012.

	Category	Description	JW2012
in-cloud	Deposition	Depositional growth of cloud ice and snow	$S_{aud} + S_{dep}^s + S_{dep}^i$
	Condensation	Condensation of cloud water	$S_c$
	Snow melt	Melting of snow	$S_{smelt}^s$
below-cloud	Evaporation	Evaporation of rain	$S_{ev}$
	Sublimation	Sublimation of snow	$S_{dep}^s$
	Snow melt	Melting of snow	$S_{smelt}^s$

to convection in the COSMO model can not be partitioned into the individual microphysical processes and is treated as one single quantity  $DHR_{con}$ . Shortwave (SW) and longwave (LW) radiation is calculated by a scheme after Ritter and Geleyn (1992). In this thesis SW and LW radiation is summed to give a total  $DHR_{rad}$ .

## 2.2 LAGRANTO trajectory model

For calculating the trajectories we make use of the LAGRANTO trajectory model (Sprenger and Wernli, 2015). LAGRANTO offers the possibility to calculate forward or backward trajectories and afterwards trace several variables along the trajectories where the variables are interpolated from the model grid points onto the trajectory positions. The time stepping for LAGRANTO for trajectory calculation is 1/12th of the time resolution of the input data (the COSMO model

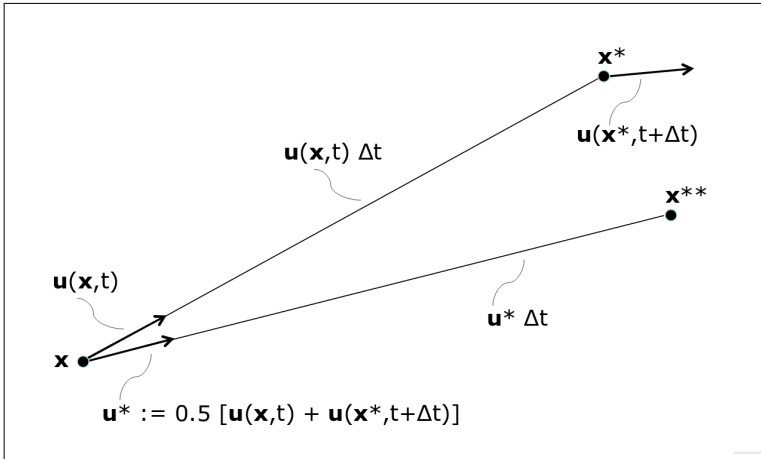


Figure 2.1: An illustration of the iterations used by the LAGRANTO model to calculate trajectory positions after Sprenger and Wernli (2015).

output). For finding the trajectory position at the next timestep three iterations are performed. This process is depicted schematically in Fig. 2.1. Consider an air parcel initially located at position  $\mathbf{x}$ . Its predicted location  $\mathbf{x}^*$  at  $(t + \Delta t)$  is calculated by adding to its initial position a displacement vector given by the winds at the starting position  $\mathbf{u}(\mathbf{x}, t)$  multiplied by  $\Delta t$ . In a next iteration, for the calculation of the wind vector  $\mathbf{u}^*$ , the average is taken between the wind at the starting position at time  $t$  and the wind at the predicted end position at time  $t + \Delta t$ .

For the spatial interpolation of the wind fields a linear interpolation is used in the vertical and a bilinear interpolation in the horizontal direction. For trajectories that cross the lower boundary of the domain, there is a special option to raise the trajectories by 10 hPa. In all our analyses this option is used. For the tracing of variables also a bilinear interpolation is used in the horizontal and a linear interpolation in the vertical. For using LAGRANTO on the idealized baroclinic channel in Chapter 3, small adaptations had to be made. First, the periodic boundary conditions had to be implemented, second, the spherical terms had to be set to zero since the grid is Cartesian with constant grid spacing in the horizontal directions.

### 2.3 Lagrangian PV budget

The modification of PV due to a specific diabatic process  $i$ , referred to as diabatic PV rate ( $DPVR_i$ ) can be calculated with the following equation (Ertel, 1942):

$$DPVR_i = \frac{1}{\rho} \cdot \boldsymbol{\eta} \cdot \nabla(DHR_i) \quad (2.11)$$

where  $DHR_i$  denotes the diabatic heating rate due to process  $i$ , as listed in Table 2.1;  $\boldsymbol{\eta}$  denotes the absolute vorticity vector and  $\rho$  is the air density. The heating rate gradients are calculated using the method of finite differences.

Whereas this instantaneous PV rate tells how an air parcel's PV is modified at a certain moment, to explain positive or negative PV anomalies in certain regions of a cyclone, one needs to take into account the history of the air parcels and their PV modification. The total effect of different diabatic processes on a parcel's PV can be calculated by integrating the diabatic PV rates (Eq. 2.11) along backward trajectories until a certain time  $t_0$ . This method of integrating diabatic PV rates along the flow was also used by Rodwell and Hoskins (1995). We will refer to the along-flow integrated diabatic PV rates as the diabatic PV (DPV), again separately for every process  $i$ :

$$DPV_i(\mathbf{x}(t)) = \int_{t_0}^t DPVR_i(\mathbf{x}(\tau)) d\tau \quad (2.12)$$

where  $\mathbf{x}(\tau)$  is the air parcel's trajectory.

The PV of an air parcel at time and position  $\mathbf{x}(t)$  can then be expressed as follows:

$$PV(\mathbf{x}(t)) = PV(\mathbf{x}(t_0)) + \sum_i DPV_i(\mathbf{x}(t)) + RES \quad (2.13)$$

i.e., the PV at time  $t$  is equal to PV at time  $t_0$  plus the sum of all diabatic PV contributions along the air parcel's trajectory, and RES is a residual. In addition we introduce the "total Lagrangian PV anomaly" of an air parcel at the position  $\mathbf{x}(t)$  as follows:

$$PV_{Lag}^*(\mathbf{x}(t)) = PV(\mathbf{x}(t)) - PV(\mathbf{x}(t_0)) \quad (2.14)$$

A comparison of the total Lagrangian PV anomaly with the total DPV (the second term on the r.h.s. in Eq. 2.13) gives us insight in the size of the residual and the accuracy of our Lagrangian budget approach. It was found that decreasing the model output frequency from once per hour, to every 12 minutes, significantly decreased the size of the residual (not shown). A further decrease in model output to 5 minutes did not further decrease the size of the residual.

Summarizing the above, when constructing a diabatic PV budget for a certain region, this implies that backward trajectories are started from every grid point in this region. The trajectories are calculated over a certain time period. Diabatic PV rates are traced along the trajectories and integrated over time. The resultant values represent the diabatic PV (DPV) budget. The focus in this thesis is on the diabatic PV related to the large-scale cloud scheme. We refer to this category as cloud diabatic PV (CDPV). This total CDPV can be decomposed in its microphysical contributions CDPV<sub>*i*</sub>, as listed in Table 2.1b.



# 3

## CLOUD DIABATIC PV ANOMALIES IN AN IDEALIZED EXTRATROPICAL CYCLONE

---

A modified version of this chapter has been published as Crezee, B., Joos, H. and Wernli, H. (2017). The microphysical building blocks of low-level potential vorticity anomalies in an idealized extratropical cyclone. *J. Atmos. Sci.* 74.5, 1402-1416.

### 3.1 Introduction

Early idealized cyclone modelling studies contributed a lot to the development of conceptual models for cyclones and their fronts (Hoskins and West, 1979; Simmons and Hoskins, 1979; Davies et al., 1991) and the different types of upper-level wave breaking (Thorncroft et al., 1993). Through the incorporation of moist processes based on a simple saturated adjustment scheme, Whitaker and Davis (1994) showed the role of mesoscale diabatically generated PV for the rapid amplification of the surface cyclones. Balasubramanian and Yau (1994) used an idealized model to study the influence of convection on a maritime cyclone. Also systems that rely on the presence of latent heat release for their existence have been studied in an idealized setup. Moore and Montgomery (2005) studied diabatic rossby waves and Davis (2010) simulated subtropical cyclones. Through selecting coherent bundles of trajectories in an idealized baroclinic channel model, detailed analyses of the impact of diabatic processes along the warm conveyor belt (Schemm et al., 2013) and cold conveyor belt (Schemm and Wernli, 2014) have been done. Recent idealized studies looked at polar low development (Terpstra et al., 2015), the influence of different microphysical processes on the tracks of cyclones (Coronel et al., 2015) and sting jets (e.g. Baker et al., 2014; Coronel et al., 2016).

Here, we build further on these advances, by applying the novel Lagrangian method as described in the previous Chapter to the idealized baroclinic channel setup as developed by Schemm et al. (2013). As will be shown, an idealized setup is well-suited for our purpose, since it allows us to study the microphysical processes in a fully isolated manner. We will quantify the importance of different microphysical processes for the diabatic formation of low-level PV anomalies in an extratropical cyclone. Specifically we want to investigate (i) the microphysical

processes contributing to the dynamically important low-level positive PV anomalies, (ii) the role played by in-cloud versus below-cloud processes for the low-level positive and negative PV anomalies, and (iii) the different scales at which the processes are important.

The structure of this chapter is as follows. The next section explains the idealized channel model. Section 3.3 briefly describes the cyclone development with a focus on the microphysics. The main results are presented in section 3.4 and this chapter concludes with a summary and discussion in section 3.5.

Horizontal grid spacing	0.1875° (~21 km)
Vertical grid spacing	200 m
Grid points (nx×ny×nz)	800×400×80
Domain dimensions (dx×dy×dz)	16800 km×8400 km×16 km
Model timestep	60 s
Model output	12 min
Physical parameterizations	Microphysics only

Table 3.1: Model setup for the idealized baroclinic channel.

## 3.2 Model setup

For the idealized modelling study the COSMO model (as described in section 2.1) is used in the idealized baroclinic channel model setup developed by Schemm et al. (2013). The basic state (shown in Fig. 3.1) consists of a baroclinic atmosphere in thermal wind balance, which is perturbed through the addition of a PV anomaly at the tropopause level. In contrast to Schemm et al. (2013), we extended the domain in the vertical up to a height of 16 km and slightly increased the baroclinicity by setting the parameters  $B_{y1}$  and  $B_{y2}$  (see equation 4 in Schemm et al., 2013) to 13 K and 11 K, respectively.

The model setup (see Table 3.1) is highly idealized: there are no surface fluxes of heat and moisture, there is no friction and the radiation, convection and turbulence schemes are switched off. The baroclinic channel measures 16800 km × 8400 km in the zonal and meridional directions, respectively. The Coriolis parameter is kept constant at its value at 45°N, i.e.,  $f = 1.03 \cdot 10^{-4} \text{ s}^{-1}$ . The initial state is strongly baroclinic with a jet stream peak velocity of about 60 m s<sup>-1</sup> (see Fig. 3.1). Adding an elliptically shaped PV anomaly with an amplitude of

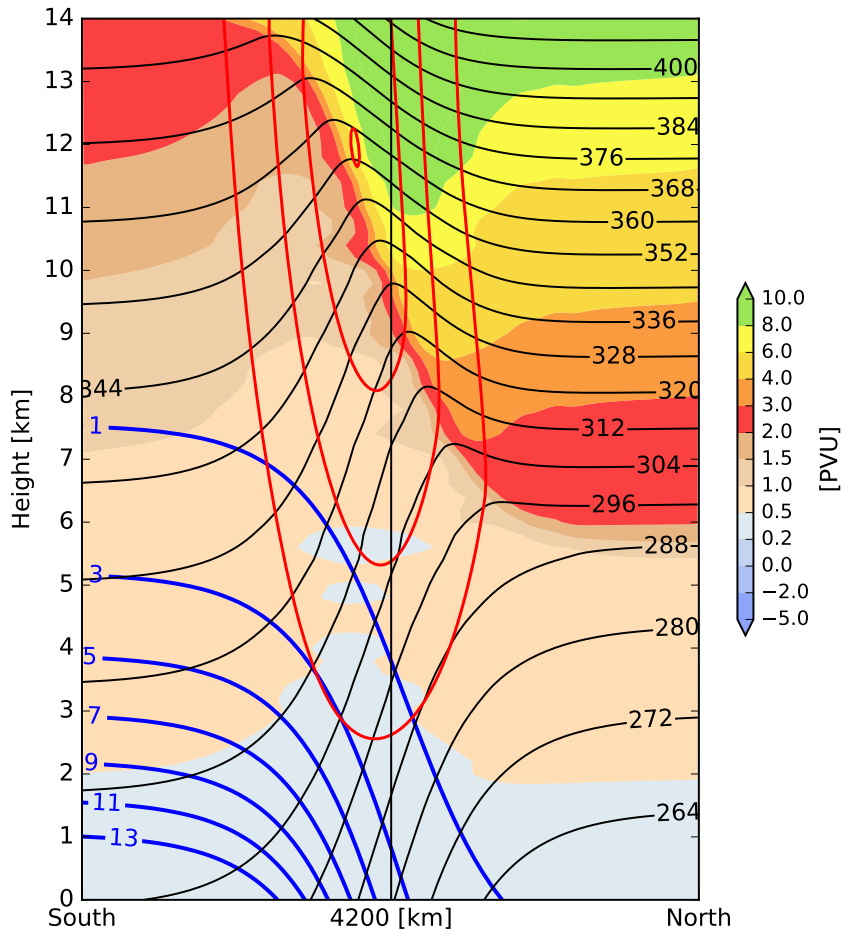


Figure 3.1: A meridional section across the baroclinic channel showing the perturbed basic state at the location where the upper-level PV anomaly was added. Shading shows values of potential vorticity (in PVU), black lines denote potential temperature (K), red lines windspeed (at intervals of  $15 \text{ m s}^{-1}$ ) and blue lines specific humidity ( $\text{g kg}^{-1}$ ).

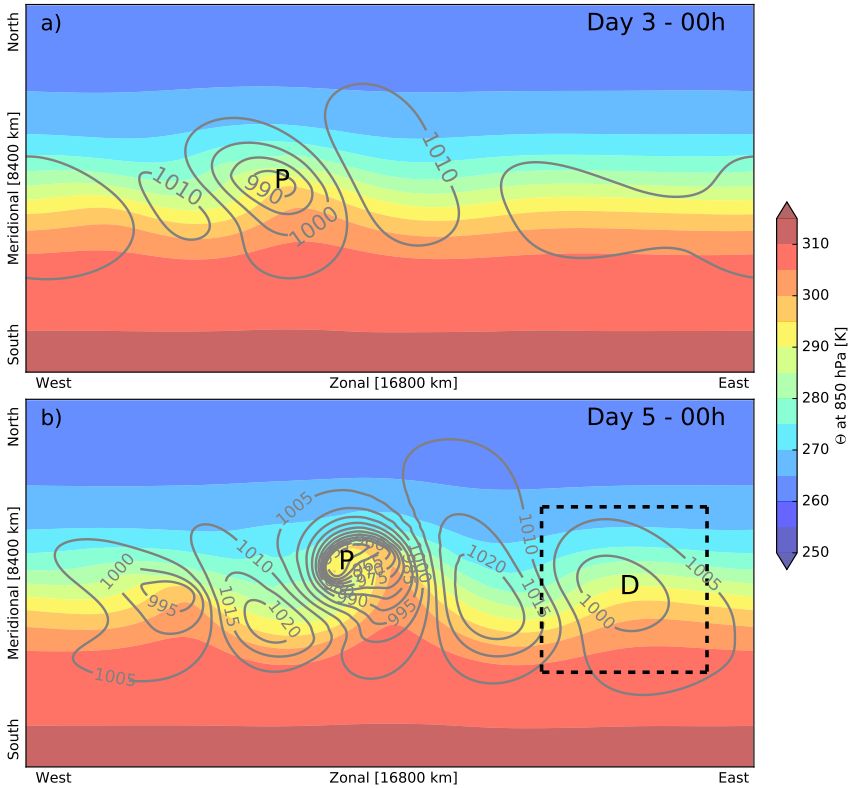


Figure 3.2: Overview of the simulation (a) at day 3, and (b) at day 5. Grey lines show surface pressure (hPa) and shading potential temperature at 850 hPa (K). The primary (P) and downstream (D) cyclones are labelled.

2 PVU at the tropopause level in the initial state triggers the formation of a cyclone, followed by upstream and downstream development. In our study we focus on the downstream cyclone as it more closely resembles the Shapiro-Keyser cyclone model (Shapiro and Keyser, 1990) compared to the primary cyclone. A cloud diabatic PV budget (see section 2.3) is constructed for a box around the downstream cyclone center measuring  $2940 \text{ km} \times 2940 \text{ km} \times 12 \text{ km}$  at time  $t=36 \text{ h}$ , integrating 36 h backwards in time.

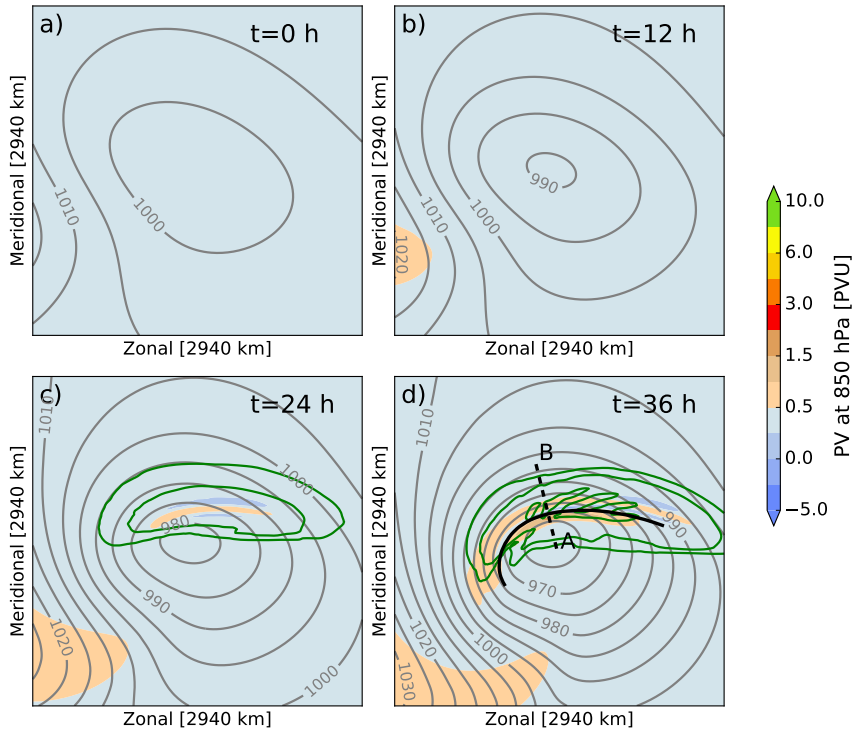


Figure 3.3: The temporal development of the downstream cyclone (centered at its core) at (a)  $t=0$  (day 5), (b)  $t=12$  h, (c)  $t=24$  h, and (d)  $t=36$  h. Shown are surface pressure (grey contours in hPa), total column condensate (green contours at 10, 100 and  $1000 \text{ g m}^{-2}$ ) and potential vorticity at 850 hPa (shading in PVU). In (d) the section (A-B) across the bent-back front is marked by a dashed line.

### 3.3 Cyclone development

A brief overview of the cyclone development and the accompanying clouds and precipitation is presented. The upper-level positive PV anomaly located at the center of the baroclinic zone leads to the development of the primary cyclone, which propagates eastward as can be seen in Fig. 3.2. After three days (Fig. 3.2a) the primary cyclone has a central sea level pressure below 990 hPa. The first signatures of both upstream and downstream development are visible to the west and east of the primary cyclone, respectively. After five days (Fig. 3.2b) the primary cyclone has developed to a mature system, whereas the downstream cyclone just starts to develop.

Figure 3.3 shows the development of the downstream cyclone over the next 36 hours in more detail. From now on we will refer to day 5 of the simulation as  $t=0$ , which corresponds to the cloud free incipient stage of the downstream cyclone. Within 36 hours the sea level pressure drops by more than 35 hPa, and clouds and precipitation develop (green contours in Fig. 3.3) and modify the PV field. For a detailed description of the development of the cyclone and its fronts the reader is referred to Schemm et al. (2013). Here, the focus will be on the development of clouds and precipitation (Fig. 3.4a) and the associated latent heating and cooling (Fig. 3.4b) in the downstream cyclone. At about  $t=13$  h the first ice clouds and snow form in the cyclone. It is from this moment that cloud diabatic processes modify the PV. Note that it takes about 9 hours before the first snow reaches the surface. Apparently, the early snow sublimates before reaching the surface, which is also indicated by the latent cooling shown in Fig. 3.4b. At about  $t=21-24$  h the first water clouds and rain appear. Between  $t=24-36$  h the cyclone develops a bent-back warm front and its structure (Fig. 3.3d) corresponds to the T-bone stage in the Shapiro-Keyser model, even though in our simulation there are no clouds at the cold front. Note that during this time period the in-cloud heating processes increase strongly, whereas the below-cloud cooling processes increase much less (Fig. 3.4b). Snow melt (occurring both in and below the cloud) is particular weak. At  $t=36$  h the total latent heating is about 4-5 times stronger compared to the total latent cooling. The dominant hydrometeor is snow and surface rainfall has strongly increased compared to 12 hours earlier (Fig. 3.4a). How the different cloud diabatic processes influence the PV, will be investigated in the next section.

## 3.4 Cloud diabatic PV budgets

### 3.4.1 *Total cloud diabatic PV across the warm front*

Figure 3.5a presents the total CDPV in a cross section perpendicular to the warm front extending from the cyclone center into the cold air (see Fig. 3.3d). Before analysing in detail this structure and how it is shaped by the different CDPV contributions in subsection 3.4.2, we first compare the total CDPV (Fig. 3.5a) to the total Lagrangian anomaly (Fig. 3.5b) defined in Eq. 2.14. The total CDPV agrees very well with the total Lagrangian anomaly. On the one hand, this can be expected, because all other PV non-conserving processes are switched off in this simulation. On the other hand, it is also a proof the reliability of the rather involved calculation of CDPV. In certain regions there are slight differences

due to either numerical PV non-conservation (Cooper et al., 1992) or errors, either in the trajectory positions, the calculation of the diabatic PV rates, or the interpolation of these rates to the trajectory positions.

Our approach of calculating Lagrangian anomalies through integrating cloud diabatic PV rates along backward trajectories, is different from the conventional way of defining a Eulerian PV anomaly, which usually corresponds to the deviation from a certain reference state. Therefore, here we also calculate the Eulerian anomaly ( $PV_{Eul}^*$ ) with as reference state the PV field at  $t_0=0$  h:

$$PV_{Eul}^*(t) = PV(t) - PV(t_0) \quad (3.1)$$

Comparing the CDPV anomaly (Fig. 3.5a) to the Eulerian anomaly (Fig. 3.5c), it becomes evident that the two anomalies are almost identical in the lower troposphere (0-3 km); there are small deviations in the mid-troposphere (3-6 km), whereas in the upper-troposphere (6-8 km) the differences are large. The small differences between the two fields in the mid-troposphere can most probably be explained by the effect of cross-isentropic PV transport whereas the large differences in the upper-troposphere are due to isentropic advection due to strong isentropic PV gradients close to the tropopause level. This effect will be explored in more detail in section A. We underline that for our main region of interest (0-6 km) the differences between the two fields are small. Also from now on, when we refer to a PV anomaly, we refer to an anomaly of CDPV (Fig. 3.5a).

### 3.4.2 Detailed structure across the warm front

The aim of this section is to understand the complex structure of the CDPV field in the warm-frontal cross section. It will be shown how the strength but also the structure of the anomalies is determined by the different in-cloud and below-cloud diabatic PV contributions. Note how we distinguish between the terms “anomaly” and “contribution”, anomalies refer to the total CDPV field, whereas contributions refer to CDPV contributions from the individual in-cloud and below-cloud processes (CDPV).

Every panel in Fig. 3.6 shows the total CDPV field in the background. As can be seen in Fig. 3.6a, the warm front is characterized by a strong low-level positive PV anomaly, which extends from the surface up to about 4 km and its maximum of about 1.5 PVU ( $1 \text{ PVU} = 10^{-6} \text{ m}^2 \text{ K kg}^{-1} \text{ s}^{-1}$ ) is approximately 1 km above the surface. Strongest winds at the surface of more than  $20 \text{ m s}^{-1}$  are found at and just north of the front, i.e., north of this positive PV anomaly. About 250 km north of the warm front, at the surface, there is another positive PV anomaly which

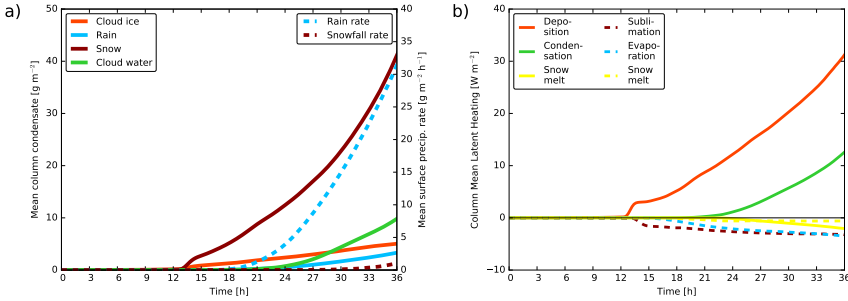


Figure 3.4: Time evolution of (a) column integrated condensate ( $\text{g m}^{-2}$ ) for the different hydrometeor species averaged over an area of  $2940 \text{ km} \times 2940 \text{ km}$  centered at the cyclone center (solid lines) and the mean surface precipitation rates in  $\text{g m}^{-2} \text{ h}^{-1}$  (dashed lines) averaged over the same area, (b) column integrated latent heating and cooling averaged over the same area. Solid lines correspond to in-cloud and dashed lines to below-cloud processes, respectively.

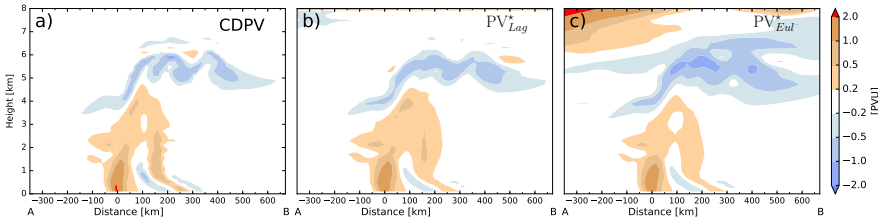


Figure 3.5: Vertical section across the warm front (A–B, see Fig. 3.3d) at  $t=36 \text{ h}$  of (a) the cloud diabatic PV (CDPV), (b) the Lagrangian PV anomaly ( $\text{PV}_{Lag}^*$ ), and (c) the Eulerian PV anomaly ( $\text{PV}_{Eul}^*$ ) at  $t=36 \text{ h}$ . Values are in PVU.



tilts southwards with height, it crosses the melting layer (grey line) and has its maximum of about 1.5 PVU just above the melting layer. Between 0-1 km height, this narrow positive anomaly is flanked by two rather small negative anomalies. At about 5-6 km altitude, a larger size negative PV anomaly can be identified.

Figure 3.6b shows the structure of clouds and precipitation in the same cross section. At the warm front, there is a deep cloud structure extending from the surface up to 7 km. The melting layer slopes from the surface up to 2 km and snow melting leads to strong rain at the surface near the surface front. About 100 km further south rainwater contents are much lower and decreasing from the melting layer towards the surface. In this region the air is sub-saturated (not shown) and rain evaporates before reaching the surface. Towards the cold side of the front, the 0 °C isotherm is close to the surface and snow reaches the surface. Most intense snowfall occurs about 200 km north of the warm front, whereas further north, snow does not reach the surface due to sublimation.

Figures 3.6c and 3.6d show the diabatic PV contributions (CDPV<sub>i</sub>) of selected in-cloud and below-cloud processes, respectively. Note again that these are not instantaneous values, but rather integrated along backward trajectories. For the in-cloud processes (3.6c), the largest positive contributions are from condensation (green contours) and ice and snow deposition (orange contours) both contributing locally about 0.5 PVU. The former is strongest near  $z = 1$  km whereas the latter has maxima near 4 km. In between there are small positive contributions from snow melting (yellow contours). Comparing this to the total CDPV shown in shading reveals that in certain regions positive and negative contributions from two different processes cancel. Strong negative contributions are found between 3 and 6 km height in a region approximately following the cloud tops (see Fig. 3.6b). These regions are characterized by low PV since they lost up to 0.5 PVU due to ice and snow deposition. Contributions of the below-cloud processes (Fig. 3.6d) are generally weaker than those from in-cloud processes. Whereas the in-cloud processes have the strongest negative contributions above 3 km, below-cloud processes contribute strongly to negative anomalies near the surface. The negative anomaly just below the melting layer seems to be related to snow melting (Fig. 3.6d, between 100-200 km). Further north, sublimation of snow or ice leads to a negative anomaly. The below-cloud processes don't only lead to negative anomalies, they also contribute to the positive low-level PV anomalies. Rain evaporation contributes positively to both low-level strong positive PV anomalies, whereas snow melting only contributes positively to the northern positive PV anomaly (Fig. 3.6d). When comparing the

below-cloud PV anomalies with the cloud pattern in Fig. 3.6b, it becomes evident that below-cloud processes are important also for the PV of air parcels that are at this moment located within the cloud. Also, there are regions outside the cloud, where PV has been modified before due to in-cloud processes. This is an important result, which indicates that (i) at a certain time the PV field cannot be understood from instantaneous diabatic tendencies, and (ii) the Lagrangian, i.e., time-integrated perspective is essential for understanding the PV structure in an extratropical cyclone.

With Fig. 3.6 we only investigated one specific section across the three dimensional anomalies. To be more systematic, we now identify the different anomalies as connected three dimensional regions, where the absolute value of the total CDPV is larger than a threshold value of 0.2 PVU and analyse the individual CDPV

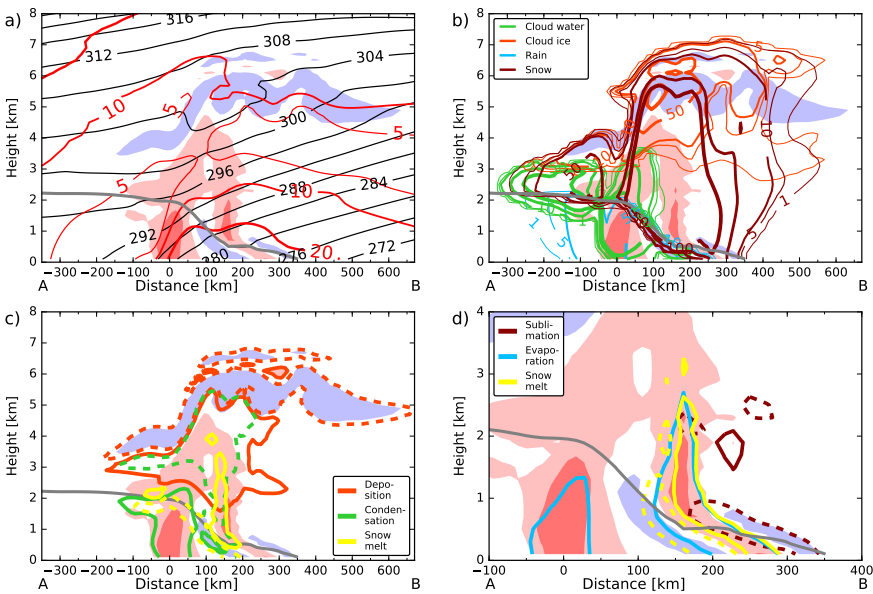


Figure 3.6: The same vertical section (A–B) across the warm front as shown in Fig. 3.5 at  $t=36$  h. In each panel the  $0^{\circ}\text{C}$  isotherm is shown as a grey line and regions where CDPV exceeds a certain threshold are shaded. Regions with  $\text{CDPV} < -0.2$  PVU are light blue, regions with  $0.2 < \text{CDPV} < 0.75$  PVU are light red and regions with  $\text{CDPV} > 0.75$  PVU are red. Panel (a) shows isentropes (black lines; in K) and wind speed (red contours; in  $\text{m s}^{-1}$ ). In (b) hydrometeor densities [ $\text{g kg}^{-1}$ ] are shown for cloud water (green), cloud ice (orange), rain (blue) and snow (red). Panels (c) and (d) show different in-cloud and below-cloud diabatic PV contributions, respectively (solid and dashed contours denote values of  $+0.2$  PVU and  $-0.2$  PVU, respectively).

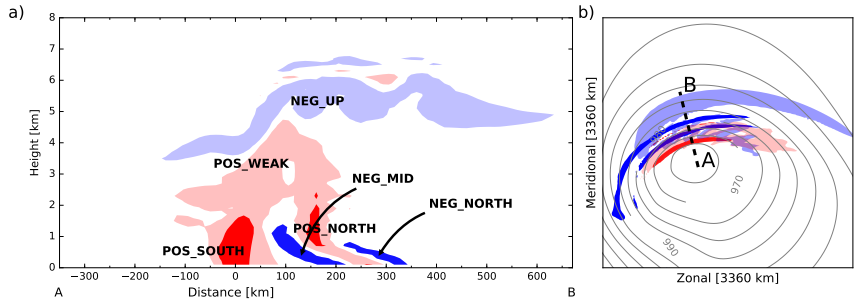


Figure 3.7: Selected positive (red) and negative (blue) CDPV anomalies at  $t=36$  h in (a) the same vertical section (A–B) across the warm front as shown in Fig. 3.5 and (b) as seen from above. For the dark red anomalies a threshold of 0.75 PVU was chosen, all other anomalies have a threshold of 0.2 PVU. Panel (b) shows the horizontal extent of the anomalies at  $z=600$  m for POS\_SOUTH, POS\_NORTH (dark red); NEG\_MID, NEG\_NORTH (dark blue), at  $z=3000$  m for POS\_WEAK (light red), and at  $z=5000$  m for NEG\_UP (light blue).

contributions for each anomaly. Small anomalies covering less than 100 grid points are neglected.

One large positive anomaly is centered along the (bent-back) warm front. This anomaly stretches from the surface up to about 5 km, is approximately 400 km wide and 2000 km long. Within this positive anomaly, there are two regions with particularly high CDPV values. Therefore an additional threshold of 0.75 PVU was applied to separately analyze these stronger parts of the positive PV anomaly. As can be seen in Fig. 3.7a, the positive anomaly is split into three distinct anomalies: a relatively large but weak anomaly, POS\_WEAK, a smaller but stronger anomaly located approximately at the warm front, POS\_SOUTH, and another strong anomaly located approximately 150 km further north, POS\_NORTH. In addition to these three positive anomalies, we identify three negative anomalies (see Fig. 3.7a): A large anomaly in the upper-troposphere, NEG\_UP, a small anomaly, NEG\_MID, in between the two strong positive anomalies at low levels, and, another low-level negative anomaly, NEG\_NORTH, located north of POS\_NORTH. Figure 3.7b indicates that many of these anomalies are zonally extended along the (bent-back) warm front. Their extent ranges from about 1500 km for POS\_SOUTH and POS\_NORTH to about 3000 km for NEG\_UP.

### 3.4.3 *Microphysical processes contributing to the individual anomalies*

In Fig. 3.8, the contributions from the different cloud diabatic processes to the CDPV are shown separately for each of the previously defined PV anomalies. Most of the negative anomalies exist mainly due to a single process, which is different for each anomaly. The NEG\_UP anomaly (Fig. 3.8a) exists due to PV destruction caused by depositional growth of ice and snow with a strength of about  $-0.5$  PVU. The other processes do not contribute significantly to the formation of NEG\_UP. PV destruction due to snow melting in and below clouds fully explains the existence of NEG\_MID (Fig. 3.8b). For this anomaly, the negative contributions are partially offset by positive contributions from condensation and rain evaporation, effectively reducing the strength of this anomaly. NEG\_NORTH (Fig. 3.8c) is a rather weak anomaly of about  $-0.3$  PVU, which is the result of below-cloud snow sublimation.

For the positive PV anomalies, the picture is more complex. The anomaly POS\_WEAK (Fig. 3.8d) has a net positive contribution of about  $0.25$  PVU from depositional growth of ice and snow. The net contributions from the other in- and below-cloud processes are close to zero, due to both positive and negative contributions within the anomaly. POS\_SOUTH (Fig. 3.8e) has strong contributions of  $0.8$  PVU from in-cloud condensation, but also small contributions of  $0.2$  PVU from below-cloud rain evaporation. Both processes influence the whole area of the PV anomaly. For the existence of POS\_NORTH (Fig. 3.8f), below-cloud processes are crucial. This anomaly owes its strength to snow melting and rain evaporation, both contributing about  $0.4$  PVU. Whereas the negative anomalies are mainly formed by a single cloud diabatic process, the positive anomaly as a whole (POS\_WEAK, POS\_NORTH and POS\_SOUTH) exists due to contributions from many different processes. Depositional growth of ice and snow acts over a large region, however the associated PV modification is small in magnitude. The PV modification due to condensation, below-cloud rain evaporation, and snow melting are much stronger, but act at much smaller scales. Below-cloud processes contribute with about 20% to POS\_SOUTH. For POS\_NORTH most contributions are from below-cloud processes. Note that this anomaly, existing due to below-cloud processes, is located partially within the cloud (see Fig. 3.6). This analysis shows that the complex pattern of PV anomalies can only be understood by (i) taking into account the contributions from all cloud diabatic processes to the PV modification and (ii) by applying a Lagrangian perspective where the PV modifications can be traced along the pathway of the air parcels that end up in

the anomalies.

In the next section we will explore in more detail how the two strong positive anomalies and the northern negative anomaly have developed over time.

### 3.4.4 Temporal evolution of diabatic PV rates of selected anomalies

The Lagrangian perspective allows not only to investigate due to which processes a certain anomaly has developed, but also allows to quantify the timescales of the

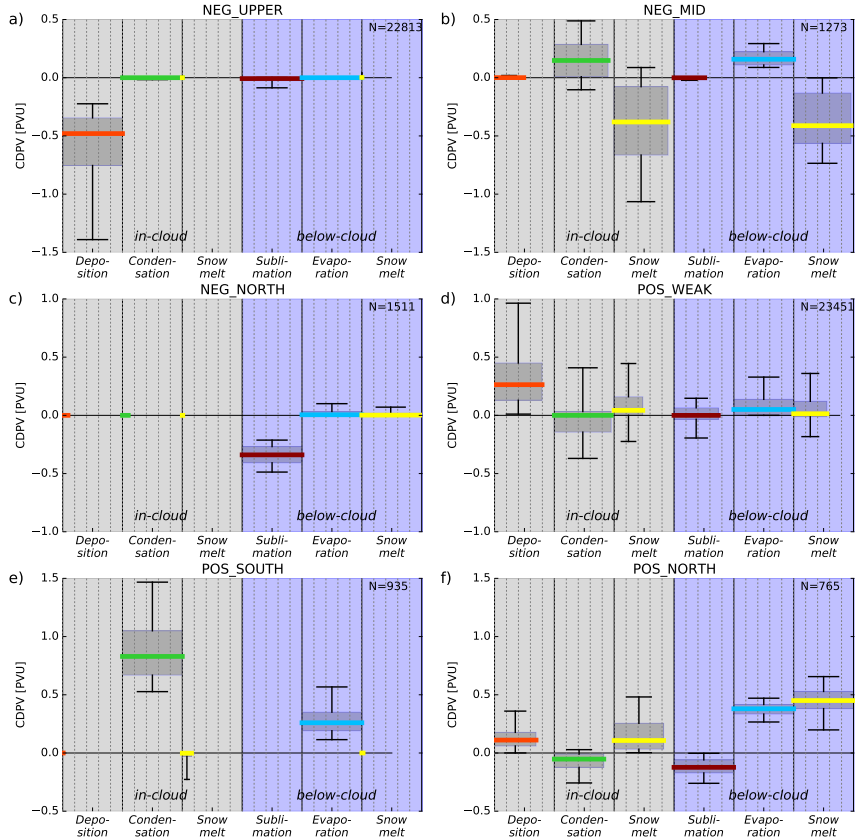


Figure 3.8: Boxplots showing on the left the in-cloud (iCDPV) and on the right the below-cloud diabatic PV (bCDPV) contributions at  $t=36$  h to the anomalies (a) NEG\_UPPER, (b) NEG\_MID, (c) NEG\_NORTH, (d) POS\_WEAK, (e) POS\_SOUTH (f) POS\_NORTH. For each process the grid points with non-zero contributions for this process are selected to calculate the percentiles. The box extends from the 25th to the 75th percentile with the horizontal line indicating the median and the whiskers extending to the 5th and 95th percentiles. The width indicates the fraction of the total anomaly where this process has contributed to the PV anomaly.

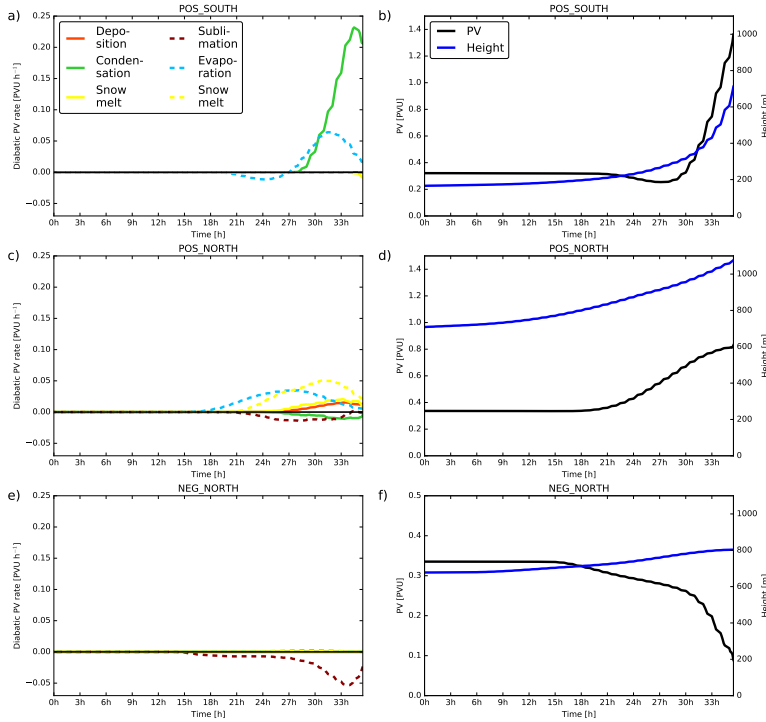


Figure 3.9: Time evolution of the median value of several variables and along the trajectories that end at  $t=36$  h in PV anomalies (a,b) POS\_SOUTH, (c,d) POS\_NORTH and (e,f) NEG\_NORTH at time  $t=36$  h. The left panels show median cloud diabatic PV rates for in-cloud (solid lines) and below-cloud (dashed lines) processes [in  $\text{PVU h}^{-1}$ ]. The right panels show median PV (black in PVU) and height (blue in m).

buildup of the anomalies. As can be seen in Figs. 3.9a,b the anomaly POS\_SOUTH is produced during the last approximately 6 hours due to below-cloud rain evaporation and in-cloud condensation. During this time, the median PV value of the air parcels rises from about 0.3 to about 1.3 PVU whereas they ascend from about 200 to 700 m with half of the total height gained in the last 4 hours. In contrast to POS\_SOUTH, the northern strong positive anomaly POS\_NORTH (see Figs. 3.9c,d), is built up over a longer time period of approximately 18 hours. Air parcels forming this anomaly ascend only about 350 m in 36 hours. They gain their PV mainly due to below-cloud rain evaporation and snow melting. These processes occur when hydrometeors fall through the air parcels as they travel westwards just to the north of the bent-back front (not shown). The negative anomaly NEG\_NORTH (Figs. 3.9e,f) forms due to snow sublimation in a very slowly

rising airstream during a time of approximately 6 hours. This analysis reveals that the formation of the different anomalies is characterized by different time scales and trajectory pathways.

### 3.5 Summary and discussion

A novel Lagrangian method was developed to provide insight into the microphysical building blocks of low and mid-level diabatically produced PV anomalies in an idealized extratropical cyclone. The positive anomaly as a whole, extends about 1500 km along the (bent-back) warm front. The cross-frontal structure is complex. Three different positive PV anomalies with different amplitudes can be identified. A rather large but weak positive anomaly is formed due to depositional growth of cloud ice and snow. A smaller but strong positive anomaly at lower levels is formed mainly due to condensation heating. About 200 km to the north, there exists another small but strong positive anomaly, which owes its existence mainly to below-cloud rain evaporation and snow melting. Whereas the positive anomalies are produced by a complex combination of different processes, the generation of the negative anomalies is characterized by a single microphysical process for each anomaly. The large upper-tropospheric negative anomaly is formed due to PV destruction caused by the depositional growth of cloud ice and snow. For the low-level negative anomaly north of the surface warm front, snow melting is the dominant process, and for the low-level negative anomaly further north, PV is decreased mainly due to the cooling induced by snow sublimation. Furthermore, the microphysical processes contributing to both the positive and negative anomalies, act on different scales. Depositional growth of cloud ice and snow is relevant over a large region (about 300 km in the cross-frontal direction), however rather small in magnitude (typically 0.2-0.4 PVU). On the other hand, cloud condensation and below-cloud process are rather strong in magnitude (typically 0.3-1.0 PVU), but act at smaller scales (about 50 km in the cross-frontal direction). It was found that whereas below-cloud processes contribute only slightly to the strong southern positive PV anomaly, the northern positive PV anomaly consists almost fully of below-cloud contributions from snow melting and rain evaporation, highlighting the importance of below-cloud processes for the positive PV anomaly as a whole. The existence of PV anomalies located in the cloud, however created by below-cloud processes can only be understood by considering the history of the air parcels in these anomalies. Air parcels experience PV modification due to below-cloud processes as long as they are located below the cloud. Later, when ascending into the cloud, they

carry the signal of below-cloud PV modification into the region where also in-cloud processes can further modify their PV. It was shown that the strong low-level southern positive PV anomaly builds up in a relatively short time of 4 hours whereas the northern anomaly is created within about 18 hours.

In summary, the key findings of this study are:

- The below-cloud processes rain evaporation and snow melting contribute significantly to the formation of the low-level positive PV anomaly.
- A complex combination of microphysical processes dictates the shape and strength of the low-level positive PV anomaly.
- The snow melting and sublimation processes each produce a low-level negative anomaly.
- The cross-frontal scale at which different processes act range from ~50 km for the below-cloud processes to ~300 km for ice and snow deposition.
- A Lagrangian perspective is needed for understanding the formation of the complex low-level PV structures in extratropical cyclones.

In the final paragraphs, we put our results into the context of the existing literature. Parker and Thorpe (1995) found that the cooling induced by snow sublimation was mainly of local influence. This is consistent with our finding, that only a small negative anomaly is related to snow sublimation. Clough and Franks (1991) argued that snow sublimation is more relevant in influencing the mesoscale dynamics than rain evaporation. Our findings slightly contradict this statement, since we find a rather weak positive anomaly due to snow sublimation and rather strong contributions from rain evaporation, mainly to the northern positive PV anomaly. The relevance of snow melting, mentioned already by Szeto et al. (1988a), is confirmed in our study as snow melting is highly relevant for the formation of both a negative and a positive low-level PV anomaly. On the other hand, Dearden et al. (2016) found no significant influence of snow melting and sublimation on the mesoscale dynamics at the fronts of two summertime cyclones. Huang and Emanuel (1991) showed how cooling due to rain evaporation strengthens the frontal circulation to the north of the warm front and leads to a faster collapse of the surface gradients. This finding is consistent with the significant contributions of rain evaporation to the northern positive PV anomaly. Importantly, whereas several earlier studies (e.g., Huang and Emanuel, 1991; Marecal and Lemaitre, 1995; Parker and Thorpe, 1995), showed the relevance for snow melting and rain evaporation in downdraft regions, we find that these



cooling processes can actually increase the PV of rising parcels, when the cooling processes are located below these parcels. Our finding about the different scales of influence of depositional growth of ice and snow (important for the large size positive PV anomaly) compared to snow sublimation (important for the small size negative PV anomaly), is consistent with Forbes and Clark (2003). They stated that the former affects the large-scale synoptic evolution whereas the impact of the latter is restricted to the frontal scales. Coronel et al. (2015) showed that an idealized extratropical cyclone simulated with full microphysics (including ice deposition and below-cloud cooling processes) crosses the jet earlier when compared to a simulation with only condensational heating.

Although our method presents a detailed view on the different microphysical contributions, we cannot make any statement about the relevance of cloud diabatic processes compared to other non-conserving processes like radiation (Chagnon et al., 2013), friction (Boutle et al., 2015) or turbulence. Our method could be extended to include these effects, however, it is believed that the complexity of the microphysical contributions themselves is best presented in an isolated manner, i.e., without other non-conservative processes impacting their structure. In addition, other studies have assessed the impact of cloud diabatic processes as a whole in comparison to other PV non-conservative processes (e.g., Chagnon et al., 2013; Chagnon and Gray, 2015). The diagnostic decomposition of the low-level PV anomalies into their microphysical building blocks is novel. A more common approach to assess the relevance of a certain process, is to perform different sensitivity studies with and without latent heating or cooling due to the considered process. In contrast, our combined Lagrangian and PV-based approach gave us a way to assess the relevance of the different processes in a single simulation. The results might guide flight planning during field experiments in order to obtain observations in regions that are sensitive to a certain microphysical process. Also testing the dynamical impact of different microphysical schemes can be a useful application of our novel method. The question to what extent the structure and composition of the low-level PV anomalies in this idealized cyclone are representative for a real case cyclone will be answered in the next chapter.



# 4

## CLOUD DIABATIC PV ANOMALIES IN A STRONG MARITIME EXTRATROPICAL CYCLONE

---

In Chapter 3 an idealized model setup was used to study the formation of low and mid-level cloud diabatic PV anomalies. In this chapter it will be investigated to what extent the main findings hold for a real case extratropical cyclone.

### 4.1 Introduction

The studied cyclone is a particularly strong maritime winter cyclone, occurring from 12-14 December 2015, over the Bering Sea to the west of Alaska. With a minimal pressure of 924 hPa at 06 UTC 13 December this is one of the strongest cyclones in the Bering Sea region on record bringing hurricane force sustained winds and gusts up to  $185 \text{ km h}^{-1}$  to the Aleutian Islands<sup>1</sup>. The cyclone originates from a weak subtropical low located over southern Japan on 10 December after which it crosses the Pacific ocean as a very diabatic system.

The cyclone simultaneously crosses the dateline and the jet from the warm to the cold side and intensifies very rapidly (50 hPa in 24 hours). The crossing of the jet from the warm to the cold side and rapid intensification are also often observed in strong North Atlantic cyclones impacting Europe (e.g. Baehr et al., 1999; Wernli et al., 2002; Rivière and Joly, 2006; Pinto et al., 2009). Figure 4.1 shows the cyclone at 00 UTC 13 December 2015 as represented in the ECMWF analysis data. As can be seen in Fig. 4.1a, the cyclone - having its center at the dateline - has occluded and has a strong cold front stretching far to the south. The PV field at 850 hPa (Fig.4.1b) shows a wide band with values over 2 PVU stretching from the triple point (where the warm front, cold front and bent-back front meet) along the bent-back front towards the cyclone center. Along the cold front PV values are generally lower (around 1 PVU) but still higher compared to the ambient air. The 320 K isentropic PV (Fig.4.1c) shows a cyclonic or LC2 wave-breaking (Thorncroft et al., 1993) with the trough wrapping cyclonically around the cyclone center. Downstream of the trough a strong ridge builds, characterized by rather low PV values ( $<0.5 \text{ PVU}$ ) at 320 K. High PV ( $>3 \text{ PVU}$ ) air overlies the cyclone center. The structure of the cyclone and its occurrence over

---

<sup>1</sup> *The Washington Post*: <http://www.washingtonpost.com/news/capital-weather-gang/wp/2015/12/14/bering-sea-bomb-cyclone-ties-record-for-strongest-storm-in-north-pacific/>, Accessed: 2016-09-30

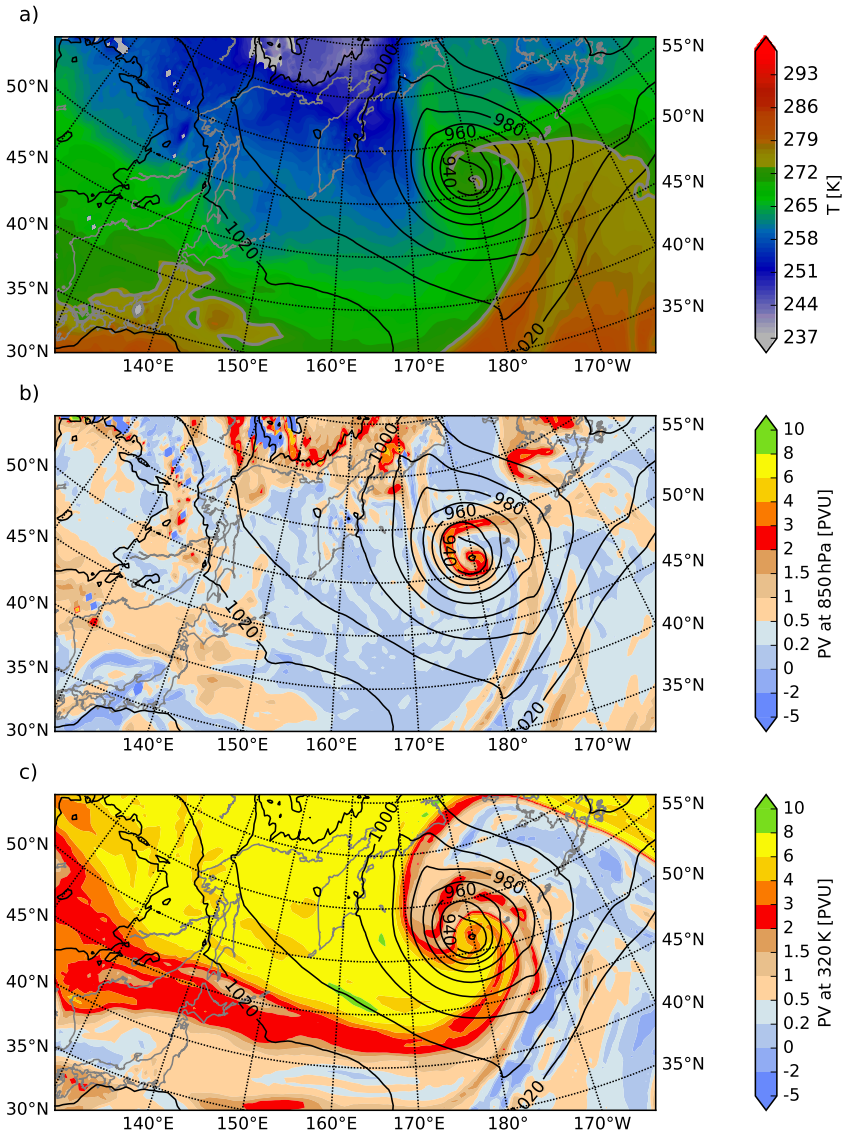


Figure 4.1: The cyclone at 00 UTC 13 December 2015 as represented in the ECMWF analysis data. Labelled sea level pressure contours (hPa) are shown in black with colours showing (a) temperature at 850 hPa (in K), (b) PV at 850 hPa (in PVU) and (c) PV at 320 K (in PVU).

sea make this a perfect candidate for applying the cloud diabatic PV diagnostics. Moreover, this allows us to find out whether or not the main findings from the idealized case in Chapter 3 are similar for the real case cyclone. The following items will be investigated:

- The impact of microphysics on the mesoscale PV structure along the warm front
- The importance of below-cloud processes for the positive and negative PV anomalies

And in addition, an answer will be provided to the following questions:

- Can the mesoscale PV structure along the cold front be understood from the microphysics?
- How do the microphysical contributions - focusing on below-cloud processes - to the PV anomalies change over time?
- How do size and strength of the PV anomalies change over time?
- How different is the Lagrangian perspective from the Eulerian perspective for the microphysical PV modification?

The outline of this chapter is as follows: the COSMO model setup is described in section 4.2, in section 4.3 the cyclone development is studied with a comparison to ECMWF analysis data. The results on the cloud diabatic PV budget are split into two parts. In the first part (section 4.4) the frontal wave stage of the cyclone is analyzed. The second part (section 4.5) analyzes the time evolution of the CDPV budget from the frontal wave stage until its occluded stage 24 hours later. In section 4.6 the results are compared to the idealized case and the chapter concludes with a summary.

## 4.2 Model setup

The storm is simulated with the COSMO model as described in section 2.1. As initial and lateral boundary conditions analysis data from the ECMWF are used. The model is set up on a rotated grid with horizontal grid spacing of  $0.125^\circ$ , corresponding to roughly 14 km. In the vertical a pressure based hybrid coordinate system is used. See Table 4.1 for an overview of the model setup and section 2.1.4 for a description of the physical parameterizations.

Horizontal grid spacing	0.125° (~14 km)
Vertical grid spacing	~10 m (surface) to ~790 m (10 km height)
Grid points (nx×ny×nz)	450×260×40
Domain dimensions (dx×dy×dz)	6300 km×3640 km×22 km
Model timestep	40 s
Model output interval	15 min
Physical parameterizations	Microphysics, turbulence, surface layer, convection, radiation

Table 4.1: Model setup for the real case study.

## 4.3 Cyclone development

### 4.3.1 *Synoptic evolution*

The COSMO simulation captures the development of this system well, both in terms of its position (Fig. 4.2a) and its core pressure (Fig. 4.2b) when compared to the ECMWF analysis data. Only during the deepest stage, the core pressure in COSMO is about 5 hPa lower compared to the ECMWF analysis. At 06 UTC 13 December, the pressure in COSMO of 923 hPa matches very well with the 924 hPa pressure as indicated in the NOAA surface analysis (see Fig. 4.3). The mismatch of central pressure in the ECMWF analysis at this time (929 hPa) could be related to the relatively coarse resolution of 0.5° compared to 0.125° for the COSMO simulation.

After model initialization time at 12 UTC 11 December (A), the cyclone is located just to the east of Japan and has a core pressure of about 980 hPa. During the next 12 hours (A-B) the cyclone gradually intensifies while tracking east-northeast towards the middle of the North Pacific (Fig. 4.6a). At 00 UTC 12 December (B), the cyclone is located downstream of a deepening upper-level trough (Fig. 4.5b), in a strong baroclinic zone (Fig. 4.6a). High values of vertically integrated column vapor to the south of the cyclone lead to strong precipitation (Fig. 4.6b), the cyclone leaves a broad region with >30 mm 12h-accumulated precipitation in its wake. The rather high PV values at 850 hPa located north of the cyclone center along the front (Fig. 4.5a), are most likely diabatically produced.

The strongest intensification takes place during the consecutive 24 hours (from

B to roughly C2) when the pressure drops about 50 hPa. This corresponds to a Bergeron value of 2.4 and thus a very explosive cyclogenesis (Sanders and Gyakum, 1980). The upper-level wave amplifies (Fig. 4.5d) and the broad trough overruns the low-level baroclinic zone (Fig. 4.6c), thereby advecting warm and moist air (Fig. 4.6d) northwards along the eastern flank of the surface low that is now characterized by a broad warm sector. Strongest precipitation (about 30 mm over the past 12 hours) occurs along the warm front, with weaker precipitation (about 10 mm over the past 12 hours) along the cold front. At low-levels high PV ( $>6$  PVU) can be found along the warm front and cold front (Fig. 4.5c), and the cyclone has a frontal wave structure at this stage (C1). During the next 12 hours (C1-C2) the cyclone occludes as can be seen by the

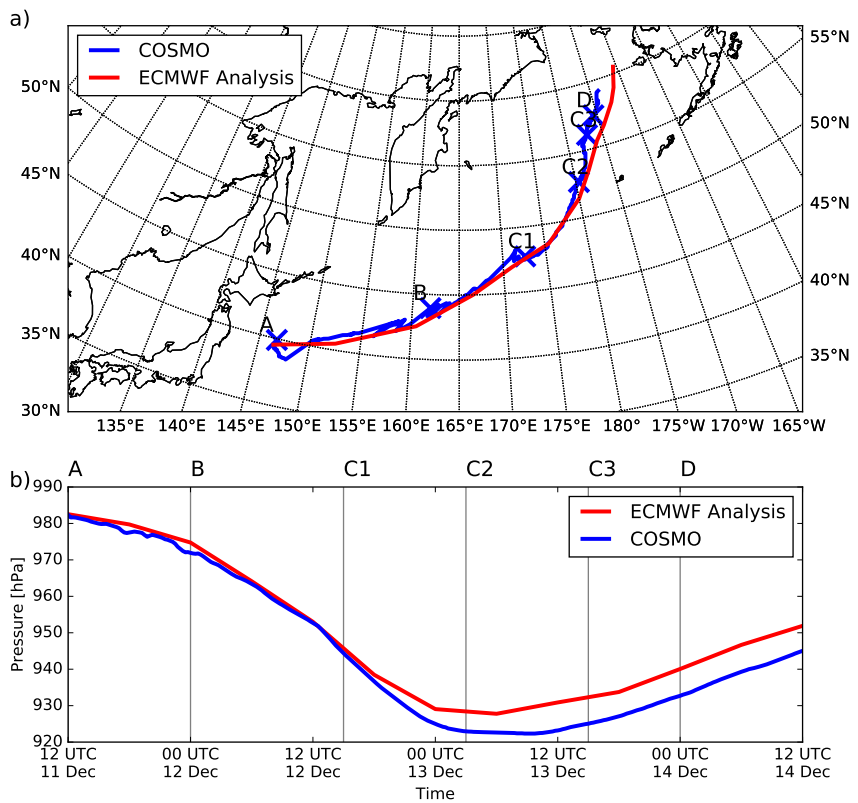


Figure 4.2: (a) Cyclone track as in COSMO (blue) and EC Analysis (red) from 12 UTC 11 December 2015 to 12 UTC 14 December 2015, (b) minimal sea level pressure in hPa over the same time period. The different stages referred to in the text are labelled as A, B, C1, C2, C3 and D.

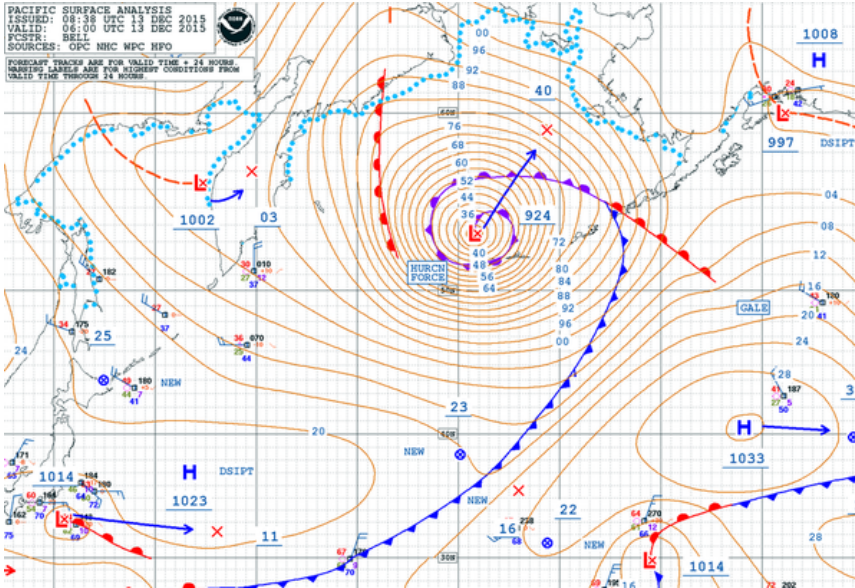


Figure 4.3: Pacific surface analysis by NOAA (and the related NCEP centers as mentioned at the top left) valid for 06 UTC 13 December 2015. Available online: <http://nomads.ncep.noaa.gov/ncep/NCEP/>, accessed on: 2016-09-30.

warm sector almost disappearing (Fig. 4.6c,e). The occluded front, indicated by relatively high vertically integrated water vapour in Fig. 4.6f, wraps around the cyclone center. Cold air (Fig. 4.6c) is advected southwards to the west of the cyclone and rapidly pushes the cold front southeastwards. The bands of high PV ( $>4$  PVU) at 850 hPa apparent at C1 have weakened considerably, although now a broader region is characterized by relatively high PV ( $>1$  PVU). The upper-level trough has wrapped cyclonically around the cyclone center (LC2 wave breaking) and high PV air is overlying the low-level diabatically produced PV, thereby forming a so-called PV tower. A few hours later at 09 UTC 13 December (between C2-C3) the cyclone reaches its lowest pressure of about 922 hPa while hitting parts of the Aleutian Islands and entering the Bering Sea. In the next 12 hours (C2-C3), the movement of the cyclone slows down while its core pressure gradually starts to rise. The upper-level and low-level circulations are strongly coupled and the cyclone further occludes.

From C1-C3 the system changes from a strongly baroclinic to a more barotropic system. We will refer to this as the transition phase.



### 4.3.2 Microphysical evolution

As seen in the previous section the studied cyclone moves from the warm (anticyclonic) to the cold (cyclonic) side of the jet and rapidly intensifies during this transition. During this transition phase (C1-C3), the temperature regime surrounding the cyclone center changes rapidly. Therefore in this section we have a closer look at how this change in temperature regime influences the microphysics.

Hydrometeor budgets are considered in a cyclone-following box of  $1400 \text{ km} \times 1400 \text{ km}$ , and in this box for each hydrometeor the total mass is calculated and divided by the surface area of the box. The budgets are presented in Fig. 4.4a. Snow is the most abundant hydrometeor over the full lifecycle of the cyclone. At C1, mean column integrated snow is about  $750 \text{ g m}^{-2}$ , dropping to 600 and  $250 \text{ g m}^{-2}$  at C2 and C3, respectively. Cloud water decreases from  $200 \text{ g m}^{-2}$  at C1 to only  $20 \text{ g m}^{-2}$ , before dropping to zero at C3. Cloud ice remains remarkably constant over the full life-cycle with values at around  $50 \text{ g m}^{-2}$ . At C1, the strongest large-scale precipitation comes from rain, with a mean rate of about  $650 \text{ g m}^{-2} \text{ h}^{-1}$ . Snow rates are about  $400 \text{ g m}^{-2} \text{ h}^{-1}$  at this time. At C2, snow rates have slightly increased, whereas rain rates have dropped significantly to  $200 \text{ g m}^{-2} \text{ h}^{-1}$ . At C3 rain rates have further dropped to only  $50 \text{ g m}^{-2} \text{ h}^{-1}$ , whereas snow rates slightly dropped to  $250 \text{ g m}^{-2} \text{ h}^{-1}$ . In the mean time, convective

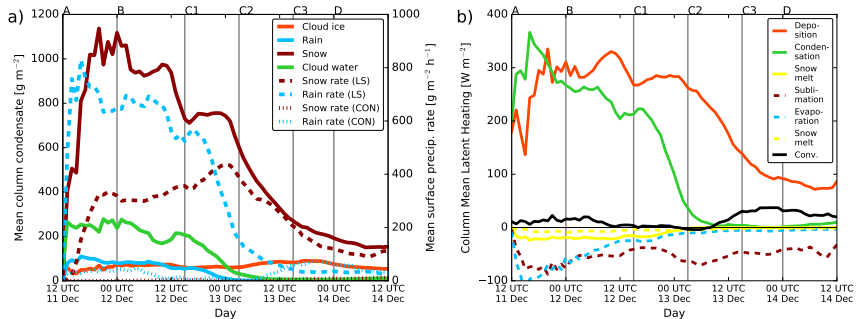


Figure 4.4: Time evolution of (a) column integrated condensate ( $\text{g m}^{-2}$ ) for the different hydrometeor species averaged over an area of  $1400 \text{ km} \times 1400 \text{ km}$  centered at the cyclone center (solid lines) and the mean surface precipitation rates in  $\text{g m}^{-2} \text{ h}^{-1}$  (dashed lines) averaged over the same area. Precipitation is partitioned into large-scale precipitation and convective precipitation. The location of the cyclone-following box is shown in the left panels in Fig. 4.5. (b) Column integrated latent heating and cooling averaged over the same area. The black line shows heating due to convection, the coloured lines correspond to in-cloud (solid) and to below-cloud (dashed) processes.

rainfall has increased to about  $60 \text{ g m}^{-2} \text{ h}^{-1}$ , whereas in the earlier stages there was no significant convective precipitation. A similar transition can be observed in the latent heating and cooling rates (Fig. 4.4b). At C1 latent heating due to ice and snow deposition and condensational heating are both very strong, with mean column integrated heating of  $220$  and  $270 \text{ W m}^{-2}$ , respectively. Twelve hours later (C2), when the system has occluded, heating due to condensation has dropped significantly, to only  $20 \text{ W m}^{-2}$ , whereas heating due to ice and snow deposition is still very strong at  $240 \text{ W m}^{-2}$ . Another twelve hours later (C3) heating due to condensation has dropped to almost zero, whereas heating due to ice and snow deposition is still moderately strong with  $140 \text{ W m}^{-2}$ .

At C1 the dominant below-cloud cooling process is snow sublimation with about  $-40 \text{ W m}^{-2}$ , followed by rain evaporation at  $-20 \text{ W m}^{-2}$ . Snow melting occurs mainly in-cloud with values of  $-15 \text{ W m}^{-2}$ . From C1 to C2, snow sublimation increases its magnitude to  $-70 \text{ W m}^{-2}$ , whereas evaporation and snow melting decrease in magnitude, keeping total below-cloud cooling approximately constant. Convective heating is close to zero at C1 and C2, but slightly increases to  $40 \text{ W m}^{-2}$  at C3, though also at this stage, heating is still dominated by large-scale depositional growth of ice and snow.

Summarizing, from stage C1 to C2, while occluding, the cyclone also makes a microphysical transition. Whereas at C1 in-cloud heating is partitioned almost equally between ice and snow deposition, and condensation, at stage C3, in-cloud heating is dominated by ice and snow deposition. Also the below-cloud cooling processes change from a mixture between snow sublimation, rain evaporation and snow melting at C1, to only snow sublimation at C3. How this microphysical change impacts the contributions to the cloud diabatic PV anomalies will be investigated in section 4.5.

#### 4.4 Frontal wave stage (C1)

The cyclone has a frontal wave structure at 15 UTC 12 December 2015 (stage C1, Figs. 4.5c,d; 4.6c,d). Figure 4.7a shows an enlargement of the box surrounding the cyclone shown in Fig. 4.5c. At 850 hPa, both the cold and warm fronts are characterized by a narrow ( $\sim 50 \text{ km}$ ) band of very high PV values of 5-8 PVU. To the south of the cyclone center a broader region with high PV air can be found. Here we analyze in detail the microphysical impact on the PV structures at this stage. Therefore, a cloud diabatic PV budget is constructed for the different microphysical processes (Table 2.1b) within the region shown in Fig. 4.7a. The analysis is based on a total number of 400,000 trajectories that are calculated

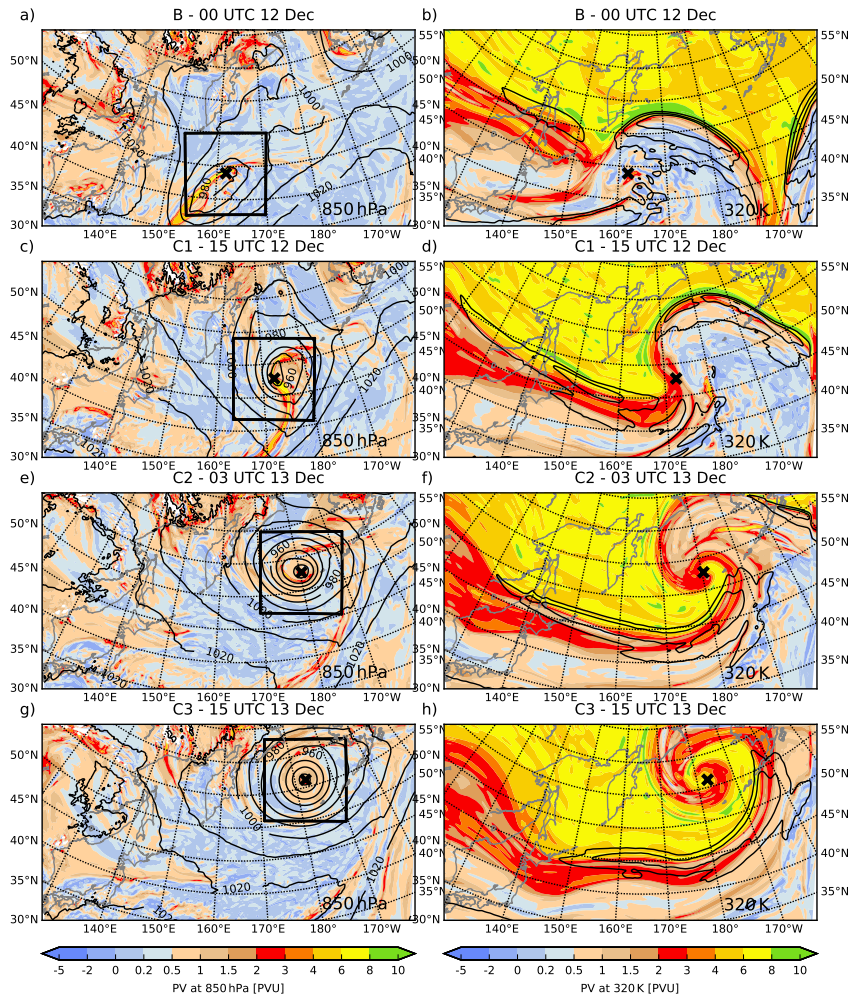


Figure 4.5: Time evolution of PV (PVU, colour shading) at 850 hPa (a,c,e,g) and 320 K (b,d,f,h), from stage B (a,b) to stage C3 (g,h) for the COSMO simulation. The cyclone center is indicated by a black cross. In (a,c,e,g) sea level pressure contours are labelled in hPa. In (b,d,f,h) contours show wind speeds at 300 hPa starting at  $50 \text{ m s}^{-1}$  at intervals of  $10 \text{ m s}^{-1}$ . Panels a, c, e and g show in addition the borders of the cyclone-following box that is used for calculating the different budgets.

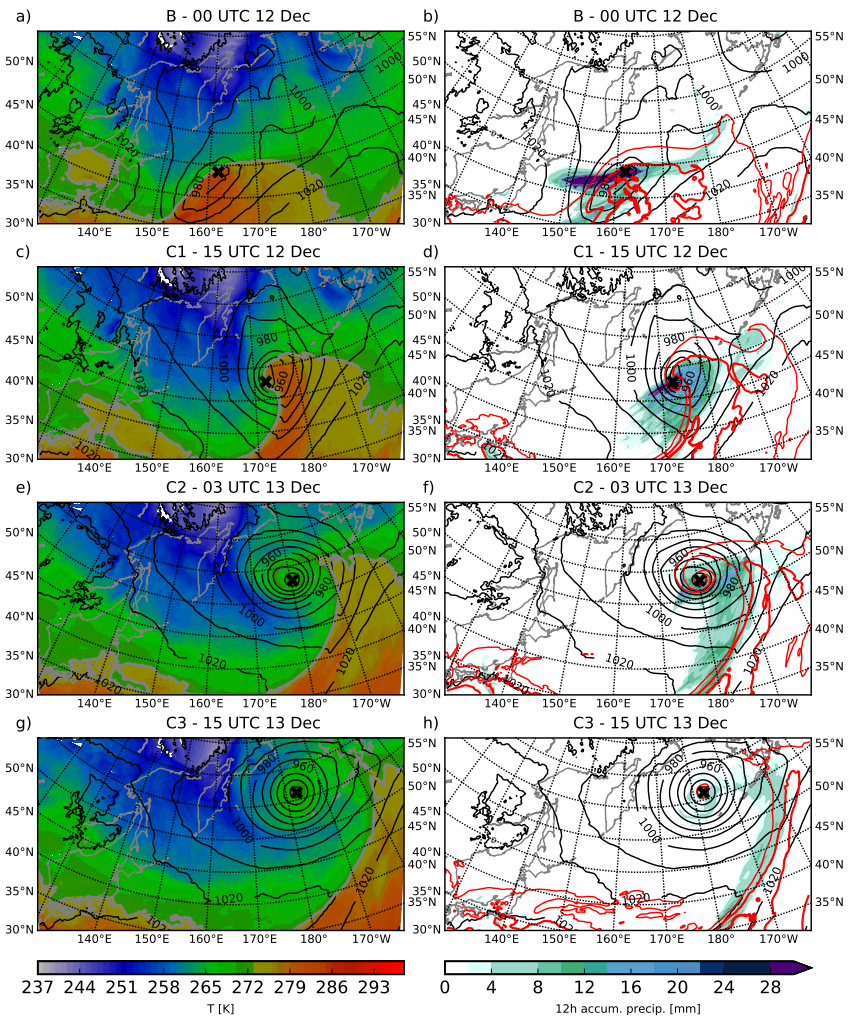


Figure 4.6: Time evolution of the cyclone from stage B (a,b) to stage C3 (g,h) with sea level pressure in black contours (labelled in hPa) for the COSMO simulation. Colour shading in (a,c,e,g) shows temperature at 850 hPa (K). Colour shading in (b,d,f,h) shows surface accumulated precipitation over the preceding 12 h and vertically integrated water vapour is shown in red contours at values of 10, 20, 30, 40  $\text{kg m}^{-2}$ .

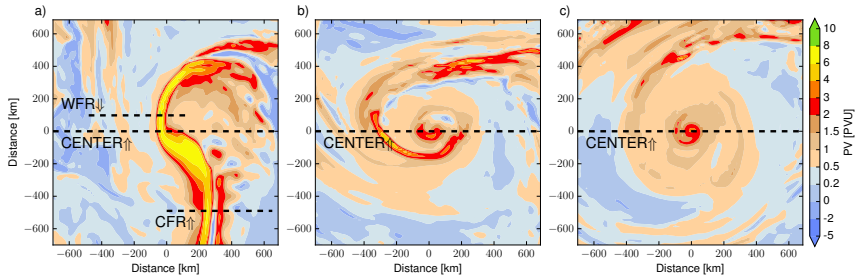


Figure 4.7: PV at 850 hPa in colours at three different stages: (a) stage C1 at 15 UTC 12 December, (b) stage C2 at 03 UTC 13 December and (c) stage C3 at 15 UTC 13 December for the COSMO simulation. Also shown are the locations of the cross sections, CENTER (in all panels) and through the warm (WFR) and cold fronts (CFR) (panel a). The arrows show the viewing direction for the different cross-sections.

24 h backward in time. Therefore, the diabatic PV budget represents for each gridpoint within this box the changes in PV of a parcel located at this gridpoint, due to a certain process  $i$  (see Table 2.1) over the past 24 hours.

Within this box, cross sections along the warm front (WFR) and cold front (CFR) are taken (see Fig. 4.7a for their exact locations) and analyzed in the next two subsections. In section 4.4.3 the anomalies in a wider region to the north of the cyclone center will be studied.

#### 4.4.1 Warm front structure

Figure 4.8a shows PV and potential temperature in a section across the warm front about 100 km north of the cyclone center (see Fig. 4.7a). The front itself is characterized by high PV values stretching from the surface approximately along the sloped isentropes (black contours) up to a height of almost 6 km. On top of this positive anomaly (P) low PV values and even small regions with negative values can be found (N). The melting layer (thick grey line) lies at about 2 km and quickly drops towards the surface over a distance of only approximately 50 km. The high PV stratospheric air comes down to about 6 km height in the western parts over the cold sector, whereas over the warm front the tropopause lies at a height of about 8-9 km. A strong low-level jet ( $>40 \text{ m s}^{-1}$ ) has its maximum at about 1 km height just to the west of the warm front.

The structure of clouds and precipitation (Fig. 4.8b) along the warm front is complex. Strong rain reaches the surface in a narrow band of approximately 50 km at the warm front. Moving upwards along the sloping isentropes, a mixed

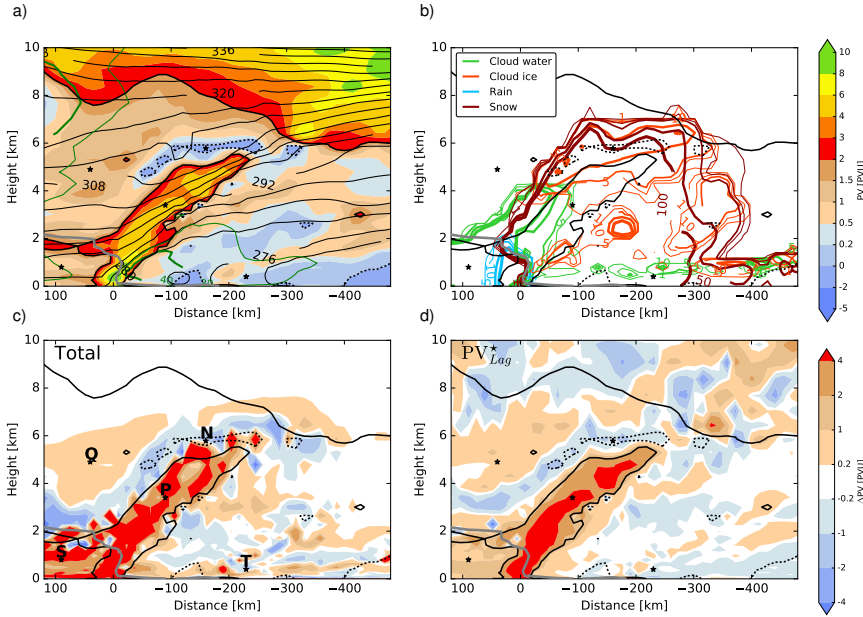


Figure 4.8: Cross-section WFR through the warm front at 15 UTC 12 December (stage C1) as shown in Fig. 4.7a. In each panel the  $0^{\circ}\text{C}$  isotherm is shown as a thick grey line, PV (PVU) is shown in colour in (a) and as 2 PVU (solid) and 0 PVU (dashed) black lines in (b,c,d). Further in (a), labelled black contours denote isentropes (K) and labelled green contours show wind speed ( $\text{m s}^{-1}$ ). (b) hydrometeor densities in coloured contours for cloud water (green), cloud ice (orange), rain (blue) and snow (red) at intervals of 1, 5, 10, 50 and  $100 \text{ g kg}^{-1}$ . (c) Shows the total DPV anomaly consisting of contributions from large-scale cloud, radiation and convection, (d) shows the total Lagrangian anomaly  $\text{PV}_{Lag}^*$  defined in Eq. 2.14. Different regions are indicated with stars in all panels, and are labelled in (c) as follows: P denotes the large and strong PV tower as bounded by the 2 PVU contour, N indicates the region of negative PV values, Q denotes the larger region with slightly positive CDPV contributions, S denotes the region below the melting layer (grey line) in the warm sector and T denotes the low levels (0-1 km) within the cold sector.

phase cloud extends from the melting layer at about 1 km height up to about 4 km. Above this level only snow and ice clouds can be found with their tops at about 7 km. The region with negative PV values (N) is embedded in the snow and ice clouds. To the west of the warm front, in the cold sector, snow reaches the surface. The clouds are mainly ice clouds, but up to a height of about 1 km small regions with mixed-phase clouds occur.

Figure 4.8c shows the total DPV consisting of contributions from the large-scale cloud scheme, radiation and convection, whereas Fig. 4.8d shows the total Lagrangian anomaly  $\text{PV}_{Lag}^*$  as defined in Eq. 2.14. Although in some regions there

are remarkable differences, overall, the total DPV field agrees well with  $PV_{Lag}^*$ . This is not trivial, since not all non-conservative processes are included in the budgets. For region Q the differences are very small. For regions N and Q, the total DPV field shows more structures and alternating patches with positive and negative contributions, whereas  $PV_{Lag}^*$  is much more smooth. These differences can be related to the calculation of the trajectories or the interpolation of the variables onto the trajectory positions. At low levels in both the warm sector and cold sector, there are clear differences between the total DPV and  $PV_{Lag}^*$ , which could be related to other PV non-conservative processes like surface heat fluxes and turbulence. Furthermore surrounding the tropopause and in the stratosphere, larger differences between the total DPV and  $PV_{Lag}^*$  arise. This is related to the relatively coarse vertical model resolution of about 800 m at these heights.

In the Appendix in Fig. C.1, the contributions of the large-scale cloud scheme, radiation and convection to the total DPV are shown. It becomes evident that the large-scale cloud scheme (Fig. C.1b) is the dominant contributor. Though, the slightly positive ( $> 0.2$  PVU) area Q is explained purely due to radiation (Fig. C.1d). Also the region with negative PV (N) experiences contributions from radiation. Although contributions from convection and radiation are widespread over the total DPV anomaly, their contributions are generally small (0.2-0.5 PVU) whereas the large-scale cloud scheme contributes much stronger with large regions with 1 to more than 4 PVU.

Summarizing, the overall PV changes over the past 24 hours are dominated by the large-scale cloud diabatic PV, even though locally radiation and convection can be important. Since the focus of this study is on the different microphysical processes, we will analyze those in further detail.

Figure 4.9 presents the different microphysical contributions to the CDPV. The positive cloud diabatic PV along the warm front (P) is mainly produced due to in-cloud condensation (Fig. 4.9a), depositional growth of cloud ice and snow (Fig. 4.9b) and below-cloud rain evaporation (Fig. 4.9d). Contributions due to depositional growth of cloud ice and snow are rather homogeneous, with contributions of 0.2-2 PVU over a larger region, whereas both condensation and rain evaporation show a larger variability. The negative contributions overlying the positive PV anomaly along the warm front (from region N and sloping downwards to the east) are mainly due to condensation (Fig. 4.9a) at altitudes between 2-4 km to the warm side of the front, and both due to condensation and depositional growth of cloud ice and snow at altitudes of around 6 km, with

the latter at slightly higher altitudes than the former. In-cloud snow melting (Fig. 4.9c) shows alternating positive and negative contributions within the positive anomaly. Below-cloud snow melting, on the other hand, contributes locally but very strongly at the surface warm front, between 0-1 km height, exactly in the region with the largest PV values (Fig. 4.8a). Snow sublimation (Fig. 4.9e) shows positive contributions at low levels in the cold sector, and negative contributions between 1-2 km height on the cold side of the front.



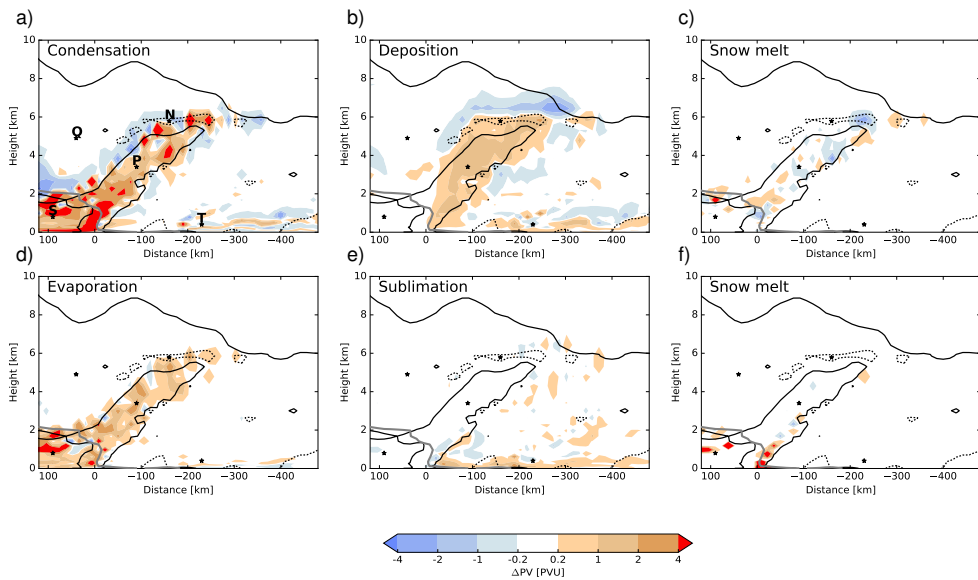


Figure 4.9: Cross-section WFR through the warm front at 15 UTC 12 December (stage C1) as shown in Fig. 4.7a, showing the different microphysical contributions to the total CDPV anomaly shown in Fig. C.1b. In each panel the 0°C isotherm is shown as a thick grey line, and black contours are 2 PVU (solid) and 0 PVU (dashed) isolines. Panels (a,b,c) show the in-cloud processes condensation, deposition of ice and snow, and snow melt, respectively. Panels (d,e,f) show below-cloud processes rain evaporation, snow sublimation and snow melt.

This cross section nicely illustrates the complex interplay of the microphysical processes in building the strong PV anomaly at the warm front. Influences of below-cloud processes can be found up to a height of about 6 km (evaporation of rain) and the melting of snow is responsible for a small but very strong anomaly near the melting layer.

#### 4.4.2 Cold front structure

Figure 4.10a shows PV and potential temperature in a section across the cold front about 500 km south of the cyclone center (see Fig. 4.7a). The PV field around the cold front has a complicated structure. Two strong low-level positive PV anomalies can be found. One located at the surface front (P1) with its maximum of about 5 PVU at a height of about 1 km. Another positive anomaly (P2) is located about 50 km to the west of the surface front (behind the front) within a region of very high static stability as can be seen by the kink in the melting layer indicating a region where temperature increases with height. A larger positive PV anomaly (P3) is located between 3 and 4 km to the west of the cold front. Low PV air is located to the west of the surface front, in the cold sector from the surface up to a height of 1-2 km (N1). Probably this is related to the strong destabilization from surface heat fluxes. Another region of low PV air (N2) can be found in between the two strong low-level positive PV anomalies stretching up to almost 9 km sloping eastwards with height. Several smaller negative anomalies (N3,N4,N5) can be found in the warm sector further to the east of the front up to a height of about 5 km. To the east of the front, a very strong jet ( $>50 \text{ m s}^{-1}$ ) extends from the stratosphere, down to a height of less than 1 km. Surface winds are strong with about  $30 \text{ m s}^{-1}$ . Behind (to the west of) the cold front no strong low-level jet can be found, though surface winds are only slightly less when compared to the eastern side of the front.

At the cold front itself strong rain reaches the surface in a band approximately 100 km wide (Fig. 4.10a). The cloud base is close to the surface whereas the melting layer is at about 2 km. The clouds are relatively shallow extending only up to a about 3-4 km at the front and are mixed-phase up to the cloud top. The cloud tops slope eastwards with height, and about 150 km to the east of the cold front the mixed-phase region extends to about 4.5 km with ice clouds and snow reaching up to an altitude of almost 10 km. Just to the west of the front, at the location of the positive PV anomaly P2, a cloud-free region can be found that is most probably related to strong subsidence occurring behind the front. Further

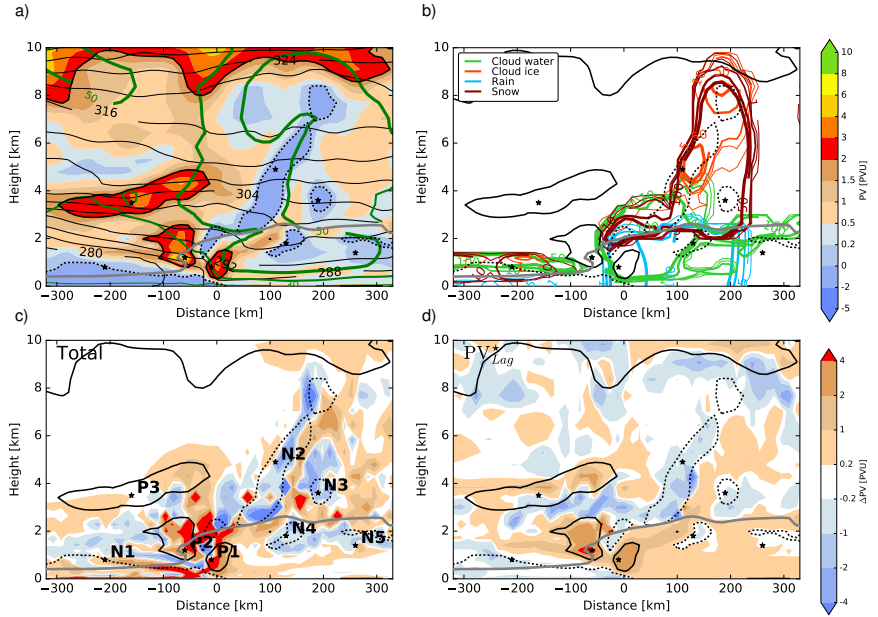


Figure 4.10: As in Fig. 4.8, but now for the cold front (CFR) as shown in Fig. 4.7a. The different positive (P1-P3) and negative (N1-N4) PV anomalies are labelled in (c) and indicated with a star in the other panels.

to the west of the front, into the cold sector, shallow (1.5 km vertical extent) precipitating mixed-phase clouds exist. Whereas the microphysical structure at and to the east of the cold front is homogeneous in the along-frontal direction (not shown), the structure of the clouds to the west is quite variable. A possible explanation could be the convective nature of the clouds and precipitation occurring in the cold sector.

Fig. 4.10c shows the total DPV consisting of contributions from the large-scale cloud scheme, radiation and convection, whereas Fig. 4.10d shows the total Lagrangian anomaly  $PV_{Lag}^*$  as defined in Eq. 2.14. We do not comment in detail on the differences here, but note that in general the total DPV is overestimated. Though, the anomalies P1, P2, P3 and N2, N3, N4 and N5 can all be identified in both the total DPV and in  $PV_{Lag}^*$ . In region N1 (the cold sector), the differences are larger, as was seen in the warm frontal cross section in the previous.

In the Appendix in Fig. C.2, the three different contributors to the total DPV are shown. As for the warm front, the large-scale cloud scheme (Fig. C.2b) is the dominant contributor to the total DPV (Fig. C.2a). Though, locally radiation and convection are important, in particular, P3 is produced by radiation and the

negative PV values in between the positive P1-P2 at around 2 km height seems to be related to the convective scheme.

Figure 4.11 shows the different in-cloud and below-cloud contributions (Table 2.1b) to the large-scale CDPV, for the section along the cold front. First it is noted that the overall regions where there are cloud diabatic contributions are characterized by both in-cloud and below-cloud processes. Furthermore, note that there are regions outside the clouds (e.g. P2 in Fig. 4.10b) where parcels have been influenced by in-cloud processes. And, vice versa, below-cloud processes have also impacted the PV of parcels that are at this moment located within the cloud (e.g., N2). There is a large overlap between the different processes. At some locations different processes act with the same sign and enhance each other, whereas in other areas the contributions cancel.

The small low-level anomaly located within the clouds at the front (P1) builds up mainly due to in-cloud condensation (Fig. 4.11a) and to a lesser extent below-cloud rain evaporation (Fig. 4.11b). The anomaly P2 is located in a cloud-free region, however it becomes evident that a multitude of microphysical processes have contributed to its strength. The structure of the contributions is very complex, in the region with PV above 3 PVU, almost all processes contribute both positively and negatively. For the strongest part of P2, situated at the melting layer, in-cloud and below-cloud snow melting (Fig. 4.11c,f) contribute strongly. For the large tilted negative anomaly (N2) stretching from approximately 2 to 8 km in-cloud condensation (Fig. 4.11a) and (in the upper region above 4 km) ice deposition (Fig. 4.11b) are the main contributors. The smaller anomaly N3 also has the strongest negative contributions from condensation. N4 exists due to in-cloud condensation (Fig. 4.11a) and snow melting (Fig. 4.11c) and some below-cloud rain evaporation (Fig. 4.11d).

Thorpe and Clough (1991) did a detailed analysis of cold fronts observed with high spatial resolution dropsondes. In terms of low-level PV maxima at the cold front, they found a maximum generally between 0.5 and 1.5 km height for the different cases studied. This is in accordance with our finding. Though, in none of the sections presented in Thorpe and Clough (1991) one can find the double structure (P1 and P2) as seen in Fig. 4.10. The occurrence of negative anomalies in the warm sector is in accordance with Thorpe and Clough (1991), which has earlier been noted by Roach and Hardman (1975) for warm-frontal rain bands.

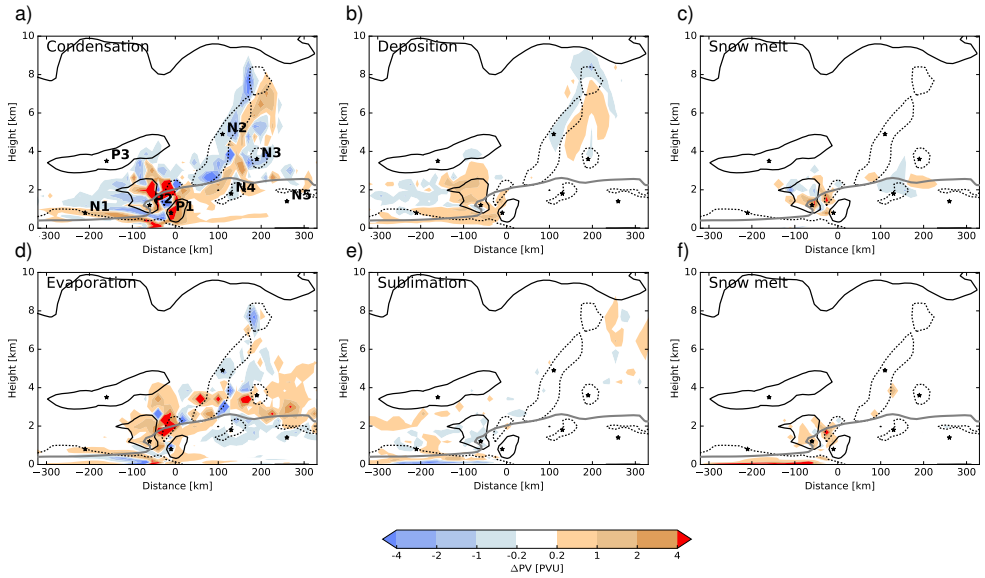


Figure 4.11: As in Fig. 4.10, but now showing the different microphysical contributions to the CDPV (Fig. C.2b). In each panel the  $0^\circ\text{C}$  isotherm is shown as a thick grey line, and black contours are 2 PVU (solid) and 0 PVU (dashed) isolines. Panels (a,b,c) show the in-cloud processes condensation, deposition of ice and snow, and snow melt, respectively. Panels (d,e,f) show below-cloud processes rain evaporation, snow sublimation and snow melt.

### 4.4.3 CDPV anomalies

#### Definition of CDPV anomalies

In the idealized study presented in Chapter 3, a threshold could be set on total CDPV and then the different anomalies could be identified by finding three-dimensionally connected regions. It was found that in the real case, the structure of CDPV is too complex to follow the same procedure. It would lead to a larger number of anomalies of small size. Therefore here another approach is used. The domain surrounding the cyclone is split into different meaningful regions based on height and on temperature regime. In the vertical, four distinct layers are defined as shown in Fig. 4.12a: the BL layer from 0-1 km, the LOW layer from 1-2 km, the MID layer from 2-6 km and the UP layer from 6 km to the model top at about 20 km. In addition, for the two lowest layers BL and LOW, we split into a cold sector (COLD) and a warm sector (WARM) with their boundary at  $\Theta_e = 300$  K (green line in Figs. 4.12a,b). In order to compare our results to the idealized simulation, where only the warm front was analyzed, we analyze only the region north of the cyclone center, which contains the warm front as shown in Fig. 4.12b (black line indicates the region boundary).

For each of the six regions we select all grid points having a CDPV value above 0.2 PVU and below  $-0.2$  PVU (as in Chapter 3) and group them together as the positive and negative anomalies, respectively. For convenience, in the rest of this Chapter, we will simply refer to e.g. the MID positive anomaly as the grid points within the region MID with CDPV values above 0.2 PVU.

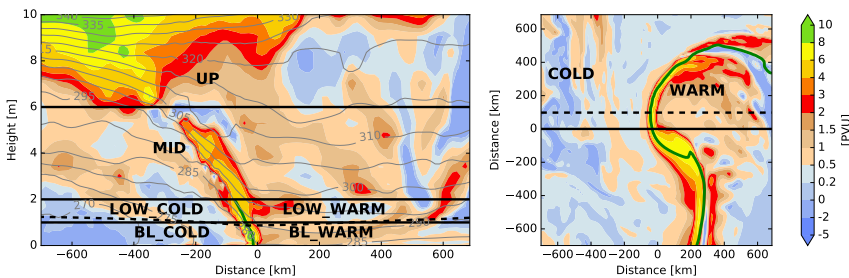


Figure 4.12: (a) section across the warm front showing the different vertical layers BL, LOW, MID and UP. The green line indicates  $\Theta_e=300$  K, splitting the two lowest layers (BL and LOW) into a cold (COLD) and warm (WARM) sector. Note that BL is chosen as the name of the lowest level, but does not necessarily correspond to the actual boundary layer height. Colours show PV (in PVU) and the dashed line indicates the 850 hPa level. (b) Same as in (a) but now at the 850 hPa level. The dashed line indicates the section in panel (a) and the black line indicates the southern boundary of the regions.

## Size and magnitude

For each anomaly the *size* is calculated as the total volume occupied by the anomaly and the *magnitude* is calculated as the mean value of CDPV within the anomaly. These two quantities are shown in Fig. 4.13 for the different anomalies at the frontal wave stage (i.e., 15 UTC 12 December; C1).

First, it can be noted that for almost all regions, the positive anomalies are stronger than their negative counterparts. This can be seen in the diagram by the clustering of the negative (blue) anomalies in the lower left part, with the positive (red) anomalies having generally larger magnitude. A clear exception are the UP anomalies, here the negative anomaly is stronger than the positive one. Moreover, their different locations in the diagram, indicate that their size-magnitude relation is very different. Whereas the negative UP anomaly is large in size and small in magnitude (0.5 PVU), its positive counterpart is about a factor 4 smaller in size, however much stronger with a magnitude of 1.5 PVU. For the

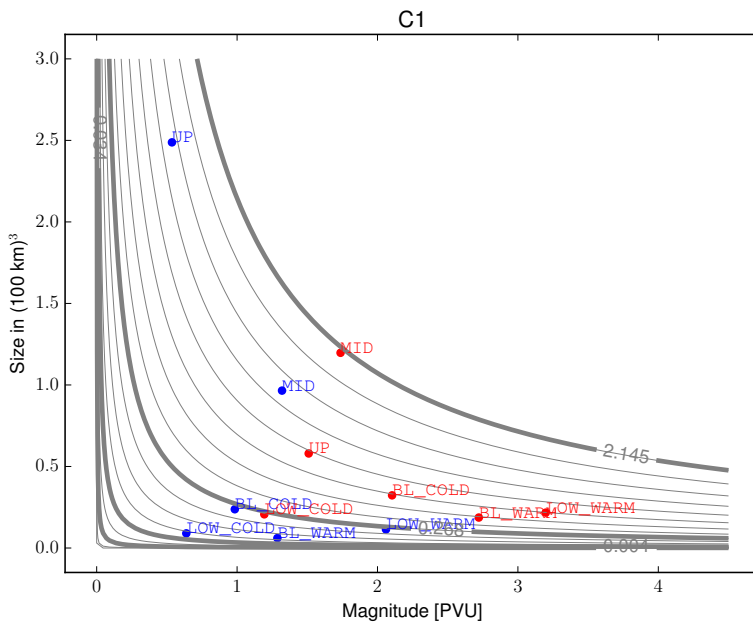


Figure 4.13: Anomaly magnitude (horizontal axis) in PVU vs. size (vertical axis) in  $(100 \text{ km})^3$ . All anomalies are labelled, positive anomalies are in red and negative anomalies are in blue (the absolute value of the magnitude is taken). The thick grey lines correspond to the strength of the reference “PV unit spheres” also shown in Fig. 4.14, additional thin grey lines denote constant strength.

other regions, the size-magnitude relation between the positive and negative anomalies is often similar, and therefore they are close to each other in the diagram. For instance, for the MID anomalies, the positive anomaly is strongest, its negative counterpart is weaker, due to both a weaker magnitude and a smaller size, but it is still the second strongest negative anomaly after UP. The low-level anomalies show a large variability in magnitude with the highest values for the positive anomalies on the warm side of the front (BL\_WARM and LOW\_WARM). Summarizing, at upper-levels the negative anomalies are large but weak, whereas the positive anomalies are small but strong, whereas at low levels both negative and positive anomalies are strong and moderately large with the strongest anomalies at the warm side of the front.

### Microphysical analysis: a new approach

A different way of analyzing and visualizing the microphysical contributions to the different anomalies is chosen here when compared to Chapter 3 where boxplots depicted how strong certain processes contributed to an anomaly. The motivation for a different visualization is that in this section, the importance of the different microphysical contributions over time will be investigated. It can be argued that both an increasing size of a certain contribution as well as an increasing magnitude of a certain contribution increases its importance. To reduce the complexity, the aforementioned *size* and *magnitude* are combined into a single quantity that will be called the anomaly *strength*. This quantity is calculated through integrating the DPV over the volume ( $V$ ) of the anomaly:

$$\langle CDPV \rangle = \iiint CDPV dV \quad (4.1)$$

Now this *strength*  $\langle CDPV \rangle$ , in units of PVU ( $100 \text{ km}^3$ ) can be decomposed into the different microphysical processes contributing to the anomaly:

$$\langle CDPV \rangle = \sum_{i=1}^n \langle CDPV_i \rangle \quad (4.2)$$

where  $CDPV_i$  can be any of the microphysical processes mentioned in Table 2.1b. In order to visualize the contributions from the different microphysical processes to the total anomaly, a pie chart is plotted. The fractions of each pie chart correspond to the different terms on the r.h.s. of Eq. 4.2, whereas the radius of each pie chart is calculated such that it corresponds to a hypothetical "PV unit sphere" having a CDPV value of 1 PVU everywhere but the same  $\langle CDPV \rangle$  value as the anomaly considered.

$$r_{pie} = \left( \frac{3 \langle CDPV \rangle}{4\pi} \right)^{\frac{1}{3}} \quad (4.3)$$



In principal, one of the individual terms on the r.h.s. of Eq. 4.2 can have the opposite sign to the anomaly. This means that this certain process counteracts the anomaly strength, it is therefore excluded from the pie chart. The relative size of these so-called counter contributions with respect to the total  $\langle CDPV \rangle$  is referred to as *counter*. As an example, consider the following: a CDPV anomaly of size  $1 \cdot (100 \text{ km})^3$  and magnitude 2.0 PVU would have the same *strength* ( $2 \text{ PVU} (100 \text{ km})^3$ ) as an anomaly of size  $4 \cdot (100 \text{ km})^3$  with a magnitude of 0.5 PVU.

For the anomaly LOW\_WARM (see Fig. 4.12) the pie chart (as described above) and the boxplot (as in Chapter 3) are shown in Fig. 4.14a and b, respectively. From the pie chart (Fig. 4.14a) it becomes evident that the dominant contributions to the anomaly strength come from in-cloud condensation (about 60%) and below-cloud (hatched) rain evaporation (about 30%). The anomaly has a magnitude of 3.2 PVU. From the boxplot (Fig. 4.14b) it can be seen that for in-cloud condensation the median contribution is about 1 PVU, whereas for below-cloud rain evap-

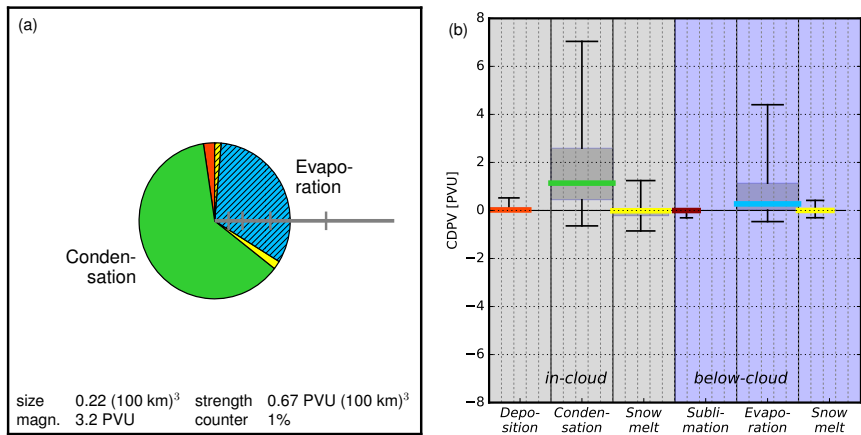


Figure 4.14: A comparison of two different ways of visualizing the microphysical contributions to the CDPV anomaly LOW\_WARM at stage C1, 15 UTC 12 December. (a) Pie chart with the radius scaled with anomaly strength  $\langle CDPV \rangle$  and the labelled fractions corresponding to the contributions  $\langle CDPV \rangle$ . Below-cloud processes are shown with hatching. Ticks on the axes correspond to  $r_{pie}$  values of 10, 20, 40 and 80 km. (b) Boxplot as in Chapter 3 showing on the left the in-cloud and on the right the below-cloud diabatic PV contributions for all grid points in the anomaly. For each process, the grid points with non-zero contributions for this process are selected to calculate the percentiles. The box extends from the 25th to the 75th percentile with the horizontal line indicating the median and the whiskers extending to the 5th and 95th percentiles. The width indicates the fraction of grid points of the total anomaly where this process has contributed to the PV anomaly.

oration the median contribution is only slightly positive. For both condensation and rain evaporation there is a large range in contributions, with even slightly negative contributions for the lower 95th percentiles. Both contributions are positively skewed with the 95th/75th percentiles reaching to 7 PVU/2.7 PVU and 4.5 PVU/1 PVU for condensation and rain evaporation, respectively. Because of this skewness the magnitude of 3.2 PVU for the anomaly as a whole is much higher than the sum of the median value of the contributions, which adds to about 1.5 PVU. The other processes contribute only weakly, but will be discussed since it provides insight to the different visualizations. From the boxplot we learn that deposition of ice and snow contributes to only about 60% of the grid points contained within the anomaly. Its contributions are positive and within a small range from 0-0.5 PVU. This leads to a very small contribution to the anomaly strength as shown in the pie chart. In-cloud snow melting has both positive and negative contributions, ranging from about  $-1$  to  $+1.5$  PVU. This leads to an even smaller contribution to the anomaly strength when compared to deposition of ice and snow. Below-cloud sublimation of snow contributes at only about 40% of the grid points of the anomaly. The contributions range from slightly negative to zero. Apparently, the  $\langle CDPV_i \rangle$  of this process is negative, and it weakens the positive anomaly strength  $\langle CDPV \rangle$  by approximately one percent. Therefore the value of counter is 1%. As will be shown later, counter contributions are rare, and when they exist, they are generally very small (0-4%) as in this case. Below-cloud snow melting has very weak contributions from about  $-0.5$  to  $+0.5$  PVU contributing at only about half the grid points contained within the anomaly. Therefore also the fraction in the pie chart is small, with less than 5%.

### Microphysical contributions

**BL\_COLD** Many different processes contribute to the positive anomaly BL\_COLD (see Fig. 4.15a). About half of the anomaly strength is produced due to below-cloud processes, with a dominant role of snow melting. The anomaly has a magnitude of about 2.1 PVU, whereas at this level the negative anomaly BL\_COLD (see Fig. 4.15b) has a magnitude of only about -1.0 PVU. This negative anomaly is formed mainly (40%) due to below-cloud snow sublimation, with smaller contributions from in-cloud condensational heating (30%), and depositional growth of ice and snow (25%).

**BL\_WARM** At the warm side of the front, the positive anomaly BL\_WARM (Fig. 4.15c) is strong with a magnitude of 2.7 PVU. For this positive anomaly the main contribution comes from condensational heating (60%) whereas rain

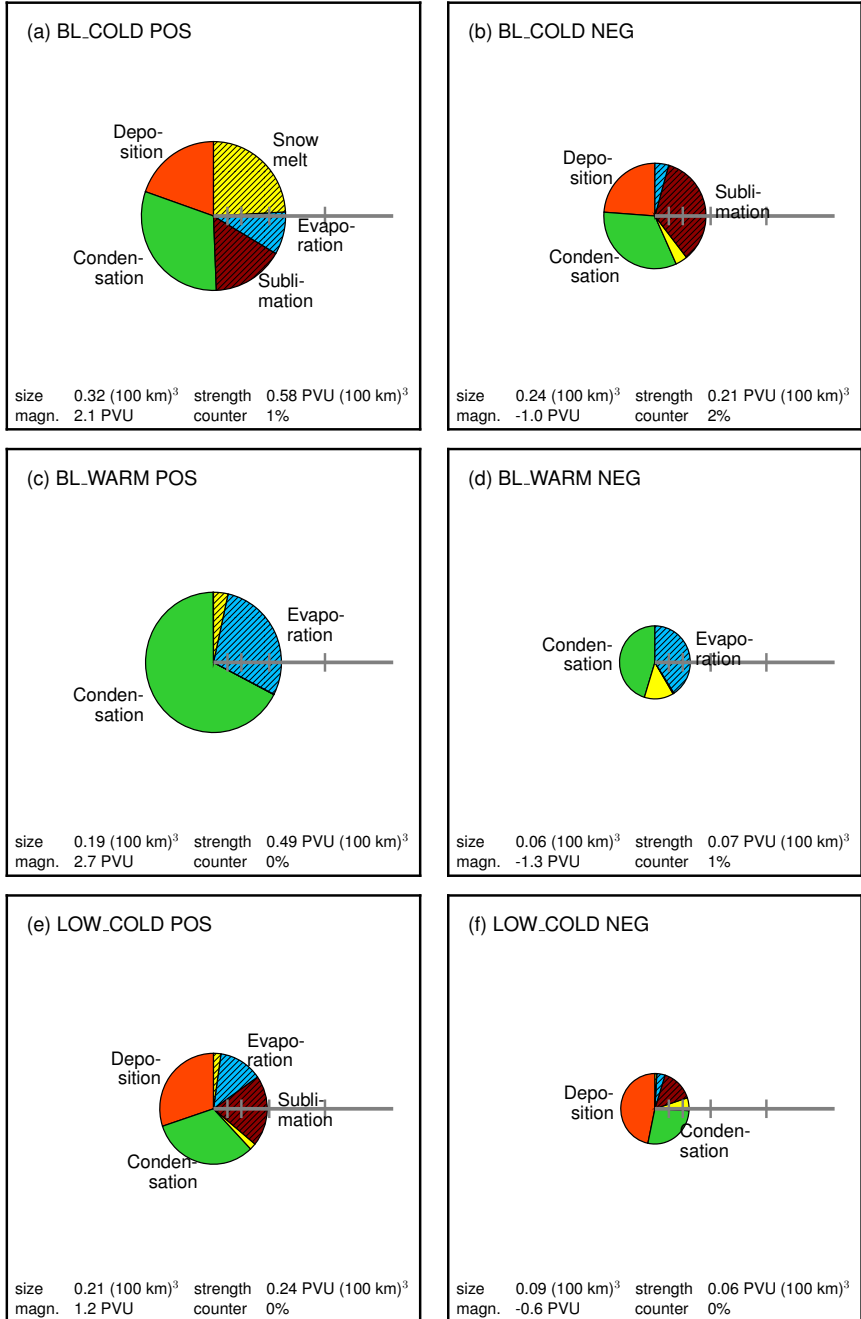


Figure 4.15: As in Fig. 4.14 at stage C1, 15 UTC 12 December for the positive and negative anomalies in the regions BL\_COLD (a,b), BL\_WARM (c,d) and LOW\_COLD (e,f).

evaporation also contributes significantly with about 30%. The negative anomaly (Fig. 4.15d) is smaller in size and in magnitude, making its strength almost an order of magnitude smaller. Rain evaporation and condensation contribute most (each about 40%) to this anomaly, with also about 15% contributions from in-cloud snow melting.

**LOW\_COLD** The positive anomaly LOW\_COLD (Fig. 4.15e) has the strongest contributions from in-cloud depositional growth of ice and snow and condensation. In addition, below-cloud rain evaporation and snow sublimation contribute to the anomaly, each with about 20%. It has a moderate magnitude of 1.2 PVU. The negative anomaly (Fig. 4.15f) is weak with a magnitude of only  $-0.6$  PVU, making its strength a factor 4 smaller compared to the positive anomaly in this region.

**LOW\_WARM** For the positive anomaly LOW\_WARM (Fig. 4.16a) again in-cloud condensation and below-cloud rain evaporation are the dominant contributors, as in BL\_WARM. This anomaly has the largest magnitude of all anomalies with 3.2 PVU. The negative anomaly (Fig. 4.16b) has also a large magnitude of  $-2.1$  PVU, though it is only half the size of the positive anomaly. As for its positive anomaly, the microphysical contributions to the negative anomaly LOW\_WARM, are mainly condensation and evaporation, with a minor role for snow melting.

**MID** The positive MID anomaly (Fig. 4.16c) is the strongest anomaly, mainly due to its size, since its magnitude of 1.7 PVU is not as large as the positive anomaly LOW\_WARM. This anomaly has contributions of about 45% from in-cloud condensational heating, whereas ice and snow deposition and below-cloud rain evaporation each contribute about 25% to its strength. The negative anomaly in this region (Fig. 4.16d) is a bit smaller in both size and magnitude. It exists for 80% due to condensational heating, and has smaller contributions from below-cloud rain evaporation (10%) and snow sublimation ( $<10\%$ ).

**UP** The upper-tropospheric positive anomaly UP (Fig. 4.16e) has a moderate magnitude of 1.5 PVU. This anomaly owes 50% of its strength to in-cloud condensational heating, and 20% due to in-cloud ice and snow deposition. Even at altitudes above 6 km, the below-cloud processes rain evaporation and snow sublimation together contribute about 25% to the positive PV anomaly. Apparently the signal of below-cloud rain evaporation, has been transported all the way up into the clouds. The negative anomaly UP is a factor of 5 larger

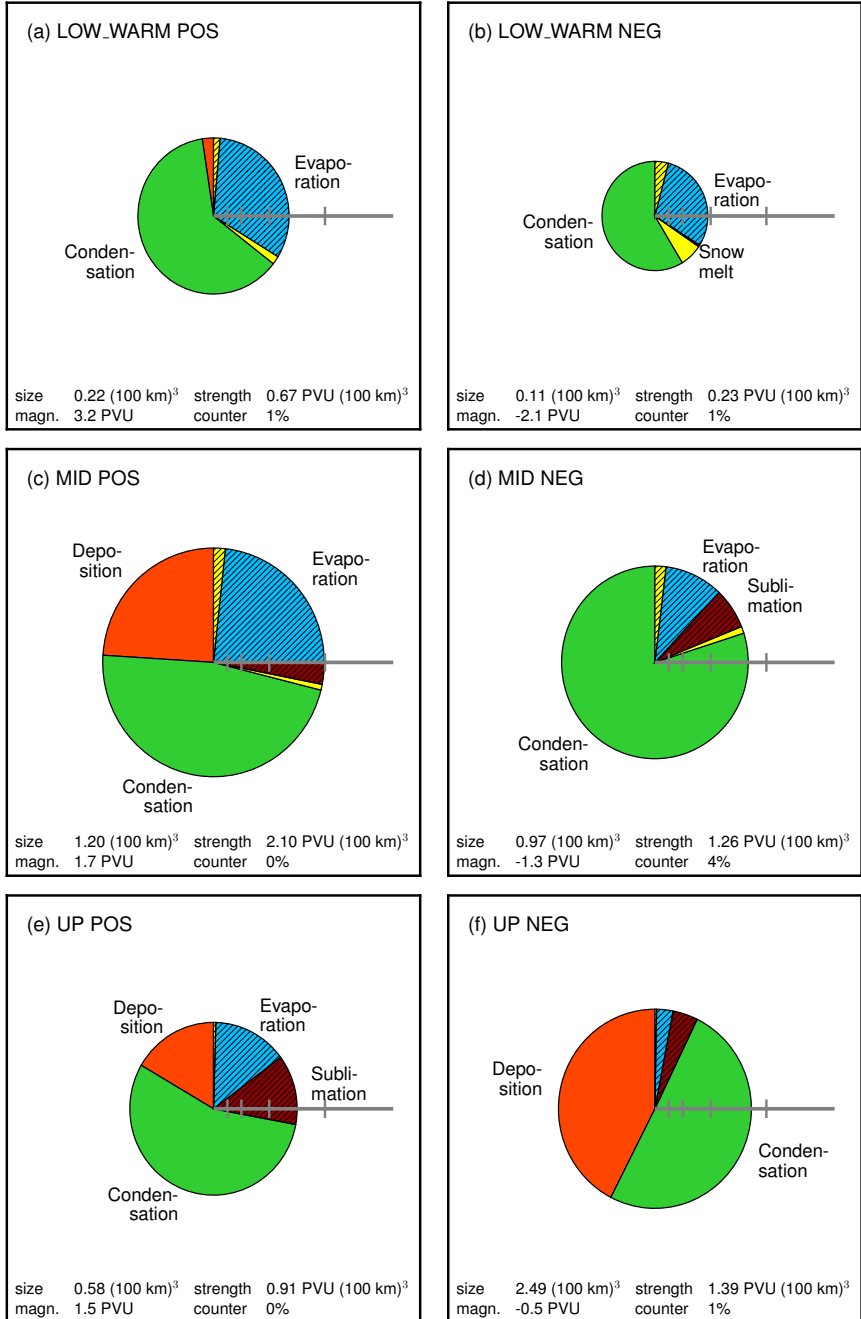


Figure 4.16: As in Fig. 4.15 at stage C1, 15 UTC 12 December for the positive and negative anomalies LOW\_WARM (a,b), MID (c,d) and UP (e,f).

compared to the positive anomaly in this region, however a factor of 3 weaker. For this negative anomaly (Fig. 4.16f) condensation and depositional growth of ice and snow contribute about 50% and 40%, respectively. There are very small contributions from the below-cloud processes rain evaporation and snow sublimation.

Summarizing, at low levels below-cloud processes contribute significantly (30-50%) to both the positive and negative anomalies. At the higher levels (MID and UP) below-cloud processes contribute significantly to the positive anomalies, but contributions to the negative anomalies shrink, to 20% at MID and <10% at UP. The largest magnitudes of CDPV anomalies are found at the warm side of the front at low levels. For these “warm” low-level anomalies, the main contributions are in-cloud condensation and below-cloud rain evaporation, whereas at the same level on the cold side, all different processes contribute to both the positive and the negative anomalies.

#### Detailed analysis of the positive upper-level anomaly

The aim of this section is to study in detail the establishment of the positive upper-level PV anomaly. When analyzing the total cloud diabatic PV rate along the trajectories (Fig. 4.17a) we learn a few things. First, we find that even though the trajectories establish a positive anomaly, along the way they also experience negative cloud diabatic PV rates. Second, along most of the path the cloud diabatic PV rates are near-zero, indicating that trajectories gain their PV during a relatively short time. A more detailed analysis of timescales of PV modification

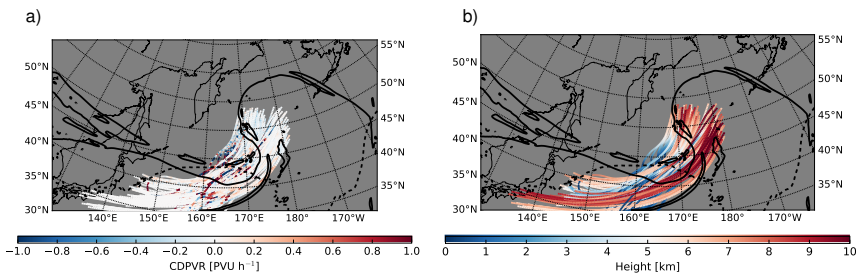


Figure 4.17: The trajectories starting at 15 UTC 11 December ending in the positive anomaly UP at 15 UTC 12 December. Only 1 out of 100 randomly chosen trajectories are shown. In (a) the trajectories are colored according to their cloud diabatic PV rate ( $\text{PVU h}^{-1}$ ), whereas in (b) the colors denote the trajectory height (m). In both panels the  $0^\circ\text{C}$  isotherm at 850 hPa at 15 UTC 11 December (start time of the trajectories) is shown with a dashed black line, and the intersection of the 2 PVU surface with the 320 K isentropic surface is shown as a solid black line at 15 UTC 12 December (end time of the trajectories).

along the trajectories will be presented in section 4.5.3.

Based on trajectory ascent and their origin (Fig. 4.17b), two different coherent bundles of trajectories can be identified, both ending in the positive upper-level PV anomaly. One bundle originates from low levels well within the warm air mass located roughly at  $30^{\circ}\text{N};160^{\circ}\text{E}$  at 15 UTC 11 December. This bundle strongly ascends as the cyclone develops and is part of the warm conveyor belt. The other bundle ends further east at 15 UTC 12 December, however its origin is much more to the west, above the low-level baroclinic zone. This bundle shows only a very weak ascent. We will refer to the former bundle as *strong*, and to the latter bundle as *weak*.

We select the different coherent trajectory bundles to study the evolution of cloud diabatic PV rates over time for each bundle. The histogram of trajectory ascent for the full bundle (Fig. C.3 in the Appendix) is characterized by two peaks separated from each other. A threshold value of 6 km ascent is used to select the two different coherent bundles.

In Fig. 4.18 the cloud diabatic PV rates are presented for each bundle separately. Bundle *strong* experiences strongest positive contributions from in-cloud condensation (green line) with values of  $0.1\text{--}0.3\text{ PVU h}^{-1}$  from about  $t = 0\text{ h}$  to  $t = 18\text{ h}$  when rates turn slightly negative for a short period of time. The second-most important process for the bundle *strong* is the below-cloud evaporation of rain, which has only small rates of  $0.05\text{ PVU h}^{-1}$  but acts over an equally long period of time as condensation. For the bundle *weak* the diabatic PV rates are much smaller. Interestingly, here the main positive contributions occur slightly later in time compared to *strong* and they are mainly due to in-cloud deposition of ice and snow and below-cloud sublimation of ice and snow. Both processes are characterized by diabatic PV rates of only about  $0.04\text{ PVU h}^{-1}$ .

Summarizing, the positive UP anomaly owes its existence due to both strong

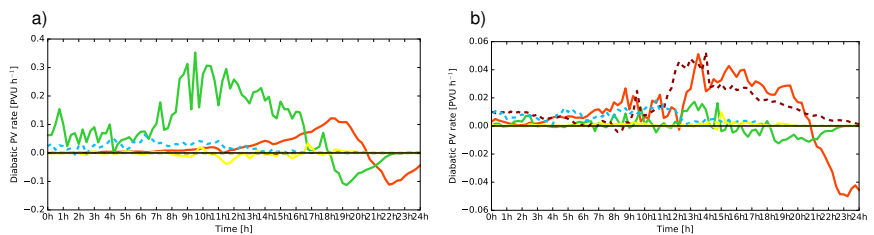


Figure 4.18: Time evolution of the mean value of the cloud diabatic PV rates along the trajectory bundles (a) *weak* and (b) *strong* for the different in-cloud (solid lines) and below-cloud (dashed) processes.

vertical transport (warm conveyor belt) of remotely produced diabatic PV (mainly below-cloud rain evaporation and in-cloud condensation) and the more local PV production from a combination of in-cloud depositional growth of ice and snow and below-cloud snow sublimation.

## 4.5 Time evolution (C1-C3)

As shown in section 4.3.2 the rapid intensification phase of the cyclone during the crossing of the jet axis is also characterized by an abrupt change in the microphysics. Initially (right after stage C1) condensational heating drops to almost zero at stage C2. This is followed by a decrease in heating due to depositional growth of ice and snow from stage C2 to C3 by about 70%. The aim of this section is to understand temporal changes of the CDPV in terms of its structure and microphysical contributions during the transition phase of the cyclone. Subsection 4.5.1 shows how the vertical structure of CDPV, clouds and precipitation changes. In subsection 4.5.2 it will be shown how the microphysical contributions to the anomalies evolve. This section concludes with a comparison of the Lagrangian and Eulerian perspective of microphysical PV modification in section 4.5.3.

### 4.5.1 *Cyclone structure*

The structure of CDPV and clouds and precipitation at C1 along the warm (WFR) and cold fronts (CFR) were discussed in section 4.4. The cross sections presented in Fig. 4.19a,b are taken through the cyclone center (CENTER). At stage C1, the cross section is just south of the WFR cross-section. As can be seen in Fig. 4.19a the diabatically produced PV (CDPV up to 6 PVU) is connected to the high-PV air of stratospheric origin at a height of approximately 6 km. There are slightly negative CDPV contributions on top of the positive CDPV anomaly, as was the case for the section across the warm front. At this time the surface warm front runs through the cyclone center. At low levels (up to about 2 km) large CDPV values can be found in a region stretching from the front about 200 km eastwards. Further east, within the warm sector, more alternating patches of positive and negative CDPV can be found. The cloud structure (Fig. 4.19b) along the WFR changes from liquid (at low levels on the warm side) to mixed phase roughly between 1 and 4 km height, to ice phase between 4 and 6.5 km. Just east of the cyclone center, only water clouds can be found, extending to about 2 km height. Further into the warm sector (from about 200 km and eastwards) again deeper ice clouds can be found, even up to a height of about 10.5 km. Both in this region



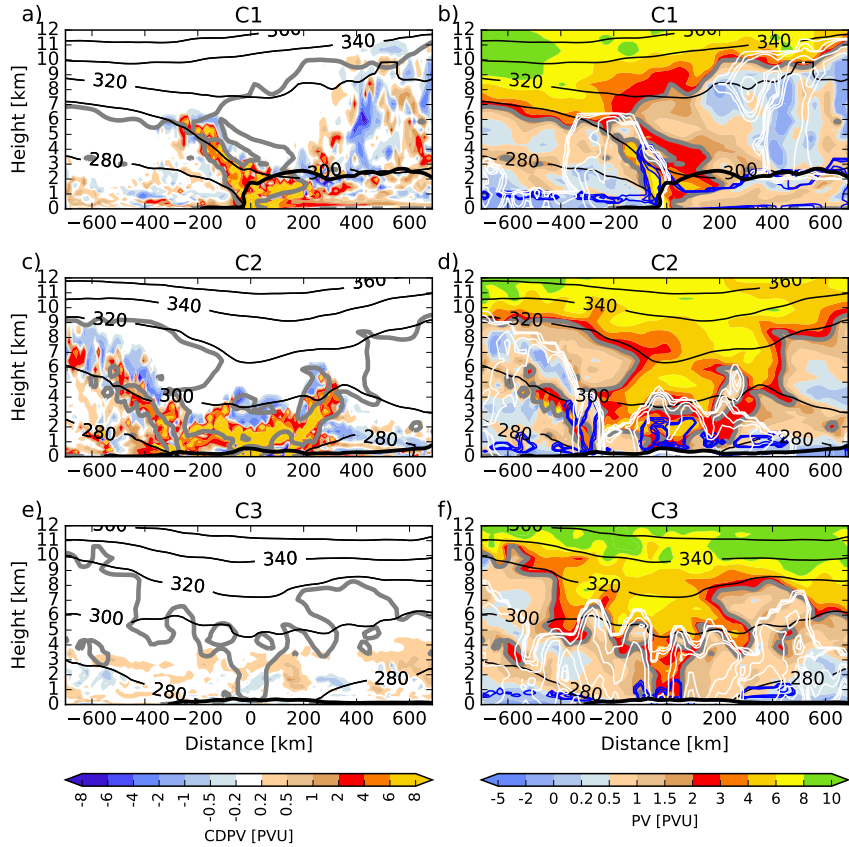


Figure 4.19: Time development of CDPV, PV and condensate along cross sections through the cyclone center (CENTER, see Fig. 4.7) for (a,b) stage C1 at 15 UTC 12 December, (c,d) stage C2 at 03 UTC 13 December and (e,f) stage C3 at 15 UTC 13 December. The left panels (a,c,e) show CDPV (PVU) in colours and labelled isentropes (K). The right panels (b,d,f) show PV (PVU) in colours, liquid and ice water content in blue and white contours respectively with contour intervals as in Fig. 4.10b. In all panels, the 2 PVU contour and the  $0^{\circ}\text{C}$  isotherm are shown as thick grey and black contours, respectively.

as well as on top of the warm front, the ice-clouds reach to slightly above the tropopause.

Twelve hours later (C2) the cyclone has occluded, thereby changing from a strongly baroclinic to a more barotropic system and enters a less diabatic phase (see Fig. 4.4). As can be seen in Fig. 4.19d, the melting layer is now close to the surface. The occluded front is located about 300 km west of the cyclone

center. Along the front, a region of high PV ( $>2$  PVU) can be found tilting westwards with height, reaching up to about 5 km. This region is characterized by strongly positive CDPV values. Moving further up and westwards along the 300 K isentrope the structure becomes more broken with also patches of relatively low PV air in between. This pattern is also represented in the CDPV field, with alternating negative and positive CDPV values. On top of this region a layer of about 1 km vertical extent with low ( $<0.5$  PVU) PV values can be found, disconnecting the diabatic high PV air from the stratospheric reservoir. This region is associated with negative CDPV contributions (Fig. 4.19c) and is located within the ice cloud. At lower levels along the fronts, a vertically oriented mixed-phase cloud can be found stretching from the surface up to about 4 km height. On top of this cloud and further westwards, ice clouds extend up to a height of about 9 km. In the cyclone center, a broad and strong PV tower can be found, reaching down to only 1 km above the surface. The bottom part of this region is characterized by high ( $>6$  PVU) CDPV values. Within this PV tower two regions of low PV air can be found, one above the cyclone center, and another one about 200 km eastwards. These regions are characterized by mainly negative CDPV contributions (Fig. 4.19c) that are located close to the upper edge but still contained within the ice clouds. A region of mixed-phase clouds extends from the surface up to about 2.5 km within the cyclone center. Ice clouds overly this region, reaching to about 4.5 km. Within these ice clouds regions of relatively low PV ( $<2$  PVU) can be found that are related to negative CDPV (Fig. 4.19c).

At stage C3 (Fig. 4.19f) the cyclone has fully occluded and the PV tower (when defined as regions where  $PV > 2$  PVU) has become narrow, stretching down almost to the surface in the cyclone center. Mainly ice-clouds can be found surrounding the cyclone center, with locally embedded shallow (up to 1.5 km) mixed-phase clouds. The tropopause level surrounding the cyclone center has a wavy structure coinciding with the ice-clouds. The CDPV values are very low, which is probably the case because the PV was diabatically produced longer than 24 hours before this timestep (i.e. before stage C1). This is a limitation, and should be kept in mind when interpreting Figs. 4.19e,f.

#### 4.5.2 CDPV anomalies

In this subsection the changes over time for the cloud diabatic PV anomalies will be presented. The next paragraph will discuss how the anomaly strengths - determined by their sizes and magnitudes - change over time. This is followed

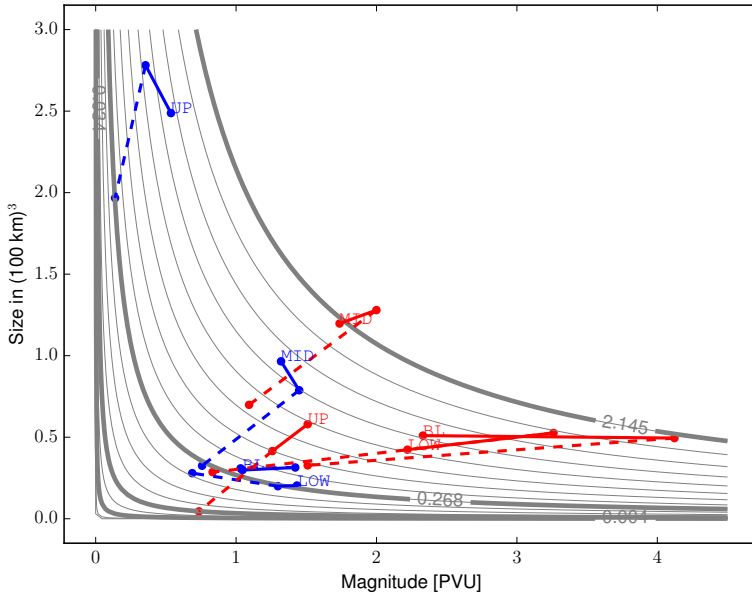


Figure 4.20: Decomposition of anomaly strength into magnitude (horizontal axis) in PVU and size (vertical axis) in  $(100 \text{ km})^3$  as in Fig. 4.13, now showing the time evolution from stage C1 (15 UTC 12 December 2015) to stage C2 (03 UTC 13 December 2015) in solid lines and from stage C2 to stage C3 (15 UTC 13 December 2015) in dashed lines.

by small paragraphs discussing per region for each anomaly the changes in microphysical contributions.

### Size and magnitude

As can be seen in Fig. 4.20, from C1 to C2, all positive anomalies - except for UP - increase their strength, mainly due to an increase in magnitude and to a lesser extent due to an increase in size. The BL and LOW anomalies, increased their magnitudes to 4.2 and 3.2 PVU, respectively. The positive MID anomaly remains the strongest anomaly due to both a moderate magnitude and a moderate size. Whereas the low-level positive anomalies significantly increase their magnitude, the low-level negative anomalies show only small increases in magnitude, and - like the positive anomaly - hardly any changes in size. The MID anomaly slightly increases magnitude while shrinking in size, whereas the UP anomaly slightly decreases magnitude, but grows in size. The negative MID and negative UP anomalies now have a similar strength (follow the strength-isolines in the size-magnitude diagram).

At stage C3 all anomalies have weakened considerably. As mentioned above, for stage C3 the integration time of 24 hours is probably too short to capture the diabatic effects that occurred before. So the results for stage C3 therefore need to be interpreted with this in mind. The positive MID anomaly is still the strongest anomaly. The positive and negative anomalies all have a similar size of about  $0.3 (100 \text{ km})^3$  and magnitudes ranging from 0.8 PVU to about 1.6 PVU. The negative UP anomaly has shrunk about a quarter in size and further decreased its magnitude to about 0.3 PVU. The positive UP anomaly has become negligibly small. Note that at all stages in the region UP, the negative anomaly is rather large in size, but small in magnitude, whereas the positive anomaly is large in magnitude, but therefore small in size.

Summarizing the above, the positive anomalies show the strongest variation of strength over time, whereas the strength of the negative anomalies remains relatively constant. Most anomalies reach their largest strength at C2 before they weaken considerably at C3. The positive UP anomaly shows a remarkable behaviour, it is smaller but has a higher magnitude than the negative anomaly in the same region, and it is the only anomaly that shrinks from C1 to C2, probably related to the fact that ascending parcels don't reach to high altitudes anymore at C2.

### Microphysical contributions

In the following paragraphs, the changes of the microphysical contributions during the transition phase will be presented. For each region, the positive anomaly is discussed first, followed by the negative anomaly. Since the cyclone has occluded at stages C2 and C3, we can no longer distinguish between a warm and cold sector, and therefore we analyze the regions BL and LOW as a whole, whereas in section 4.4.3 we analyzed separately the warm and cold sectors for these regions.

**BL** The BL positive anomaly at C1 (Fig. 4.21a) has about half its contributions from condensation, about 25% due to rain evaporation, closely followed by snow melt, deposition of ice and snow and sublimation. The BL anomaly reaches its largest strength during C2 (Fig. 4.21c), which is explained by a strong increase in magnitude from 2.3 to 4.1 PVU, while its size remains fairly constant. Snow melting contributes very strongly at stage C2, explaining about 50% of the anomaly strength. Condensation and ice and snow deposition contribute about 20% and 15%, respectively, with smaller contributions from rain evaporation and

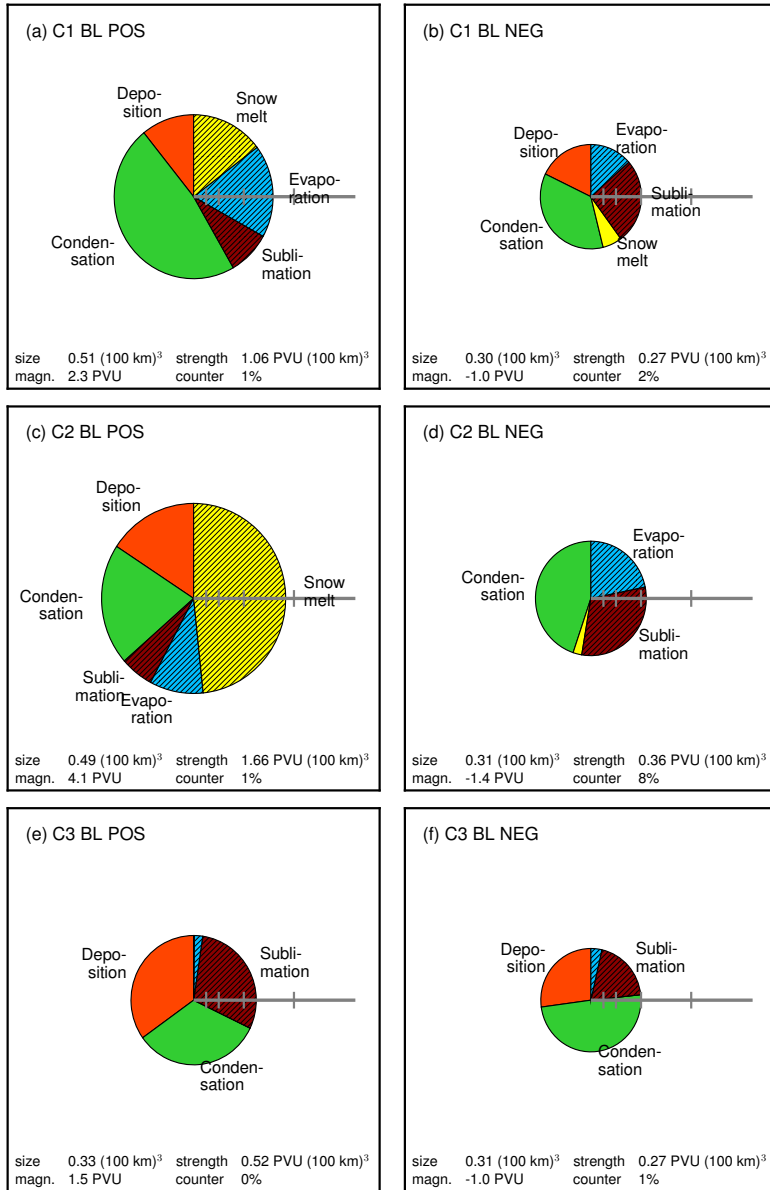


Figure 4.21: As in Fig. 4.16, now showing the time evolution (C1-C3) from top to bottom for the positive (left) and negative (right) anomaly BL.

sublimation. At stage C3 the positive BL anomaly has shrunk about one third in size and decreased in magnitude to 1.5 PVU, making its strength only about a third from the strength at stage C2. The role of snow melting has vanished completely. However, snow sublimation has become increasingly important contributing now about 30% to the strength of the anomaly, likewise for deposition of ice and snow and condensation. For the in-cloud processes, the relative importance of depositional growth of ice and snow compared to condensation increases steadily from C1 to C3. The sudden increase of snow melt from C1-C2, before completely vanishing at C3, is remarkable and needs to be further investigated.

Whereas the positive anomaly BL showed significant changes in both magnitude and size, its negative counterpart shows small changes in magnitude, while hardly changing size. The anomaly reaches its largest magnitude at C2, like the positive anomaly. In-cloud condensation and below-cloud snow melting contribute strongly from C1-C3. Evaporation increases from C1-C2, but vanishes at C3. Ice deposition is only present at C1 and C3 and not at C2.

**LOW** At stage C1 the LOW positive anomaly (Fig. 4.22a) owes more than half its strength to in-cloud condensation, and about a quarter of its strength to below-cloud rain evaporation. Deposition of ice and snow and sublimation both contribute less than 10%. Like the positive BL anomaly, the positive LOW anomaly reaches its largest strength at C2 (Fig. 4.22c), increasing its magnitude from 2.2 to 3.3 PVU while growing about 24% in size. As in the region BL, below-cloud snow melting increases its contributions, however not as much, contributing just 15% at C2. Condensation is still the most important contributor, though its relative contribution decreases to about 40%, whereas ice deposition increases to about 15%. Below-cloud rain evaporation slightly decreases its relative contribution to about 20%, whereas below-cloud snow sublimation slightly increases its relative contribution. From stage C2 to C3 (Fig. 4.22e), the anomaly decreases in size by a factor of 2, whereas its magnitude decreases even more, from 3.3 PVU to only 0.8 PVU. The only process that kept its absolute strength is snow sublimation, thereby increasing its relative contribution to the positive anomaly LOW to about 40% at C3. Ice deposition further increased its relative contributions to about 35%, whereas contributions from condensation have almost vanished. Also rain evaporation hardly contributes to the positive LOW anomaly at stage C3. Overall we note that similar processes contribute to the anomalies in the region LOW when compared to region BL, as can be seen by comparing Fig. 4.22 with Fig. 4.21.

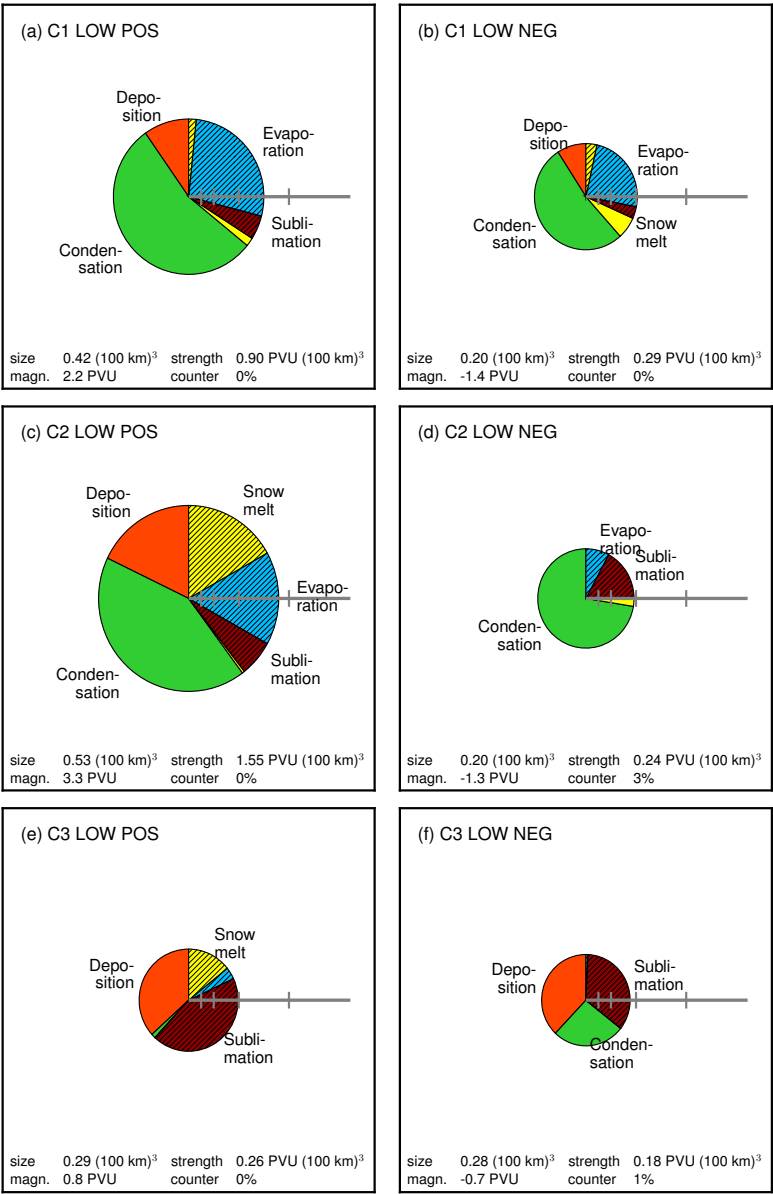


Figure 4.22: As in Fig. 4.21, now showing the time evolution (C1-C3) from top to bottom for the positive (left) and negative (right) anomaly LOW.

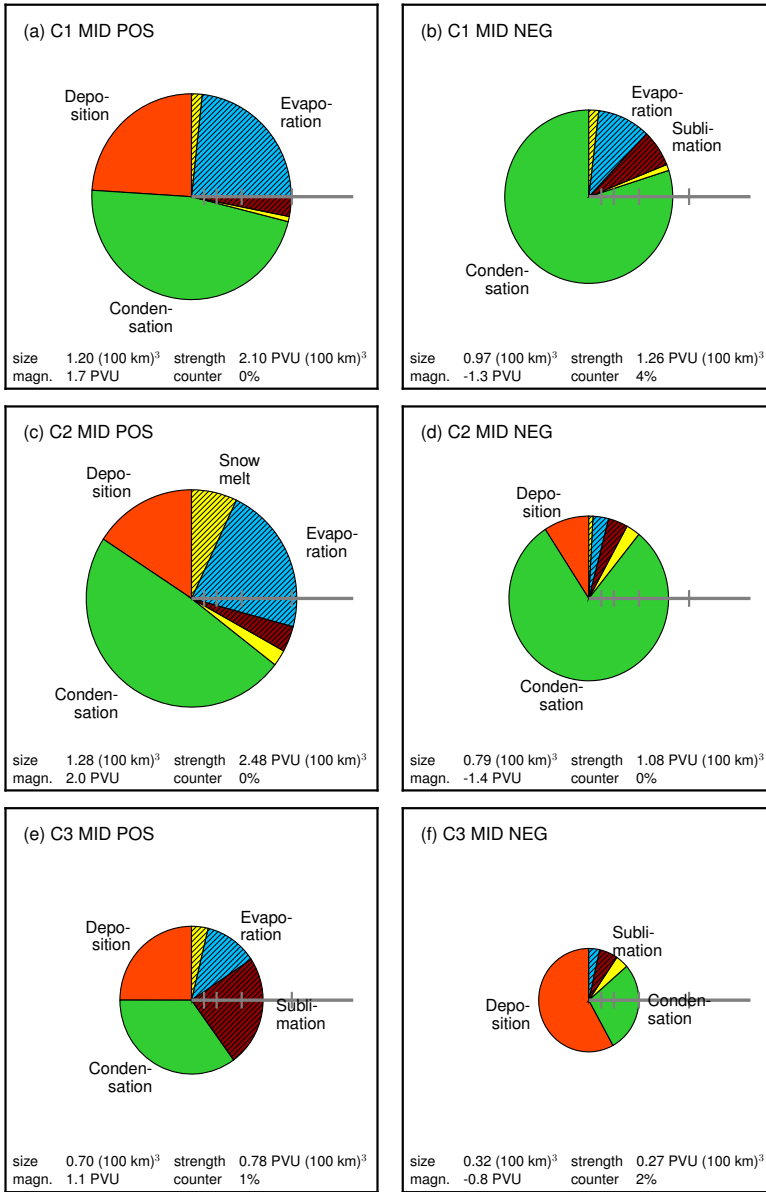


Figure 4.23: As in Fig. 4.22, now showing the time evolution (C1-C3) from top to bottom for the positive (left) and negative (right) anomaly MID.



**MID** The MID positive anomaly (Fig. 4.23a) also reaches its largest strength at C2, which then strongly decreases. The relative contributions hardly change from C1 (Fig. 4.23a) to C2 (Fig. 4.23c). Only the relative contribution from condensation compared to depositional growth of ice and snow shows a slight increase. This is remarkable, since the opposite was found for the lower positive anomalies BL and LOW (Figs. 4.21,4.22). From C2 to C3 (Fig. 4.23f) the relative contributions from the in-cloud processes deposition of ice and snow compared to condensation increases, now each contributing about 30% to the MID positive anomaly. For the below-cloud processes the relative contribution of sublimation compared to evaporation increases. At C3 sublimation contributes about 25%, whereas evaporation contributes only about 10%. So overall, from C2 to C3 the relative contributions of below-cloud versus in-cloud processes stay the same, there is a relative increase in the ice-phase processes (deposition and sublimation) compared to their liquid phase equivalents (condensation and rain evaporation). The negative MID anomaly (Fig. 4.23b) has its largest strength at C1, decreasing slightly to C2, before strongly decreasing from C2 to C3. For this anomaly, the relative contributions also hardly change from C1-C2, with the main contributor being in-cloud condensation, explaining about 80% of the anomaly strength at C2. There is a slight decrease in below-cloud rain evaporation and snow sublimation and a slight increase in depositional growth of ice and snow. From C2 to C3 there is a drastic decrease (increase) for condensation (deposition of ice and snow).

**UP** The UP positive anomaly (Fig. 4.24a,c,e) significantly shrinks over time, its strength decreases by more than an order of magnitude from C1 to C3. From C1 to C2 the in-cloud processes remain approximately similar with most contributions from condensation (50%) and deposition (20%). For the below-cloud processes evaporation increases from about 15% to about 30%, whereas the 15% snow sublimation contribution at C1 almost vanishes at C2. From C2 to C3 the in-cloud processes increase their importance relative to the below-cloud processes, mainly due to increases in deposition of ice and snow and snow melting. The UP negative anomaly (Fig. 4.24b,d,f) strength significantly weakens over time. Although it slightly increases size from C1 to C2, this is offset by a decrease in magnitude. From C2 to C3 both size and magnitude drop significantly. Deposition of ice and snow and condensation are the most important contributors at each stage. The relevance of below-cloud processes clearly decreases over time, a possible explanation could be that low-level parcels don't reach up to high altitudes at stage C3.

Summarizing, the low-level anomalies BL and LOW show the strongest and

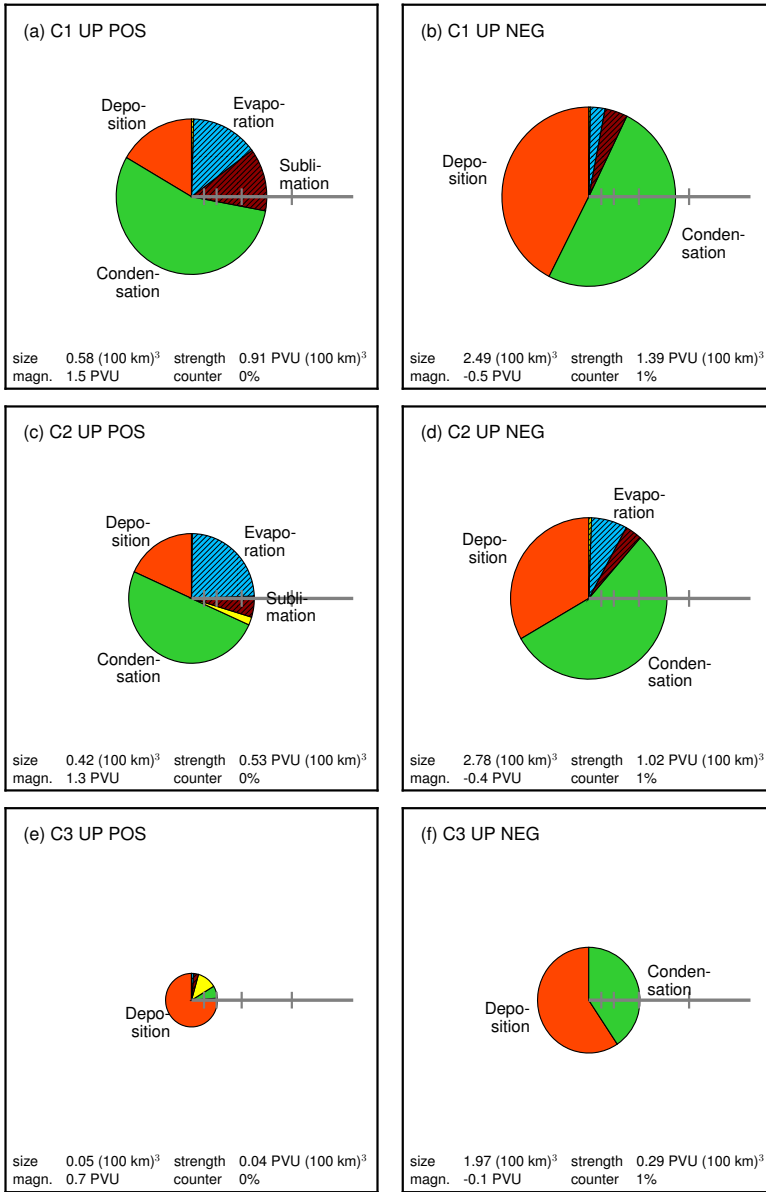


Figure 4.24: As in Fig. 4.23, now showing the time evolution (C1-C3) from top to bottom for the positive (left) and negative (right) anomaly UP.

fastest transition in terms of microphysical contributions (e.g. the positive LOW anomaly changes from condensation, evaporation, ice/snow deposition to snow sublimation, ice/snow deposition, snow sublimation), whereas the Lagrangian contributions to the MID and UP anomalies vary less with time. Below-cloud processes contribute significantly to both positive and negative anomalies over the full life-time of the cyclone and over the full depth of the troposphere. Only for the negative anomalies MID and UP, the importance of below-cloud processes decreases significantly over time. During the transition phase there is an increase in the relative importance of ice phase processes (depositional growth of ice and snow and snow sublimation) compared to liquid phase processes (condensation and rain evaporation). The role of below-cloud rain evaporation is overtaken by its “cold equivalent”, namely below-cloud snow sublimation. It becomes the dominant contributor to the positive LOW anomaly (40%) and also significantly contributes to the positive MID anomaly (25%). Remarkable is the sudden increase from C1 to C2 of contributions from snow melting to the BL (from 15 to 50%) and LOW (from <3% to 15%) positive anomalies.

#### 4.5.3 *How different is the Lagrangian perspective from the Eulerian perspective?*

The relevance of the Lagrangian perspective for understanding the formation of mesoscale PV structures along the fronts has been shown in sections 4.4.1 and 4.4.2. In this subsection, two complementary analyses are presented. First, a comparison is made between CDPV and the cloud diabatic PV rates. The aim is to (a) compare instantaneous rates ( $PVU h^{-1}$ ) with the integrated CDPV values ( $PVU$ ) and (b) to gain a more detailed view of the vertical structure of the PV tower and its changes over time. Then, specific timescales are defined and calculated for the different anomalies over time. This also reveals more insight in the importance of the Lagrangian perspective.

##### Vertical structure of the PV tower

For each microphysical process profiles of horizontally averaged CDPV and instantaneous CDPV rates are calculated and the results are presented in Fig. 4.25. Before describing in detail the different profiles, it is noted that in general, for each microphysical process, its vertical profile of CDPV is quite different from the instantaneous rate of the same process. CDPV provides a time-integrated perspective, where vertical transport, but also horizontal advection are highly relevant.

At stage C1 condensation dominates instantaneous PV changes (Fig. 4.25b), with a maximum exceeding  $0.2 \text{ PVU h}^{-1}$  close to the surface. Above about 1 km height the rates turn negative, however CDPV values are positive up to a height of 3 km (Fig. 4.25a). It becomes evident that vertical transport redistributes the diabatically produced PV. For depositional growth of ice and snow, the maximal production regions lie at around 500 m (probably in the cold sector) and around 4 km height (probably in the warm sector), with maximal destruction just above, at around 6 km height. In terms of CDPV, this process has its main maximum

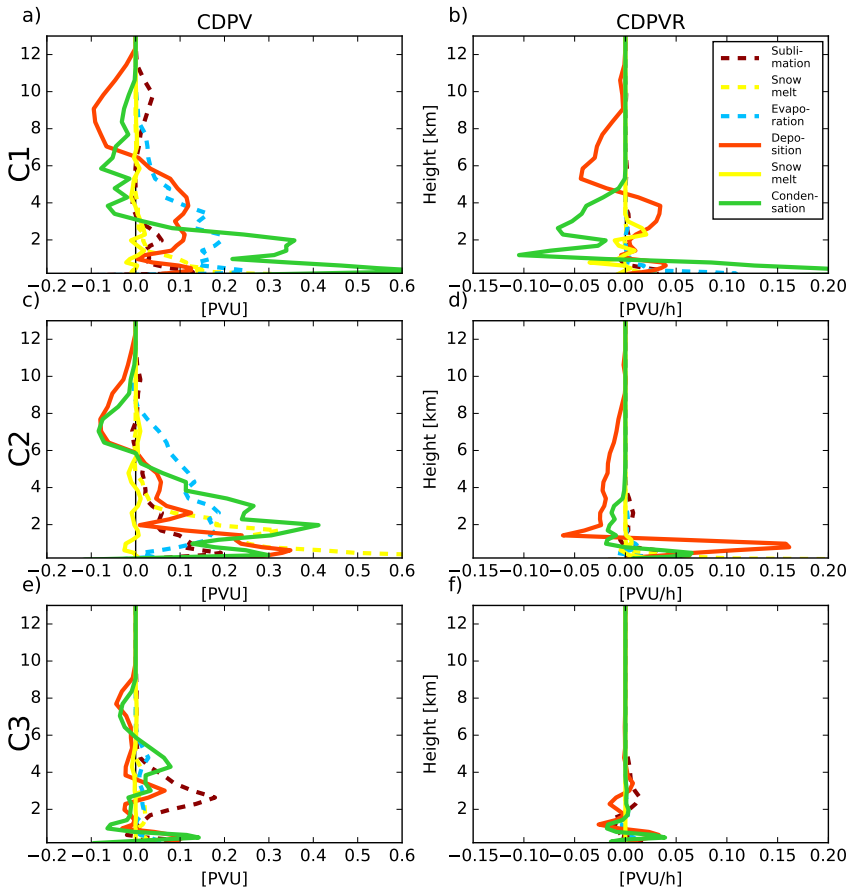


Figure 4.25: Vertical profiles of horizontally averaged CDPV (a,c,e) and CDPV rates (b,d,f) for the different process categories at stages C1 (a,b), C2 (c,d) and C3 (e,f). Horizontal averages are calculated over the cyclone boxes shown in Fig.4.5c for C1, Fig.4.5e for C2 and Fig.4.5g for C3.

between 1-7 km, with a minimum above, between 7-12 km, where again negative CDPV values reach further upwards compared to instantaneous CDPV rates. Snow melting shows an alternating behaviour with both positive and negative rates in between 0 and 3 km, which can probably be explained by the small vertical extent of the melting layer and its variable height in the warm and cold sectors. In terms of CDPV, snow melting contributes mainly between 0-1 km height. Rain evaporation leads to strong diabatic PV production close to the surface, however, it influences the PV far up into the troposphere, as can be seen by the positive CDPV contributions up to a height of 8 km. Apparently parcels influenced by below-cloud rain evaporation make it all the way up into the cloud, a sign of strong vertical transport probably related to the warm conveyor belt. Snow sublimation is characterized by very low CDPV rates, peaking at the surface, but contributions to CDPV are significant, with maxima close to the surface, at 2 km height and at 9 km height.

Comparing the overall change of CDPV rates and CDPV from C1 to C2, different aspects can be noted. It is observed that instantaneous CDPV rates generally decrease, except for depositional growth of ice and snow that approximately keeps its strength; but its dipole structure lowers from around 5 km to about 1 km height. In terms of CDPV, the processes keep their strength. In-cloud condensation and below-cloud snow melting and rain evaporation move a bit upward within the PV tower compared to C1. As an example consider in-cloud condensation: the CDPV maximum close to the surface is less strong at C2 compared to C1, however in the range 3-6 km the contributions changed from negative to positive. Although at this time (C2), the CDPV rates due to condensation (see Fig. 4.25d) are slightly negative in parts of this region. This observation again stresses the importance of the redistribution of PV that was diabatically produced in the time between C1 and C2.

From C2 to C3, the instantaneous CDPV rates for most processes decrease significantly, with the exception of below-cloud snow sublimation. This process slightly increases its magnitude from C2 to C3, though still being weak with a production maximum at about 3 km height of less than  $0.02 \text{ PVU h}^{-1}$ . However, through acting over time, the process is apparently able to produce significant CDPV contributions (about 0.2 PVU), between 2 and 4 km height. For the other processes, CDPV contributions weaken significantly. Interestingly, condensation and rain evaporation have now shifted their maxima upwards, from about 2-3 km at C2, to about 4-5 km at C3. This goes along with a strong decrease in CDPV values at the lower levels. The production regions for both these processes

are at low levels, it makes sense that as soon as production stops, the CDPV anomaly loosens its strength first at low levels. Note that in general, the CDPV modifications at C3 reach only to an altitude of about 9 km compared to 12 km at stages C1 and C2.

In summary, it is noted that (a) during the diabatically active stages C1 and C2, for each process the maximum in CDPV is located at a higher level than the maximum in its instantaneous rate, highlighting the role of vertical transport; (b) at stage C2 there is hardly any production of PV due to rain evaporation, however parcels up to a height of 8 km have been modified by this process, apparently at an earlier moment in time; and (c) at stage C3, there is a strong peak in CDPV due to snow sublimation, even though CDPV rates are small. Apparently, accumulation of PV over time is important. All of these findings underline the importance of the Lagrangian perspective.

### Timescales

In Chapter 3 it was shown that the CDPV anomalies developing in an idealized cyclone were characterized by different timescales. Through calculating the mean CDPV rates of the trajectories ending in the anomaly it was shown e.g. that POS\_NORTH is produced over a longer timescale when compared to POS\_SOUTH. Here, a new approach is introduced. Instead of visualizing the evolution of the diabatic PV rates for each anomaly, we calculate different timescales that tell us how fast ( $\tau_{gain}$  and  $\tau_{active}$ ) and how long back in time ( $\tau_{back}$ ), the PV of a certain parcel was produced.

**Calculation of the timescales** The timescales are calculated for every single trajectory ending within a certain anomaly for stages C1 and C2. It was decided to leave out C3 since most of the high PV air present was not diabatically produced in the preceding 24 hours, therefore the timescales at this stage are not meaningful. Each timescale is calculated for every gridpoint, where every gridpoint corresponds to one backward trajectory. Figure 4.26 shows schematically, for a single trajectory, the meaning of each timescale. First, we define  $\tau_{gain}$  as the time it took a parcel to gain (or loose, in the case that the CDPV is negative) at least half of its CDPV value, independent when the parcel underwent this PV change. It is calculated through sorting the CDPV rates for each trajectory (in reverse order for a negative CDPV value) and integrating them. The first timestep at which the integrated value along the sorted CDPV rates is larger than half the total CDPV is defined as  $\tau_{gain}$ .

Another timescale  $\tau_{back}$  is introduced to indicate how far back in time a certain

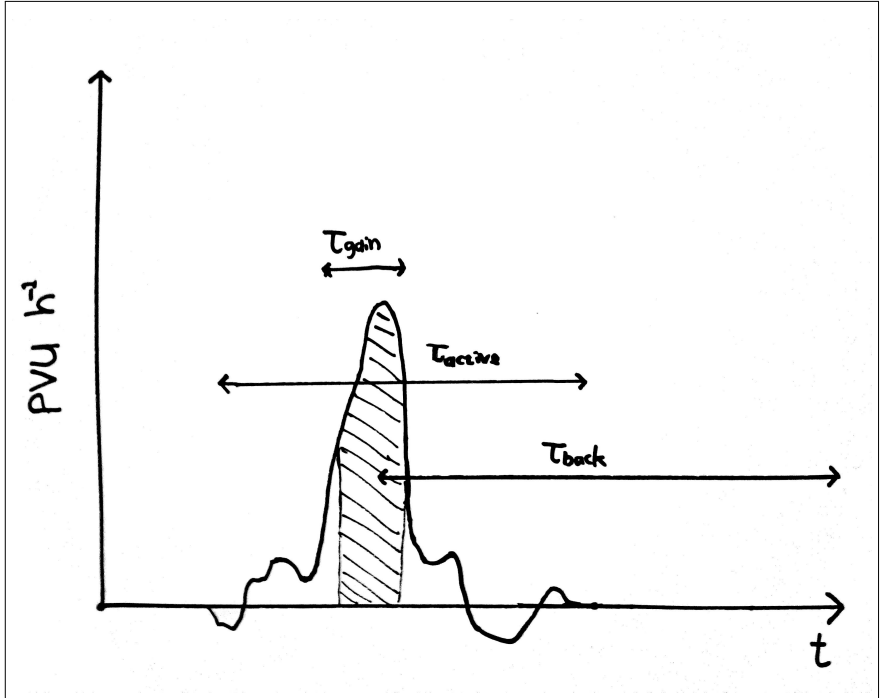


Figure 4.26: Schematic illustrating the three different timescales for a single trajectory:  $\tau_{gain}$  represents the time it took a parcel to gain half of its current CDPV value (the shaded area);  $\tau_{back}$  is the mean time (backwards) the CDPV of a parcel was produced, and  $\tau_{active}$  represents the total time a parcel has experienced cloud diabatic PV changes.

parcel gained or lost most of its CDPV. It is calculated as the CDPV rate-weighted time mean along the backward trajectory. If a parcel experienced a constant CDPV rate from 12 to 8 hours before arriving at the gridpoint location, this would result in a  $\tau_{back}$  value of 10 hours.

Finally, the timescale  $\tau_{active}$  simply defines how long a certain parcel experienced non-zero CDPV rates.

As a value representative for the whole anomaly, the trimean is calculated:

$$trimean = \frac{p_{25} + 2 \cdot p_{50} + p_{75}}{4} \quad (4.4)$$

where  $p_y$  denotes the  $y$ -th percentile over all trajectories ending in the anomaly. This statistical metric is chosen since it is a more robust measure compared to the mean.

	$\tau_{gain}$		$\tau_{back}$		$\tau_{active}$	
	C1	C2	C1	C2	C1	C2
BL	0.5	0.6	4.5	5.9	10.5	11.1
LOW	0.3	0.3	5.7	6.4	10.3	11.8
MID	0.1	0.1	7.9	9.4	10.8	11.2
UP	0.1	0.1	10.2	14.8	9.6	10.8

Table 4.2: Trimean values of the three different timescales  $\tau_{gain}$ ,  $\tau_{back}$  and  $\tau_{active}$  (in hours) for the positive anomalies (rows) for the stages C1 and C2 of the cyclone (columns).

**Timescales for the different anomalies** As can be seen in Table 4.2, the values of  $\tau_{gain}$  are typically very short with 0.1-0.6 h. However, the parcels are diabatically active over a much longer period with  $\tau_{active}$  ranging from about 9-11 h. In general  $\tau_{gain}$  slightly increases over time, which is consistent with the decreasing heating rates over time.

The time  $\tau_{back}$  when parcels typically gained their PV shows a larger range from about 5 to 15 h. It becomes clear that the anomalies at higher levels were generated longer back in time compared to anomalies at lower levels. From C1 to C2, there is an increase in  $\tau_{back}$  for all the anomalies, which is consistent with the fact that the diabatic heating rates decrease over this time (see Fig. 4.4), i.e., the advection of remotely produced CDPV becomes more important compared to local production.

The time parcels have been cloud diabatically active shows the smallest variation both over time and over height.

Summarizing, for all positive anomalies at C2, parcels gain their PV less quickly, longer back in time and they have been longer diabatically active compared to C1. In addition, positive anomalies located at upper-levels gained their PV in very short time intervals, generally longer back in time compared to low-level anomalies and have been diabatically active for a shorter time period.

## 4.6 Comparison to the idealized cyclone

In this section the results presented for the frontal wave stage (C1) will be compared to the idealized case in Chapter 3. First we note a few differences between our idealized cyclone, and the real cyclone. At the time of analysis for the ideal case ( $t=36$  h, see Fig. 3.3d), the idealized cyclone had a core pressure of about 960 hPa, whereas the real cyclone at the frontal wave stage (C1) had



a core pressure of about 945 hPa. Also the pressure drop during the preceding 24 hours is with 35 hPa for the real case larger compared to the about 28 hPa for the idealized cyclone. In terms of development stage, the idealized cyclone has developed slightly further when compared to the real cyclone, with the formation of a bent-back front, whereas the real cyclone is in its frontal wave stage. Whereas clouds and precipitation are fully developed along the cold front in the real case (see Fig. 4.10b), no clouds and precipitation can be found along the cold front in the idealized cyclone.

Keeping in mind the differences in frontal structure and cyclone intensity, the findings of the real case as presented in the previous section, will be compared to the idealized case that was studied in Chapter 3.

#### 4.6.1 *Warm front structure*

Comparing Figs. 4.8b and 3.6b shows that the structure of clouds and precipitation is similar between the real and idealized cases. For both cases, the melting layer is at about 2 km height in the warm sector, and close to the surface in the cold sector. However, there are remarkable differences in terms of the width of the front. Whereas in the idealized case, the melting layer slopes over about 100 km, in the real case this is only 50 km. Also, in the idealized case, the sloping of the melting layer continues further to the north of the surface warm front, whereas in the real case, there is an abrupt change in melting layer height from about 1 km height towards the surface.

In terms of the in-cloud diabatic PV contributions (Figs. 4.8c and 3.6c), common characteristics are the upper-level negative PV anomaly of about 1 km vertical extent related to depositional growth of ice and snow. Also in both cross-sections, below those negative contributions, a wide region with positive contributions from depositional growth of ice and snow can be found. In the real case, this region reaches almost down to the surface, whereas in the idealized case the positive contributions only reach down to a bit below 2 km. For the positive contributions due to condensation, there is a remarkable difference. In the real case, they reach up to heights of about 5 km, compared to only about 2 km in the idealized case. On the other hand, in-cloud snow melting, reaching up to about 5 km in the real case, also reaches high, to about 4 km in the idealized case.

For the below-cloud diabatic PV contributions (Figs. 4.8d and 3.6d), a common feature is the occurrence of a negative anomaly due to snow sublimation on the cold side of the front. Also, in both cases, below-cloud snow melting contributes in a narrow (~30 km) region from the surface upwards crossing the

melting layer. In both the real and idealized case, below-cloud rain evaporation contributes positively. However, as for the in-cloud process of condensation, rain evaporation contributes much higher up in the cloud, up to altitudes of about 6 km for the real case, compared to only about 2.5 km in the idealized case.

#### 4.6.2 *CDPV anomalies*

For the anomaly selection, a different approach was taken in the real case, compared to the idealized case. Whereas in the idealized case, anomalies were selected based on three-dimensionally connected regions with  $|CDPV| > 0.2 PVU$ , in the real case, the regions were defined manually, and within each region only the grid points having  $|CDPV| > 0.2 PVU$  were selected, independent whether or not they were connected to each other. Nevertheless, a comparison will be made, keeping in mind that in the real case, there is also diabatically produced PV in the warm and cold sectors that is not linked to the fronts, whereas in the idealized case all the cloud diabatic PV was located in the wider frontal region (see Fig. 3.7).

##### Positive anomalies

The anomalies on the warm side of the front (real BL\_WARM and LOW\_WARM and idealized POS\_SOUTH in Fig. 3.7) both owe about two-third of their strengths to in-cloud condensation and about one-third to below-cloud rain evaporation. It is remarkable, that the relative strength of the processes is so similar, even though the total magnitude of the real case anomaly (3.2 PVU) is almost twice as large as in the idealized case.

On the cold side of the front, the real anomalies BL\_COLD and LOW\_COLD are compared to the idealized anomaly POS\_NORTH. Whereas the latter was formed mainly due to below-cloud snow melting and evaporation, its real case companions have only one third of their strength explained by these processes, with further contributions from below-cloud snow sublimation and in-cloud condensation and depositional growth of ice and snow.

At mid levels, the idealized anomaly POS\_WEAK is compared to the real anomaly MID\_POS. In the ideal case, this anomaly has only net positive contributions from depositional growth of ice and snow, whereas in the real case also condensation and below-cloud rain evaporation contribute significantly. Again, it becomes evident, that in the real case, both condensation and below-cloud rain evaporation

impact the PV up to higher levels into the cloud compared to the idealized case.

### Negative anomalies

The upper-level negative anomalies (real UP and idealized NEG\_UPPER) show a more remarkable difference. The ideal anomaly is purely due to depositional growth of ice and snow, whereas in the real case, condensation contributes as much as depositional growth of ice and snow.

The idealized anomaly NEG\_MID, located in the middle between the two low-level positive anomalies, is purely related to snow melting. As discussed in the previous section, no clear negative anomaly can be identified in the section across the warm front in the real case. However, both the negative anomalies BL\_WARM and LOW\_WARM show small contributions of snow melting, explaining roughly 1/8th of their strength.

In the idealized case, a negative anomaly related to snow sublimation (NEG\_NORTH) was found on the cold side of the front. Also for the real case negative anomalies BL\_COLD, and to a lesser extent LOW\_WARM, contributions from snow sublimation can be found.

#### 4.6.3 *A conceptual understanding of the complex frontal mesoscale PV patterns*

The mesoscale PV structure along the fronts is shaped by a complex combination of different microphysical processes. Here, a conceptual framework will be presented to explain the complicated patterns of microphysical contributions as presented in the frontal cross sections. This might also help understanding the differences in the complex mesoscale PV structures as seen across the bent-back front in the idealized case (Chapter 3) compared to the warm front in the real case (Chapter 4).

The concept is based on the knowledge that a heating (cooling) maximum leads to a dipole of PV modification with production below (above) and destruction above (below). This PV modification dipole is schematically illustrated in Fig. 4.27c. Now, consider a cooling process having its maximum at the surface, e.g. rain evaporation. This leads to a monopole of PV production (Fig. 4.27a). Now consider the impact of the flow transporting this structure and modifying its shape. This can transport the impact of a certain process upwards into the cloud, as illustrated in Fig. 4.27b. For the dipole structure (Fig. 4.27c) a similar

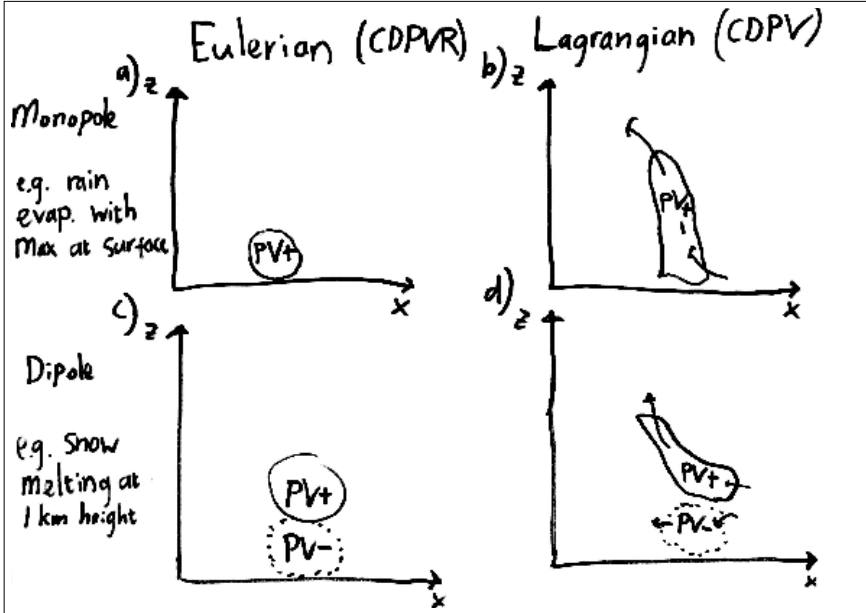


Figure 4.27: Schematic illustration of the concept of flow-modified PV dipoles. (a) DPVR monopole in Eulerian perspective, (b) a potential Lagrangian CDPV pattern belonging to this monopole, (c) DPVR dipole in Eulerian perspective, (d) a potential Lagrangian CDPV pattern belonging to this dipole.

pattern can evolve, but note that there can be differential transport, bringing e.g. the positive part of the dipole up into the cloud, whereas the negative part of the anomaly stays at low levels. Note that the hypothetical CDPV structure in Fig. 4.27d looks similar to the contribution of in-cloud snow melting to the CDPV in Fig. 3.6c. It could even be hypothesized that the strong cooling itself modifies the flow pattern in such a way to act as a positive feedback of the separation of the two parts of the dipole from each other.

The mesoscale PV structure for each microphysical process, arises from a complex combination of (a) the Eulerian location of the pole belonging to this process relative to the front (Fig. 4.27a,c), and (b) the transport into the cross-section which also modifies the pole (Fig. 4.27b,d). Neither of these were investigated in detail. Though, with regard to (a) it can be noted that the melting layer slopes more steeply in the real case as compared to the idealized case. This could bring the PV monopole (cooling maximum at the surface) of snow melting closer to the positive part of the condensation dipole and the rain evaporation monopole (cooling maximum at the surface). Thereby condensation, rain evaporation

and snow melting all contribute to the same very strong low-level positive PV anomaly in the real case. In contrast, in the idealized case, a low-level split PV structure was found. Similarly, the cold front in the real case is very sharp, it is therefore not surprising that the strong low-level positive PV anomaly consists of basically all processes together.

Summarizing, in both the idealized and real case we find:

- Strong contributions of the below-cloud processes snow melting and rain evaporation to the positive anomaly as a whole
- For the in-cloud contributions to the positive anomaly, condensation dominates in the lower part and depositional growth of ice and snow in the upper part
- A small negative anomaly on the cold side of the front related to below-cloud snow sublimation
- A negative upper-level anomaly with an extent of  $\sim 1$  km due to depositional growth of ice and snow
- Below-cloud contributions reaching way up into the cloud, emphasizing the importance of a Lagrangian perspective for understanding PV structures in extratropical cyclones

Despite these common characteristics, there are notable differences. First, as mentioned before, the total CDPV in the idealized case is much more spotty compared to the real case, i.e. there are alternating positive and negative contributions separated by only a few tens of kilometers in the vertical or horizontal direction.

Further, the below-cloud processes (mainly rain evaporation) reach to much higher altitudes in the real case when compared to the idealized case. This points to a stronger vertical transport in the real case cyclone, which is not surprising given that this cyclone is stronger than the idealized cyclone. In addition, the presence of surface friction (absent in the idealized case) could lead to increased vertical motion upward from the boundary layer due to Ekman pumping in the real case.

Another remarkable difference between the real case and idealized case is that for the idealized case, the low-level positive anomaly as a whole, was split into two distinct regions with elevated PV values and CDPV contributions. Each of these regions had its own characteristic microphysical contributions. In the real case, no clear split PV structure is apparent at low levels, and also the

CDPV contributions show much more overlap. A possible explanation for this difference, could be the difference in low-level frontal structure.

## 4.7 Summary

The main aim of this chapter was to find out how important below-cloud processes are for the mesoscale PV and its structure in a real case cyclone. It was shown that below-cloud processes are relevant throughout the lifecycle of the cyclone, contributing about one third of the strength of the low-level positive PV anomalies, similar to what was found in the idealized case study. The mesoscale PV structure is different from the idealized case, something that can possibly be explained by the difference in frontal structure. It was found that vertical transport plays an essential role in the redistribution of diabatically produced PV highlighting the importance of the Lagrangian perspective.

# 5

## SUMMARY

---

Through applying a novel Lagrangian method to construct cloud diabatic PV budgets, we investigated the impact of microphysical processes on the mesoscale PV structure in an idealized and real case extratropical cyclone. The main findings can be summarized by answering the key questions as posed in the introduction.

### 5.1 How important are below-cloud processes like rain evaporation, snow melting and snow sublimation for the positive and negative PV anomalies?

It was found that below-cloud processes contribute strongly to both positive and negative PV anomalies. In the idealized case, at the warm side of the front, *rain evaporation* contributed  $\sim 0.3$  PVU to an anomaly of  $\sim 1.0$  PVU, in the real case, a much stronger cyclone, this process even contributed  $\sim 1.0$  PVU to a total anomaly of  $\sim 3$  PVU.

Later in the development of the real case cyclone, the role of rain evaporation in enhancing the low-level (0-2 km) positive PV anomalies is taken by *snow sublimation*, contributing about 0.4 PVU. The total strength of the low-level positive CDPV anomalies decreases over time, and the relative importance of below-cloud processes compared to in-cloud processes increases slightly. Whereas snow sublimation is important for the positive low-level CDPV anomalies at the later stage, earlier, this process leads to the formation of negative anomalies in the cold sector at low and mid levels. In both the idealized and real case, the contributions are about -0.3 PVU.

Snow melting behaves differently from rain evaporation and snow sublimation, its contributions are much more local, but therefore often stronger. In both the idealized and the real studies, snow melting contributed strongly in the region where the melting layer hits the surface.

Through vertical transport, the impact of the below-cloud processes is transported upwards into the cloud, up to 8 km height in the case of rain evaporation in the strong real case cyclone.

## 5.2 Can the mesoscale PV structure at the fronts be explained by the microphysical processes?

For an idealized cyclone, it was found that the different microphysical processes dictate the strength and shape of the PV anomalies. Whereas the positive anomalies were characterized by contributions from many different processes, the negative anomalies were each characterized by a distinct process: depositional growth of cloud ice and snow for the large upper-level negative anomaly, and snow melting and snow sublimation each producing a distinct negative anomaly. For the real case study, the picture looks slightly different. First, it was found that cloud diabatic processes were dominating over convection and radiation, noting that locally they can be important. In terms of the cloud diabatic PV, it was found that there is more overlap for the different microphysical contributions. The positive anomaly along the warm front exists due to several in-cloud and below-cloud processes: condensation and below-cloud rain evaporation are most important in the lower part, whereas deposition of ice and snow is most important in the upper-part. Snow melting contributes very strong, but also very localized at the surface front. It is believed that the thermal structure in these two sections, are two samples from a wider spectrum of fronts. How representative they are is subject of further research.

## 5.3 What is the general evolution of the positive and negative anomalies over time?

It was shown that, as the cyclone occludes and generally becomes embedded in a colder environment, the relative importance of ice phase processes (depositional growth of ice and snow and snow sublimation) compared to liquid phase processes (condensation and rain evaporation) increases significantly. The strongest microphysical transitions occur at the low-levels. This can be related to (a) the fact that temperature changes mainly at low levels and (b) the fact that CDPV at mid and upper-levels was generally produced at lower levels back in time. Therefore, the mid and upper-levels respond more slowly to the temperature changes. The positive anomaly varies most, whereas the negative anomaly strength remains fairly constant. Most anomalies reach their largest strength at time C2, even though diabatic heating has dropped already with almost 40% compared to C1. Positive anomalies only reach up to high levels in the early stages.



#### 5.4 Do we require the Lagrangian perspective to answer the above questions?

It becomes evident that the PV pattern is not a simple result of the instantaneous production or destruction of PV. Rather, the effects of rain evaporation that occurred below the clouds, can be transported all the way up to 8 km altitude into the clouds. For the real case, it was shown that the northern strong positive CDPV anomaly was produced over a longer time compared to the southern positive anomaly. Furthermore, the timescales calculated for the different anomalies in the idealized case, revealed that, typically a parcels PV has been produced due to cloud diabatic processes occurring about 5-10 hours earlier. Contrasting to this, the timescales in which the PV was produced are very short with typically  $<1$  h, which indicates that locally, in the production regions, the Eulerian perspective does not differ much from the Lagrangian perspective. However, the role of both horizontal and vertical transport in redistributing the cloud diabatically produced PV is essential. In addition, it was shown how the importance of remotely diabatically produced PV increases over time for the real cyclone, as the diabatic processes diminish.



# 6

## FINAL REMARKS & OUTLOOK

---

### 6.1 Final remarks

In this study two particular cyclones were investigated, one idealized cyclone for which the bent-back front was studied, and a strong maritime cyclone for which both the warm front and the cold front were studied. Probably these two cyclones are a sample from a wide spectrum in terms of their mesoscale structure and the role of the microphysical processes.

For both case studies, the COSMO model was used. This model is ran operationally at several national weather services (e.g. DWD, MeteoSwiss) across Europe, and is therefore well tested. However, other models have different parameterizations for the microphysics, because the details of the formation and dissipation of clouds and precipitation are not exactly known and therefore not represented correctly in the models. In this study it has been shown that the detail in microphysics can matter for the mesoscale PV pattern and thus the dynamics. A different representation of these processes in the model can lead to differences in the simulated frontal structures and associated weather.

In this study we defined Lagrangian anomalies, through integrating diabatic PV modification along the flow. Whereas for Eulerian anomalies one needs to define a reference state, for Lagrangian anomalies we need to define an integration time. For our idealized setup this was straightforward, since we were interested in the effects of microphysical processes on the PV, we simply integrated back in time to the point at which no clouds were present yet in the vicinity of the cyclone studied, which led to an integration time of 36 h. However, the real atmosphere is never at rest and clouds and precipitation are around all the time, therefore in the real case cyclone the choice of this integration time was more arbitrary. A time of 24 h was chosen, and seemed to be justified by the fact that the strongest cloud diabatic PV changes took place well within this time frame and were therefore included in the budget. Since several studies use the concept of Eulerian anomalies (e.g. Davis and Emanuel, 1991), in Appendix A the Lagrangian and Eulerian anomalies are compared for both the idealized and real case studies. One of the outcomes is that at upper-levels the two anomalies differ quite strongly, and it will be argued that along-flow integrated latent heating

explains a crucial part of this difference.

## 6.2 Outlook

It would be interesting to investigate the validity of the results in a more climatological sense. The conceptual framework explained in section 4.6.3 might help in understanding case-to-case variability.

Besides expanding the results to a more climatological perspective, it would be of interest to study more in detail the impact of the different anomalies on (a) each other, (b) the upper-level wave guide and (c) the surface circulation. Of importance here is the partitioning of the PV anomaly into a temperature field and wind field anomaly. It can be shown that whereas lens-shaped anomalies are characterized more by temperature anomalies, anomalies with a larger vertical extent establish themselves more as rotational flow anomalies (Hoskins et al., 1985). To quantify this partitioning, and the different impacts as mentioned above, a piecewise PV inversion (Davis and Emanuel, 1991) could be performed on the different anomalies.

With our framework it is possible to identify regions within a cyclone that are sensitive to certain microphysical parametrizations, this can guide targeted measurements in terms of the microphysical process to focus on as well as the location within a cyclone to perform the measurements.

Furthermore, our newly developed method of integrating diabatic PV rates along backward trajectories is widely applicable. As an example, in Appendix B it is shown how our method can be used to quantify the different diabatic processes involved in stratosphere troposphere exchange.

# A

## ON THE ROLE OF CROSS-ISENTROPIC TRANSPORT FOR THE PV ANOMALIES

---

The main aim of this thesis was to *quantify* the impact of different microphysical processes on the PV structure in extra-tropical cyclones. This has been done through calculating Lagrangian PV anomalies, which is different from the conventional way of defining a PV anomaly as a Eulerian anomaly. The aim of this section is to describe and understand the differences between the two approaches. The formation of the upper-level negative PV anomaly in the outflow region of a strongly ascending airstream (warm conveyor belt) is a complex process involving dry isentropic advection, and moist processes contributing in two ways. First, cloud diabatic PV modification through an overlap of heating rate gradients and vorticity along the air flow contribute to the anomaly. This effect can be quantified by studying the evolution of the diabatic PV rates along the trajectories (Joos and Wernli, 2012) or by constructing a Lagrangian PV budget as was done in this thesis. The strength of the Lagrangian upper-level negative PV anomaly was found to be about -0.5 PVU in both the idealized (NEG\_UP in Fig. 3.7 with  $t_{int} = 36 h$ ) and real studies (the negative anomaly UP in Fig. 4.12 with  $t_{int} = 24 h$ ). The second way in which moist processes can contribute to the formation of PV anomalies is through cross-isentropic transport of lower tropospheric low-PV air. This mechanism was recognized already by Rossby (1937). However, later studies (e.g. Persson, 1995; Wernli and Davies, 1997; Madonna et al., 2014; Methven, 2015) generally didn't distinguish between the two pathways in which diabatic heating contributes to upper-level negative PV anomalies. An exception is Pomroy and Thorpe (2000) who recognized the importance of this distinction. They calculated the anomalies by selecting regions in which the backward trajectories experienced heating, and for these regions they calculated  $PV_{Lag}^*$  (Eq. 2.14). When referring to their Fig. 4a, which shows the PV field with the selected anomaly subtracted, they noted that: "the apparently anomalous region is not entirely absent [...] This shows that advection from well within the troposphere also accounts for some of the low PV." Although they performed a very detailed analysis of the different Lagrangian-type anomalies, they did not further analyse the contributions from this process. Combining Eulerian and Lagrangian analyses, the plotting of warm conveyor belt trajectory intersection points with isentropic

surfaces by Grams et al. (2011) illustrates the occurrence of cross-isentropic mass transport.

Although both of the above studies nicely illustrate the occurrence of the effect, quantifying the amount of cross-isentropic low PV transport is not straightforward. The fact that the two different mechanisms (along-flow diabatic PV modification and cross-isentropic low-PV transport) are inherently linked, makes it difficult to distinguish the two. Both Madonna et al. (2014) and Methven (2015) show that along the warm conveyor belt, generally  $PV_{Lag}^* \approx 0$  and therefore the negative Eulerian PV anomalies quantified in Madonna et al. (2014) are probably due to cross-isentropic transport, considering that these parcels are heated considerably (typically  $> 20$  K) during their ascent. However, as far as we are aware of, no earlier study has been able to quantify this cross-isentropic transport of low PV air.

Here, some light will be shed on the problem, through comparing Lagrangian and Eulerian anomalies and showing how differences between the two arise in strongly heated air masses.

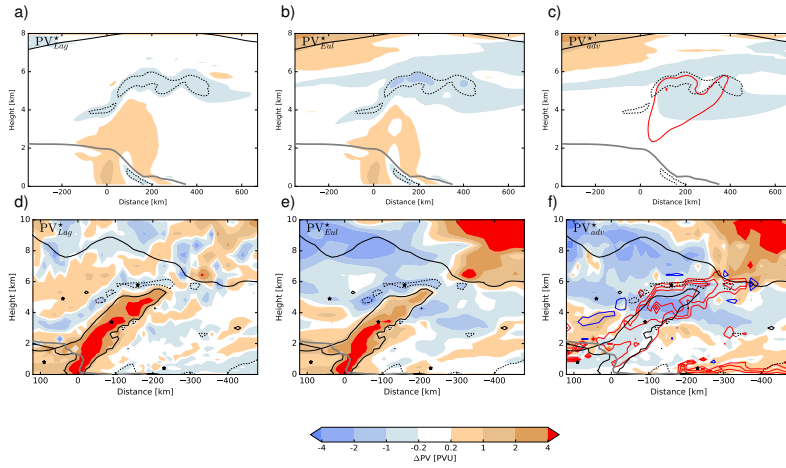


Figure A.1: Sections through (a,b,c) the idealized bent-back front (Fig. 3.3d) and (d,e,f) the real case warm front (Fig. 4.7a) showing the different types of PV anomalies (units PUV) in colour shading: (a,d) the Lagrangian anomaly  $PV_{Lagr}^*$ , (b,e) the Eulerian anomaly  $PV_{Eul}^*$  and (c,f) the advective anomaly  $PV_{adv}^*$ . Every panel shows the 2 PUV (solid) and 0 PUV (dashed) contours in black and the melting layer as a grey line. Red (blue) contours show total diabatic heating (cooling) at 5 K intervals.

**Comparing the Eulerian and Lagrangian PV anomalies** For calculating an Eulerian PV anomaly, a reference PV field needs to be defined. Depending on the focus of the study this reference is taken to be the PV at a certain reference time, a mean PV over a certain time-span or a climatological mean PV field. Our aim was to compare the Lagrangian anomalies building during  $t_{int}$ , therefore, we took as a reference state the timestep  $t_{int}$  before the time of interest. This resulted in  $t_{int} = 36 h$  for the idealized cyclone in Chapter 3 and  $t_{int} = 24 h$  for the real cyclone in Chapter 4. Thus, the Eulerian PV anomaly is calculated as follows:

$$PV_{Eul}^* = PV - PV_{ref} \quad (A.1)$$

The Lagrangian anomaly, through writing Eq. 2.14 a bit differently, is given by:

$$PV_{Lag}^* = PV - PV_{ini} \quad (A.2)$$

where  $PV_{ini}$  is the PV at the starting point of the backward trajectories calculated  $t_{int}$  back in time. The difference between the Eulerian and Lagrangian anomaly ( $PV_{Eul}^* - PV_{Lag}^*$ ) is given by:

$$PV_{adv}^* = PV_{ini} - PV_{ref} \quad (A.3)$$

Where  $PV_{ini}$  is the initial PV of the backward trajectories advected passively to their arrival points and  $PV_{ref}$  is the model PV at this arrival point at the reference time. In other words,  $PV_{adv}^*$  represents the anomaly purely due to advection of reference state PV. Now, we compare the Lagrangian and Eulerian anomalies. At low levels (0-3 km) the Lagrangian anomalies (Fig. A.1a,d) are almost identical to the Eulerian anomalies (Fig. A.1b,e) which means that the along-flow PV modification dominates over the advection of reference state PV gradients. In the mid-levels (3-6 km) there are slight differences between the ideal case Lagrangian and Eulerian anomaly (Fig. A.1a,b). The positive parts of  $PV_{Lag}^*$  are stronger than  $PV_{Eul}^*$  and the negative parts of  $PV_{Lag}^*$  weaker. For the real case, the differences are even larger (Fig. A.1d,e) with regions where  $PV_{Lag}^* = 4$  PVU, have only  $PV_{Eul}^* = 2$  PVU. The largest differences between  $PV_{Lag}^*$  and  $PV_{Eul}^*$  can be found at upper levels. In these regions the anomalies are caused by advection (Fig. A.1c,f). This is not surprising, since the reference state isentropic PV gradients are large here, and there is strong advection in a developing cyclone. In the next subsection, it will be argued that a consideration of the total diabatic heating along the trajectories is key to understanding the differences in the mid-troposphere.

**Diabatic heating and cross-isentropic low-PV transport** When there are PV gradients present in the basic state fields, anomalies can develop through advective



tion. In a dry atmosphere, the advection will be isentropic, and one needs to consider the PV gradients on isentropic surfaces and their advection to understand the formation of Eulerian PV anomalies. In a moist atmosphere, latent heating leads to cross-isentropic mass transport. If this cross-isentropic transport takes place in regions where there are vertical gradients in PV, this also leads to the development of a Eulerian PV anomaly.

This means that we can decompose the Eulerian anomaly into a Lagrangian part and an advective part:

$$PV_{Eul}^* = PV_{Lag}^* + PV_{adv}^* \quad (\text{A.4})$$

Whereas the separation of the Eulerian anomaly into Lagrangian and advective parts is straightforward, disentangling the cross-isentropic and isentropic advection is far from straightforward. The strength of isentropic PV advection is only limited by the presence of isentropic PV gradients (obviously in a developing cyclone, the isentropic advection is strong), whereas the strength of cross-isentropic advection is limited by the latent heating. We can get insight into the cross-isentropic transport by looking at integrated latent heating along the backward trajectories.

Now, we discuss  $PV_{adv}^*$  at mid levels (3-6 km), where diabatic processes are important, and considerable differences between the Lagrangian and Eulerian anomalies were identified.

For the idealized case (Fig. A.1c), within and below the region with negative PV, a weak negative anomaly  $PV_{adv}^* < -0.2$  PVU can be identified, which coincides with a region that has been heated (red contour indicates 5 K). This region has a depth of about 2 km and weakens the Lagrangian positive PV anomaly, but strengthens the Lagrangian negative PV anomaly. The magnitude of the Lagrangian negative anomaly is similar to the magnitude of the advective anomaly with about 0.5 PVU. The Lagrangian anomaly has a limited vertical extent of about 1 km, whereas the advective anomaly has an extent of about 2 km. The strongest negative anomaly of  $PV_{Eul}^*$  (Fig. A.1b), arises due to the combined effect of along-flow PV modification (CDPV) and cross-isentropic low-PV transport.

For the real case (Fig. A.1f), the most negative  $PV_{adv}^*$  ( $< -2$  PVU) also coincides with the strongest latent heating ( $> 15$  K), with both the magnitude of the heating and the magnitude of the advective anomaly much stronger compared to the idealized case. At the same altitude, outside the heated region, also negative anomalies can be found, however, they are weaker with  $PV_{Adv}^* \approx -1$  PVU.

Although we cannot yet quantify the cross-isentropic low PV transport, we have shed some light on the process, by showing the different types of anomalies

and the total latent heating in cross sections. From the results in our idealized and real case simulations, the effect of cross-isentropic transport is to weaken the Lagrangian positive PV anomaly at mid-levels. On the other hand, for the upper-level negative anomaly, cross-isentropic PV transport has the potential to enhance the negative anomaly, explaining why the Eulerian negative anomaly is stronger than the Lagrangian negative anomaly. In the real case, where diabatic heating was much stronger compared to the ideal case, also the advective anomaly was much stronger, even though the Lagrangian anomaly had a similar strength compared to the ideal case. It has to be noted, that a part of these differences can arise from differences in the basic-state isentropic PV gradients between the idealized and real case.

An interesting follow-up study would be to investigate the sensitivity of both the upper-level negative Lagrangian anomaly and the upper-level negative advective anomaly to the total diabatic heating in an idealized setup. Through constructing a basic state with no (or small) isentropic PV gradients at heights between 3-6 km, it would be possible to study solely the cross-isentropic PV transport in this region. A hypothesis could be that the advective anomaly increases its relative importance to the Lagrangian anomaly with increased diabatic heating. Due to its dependence on basic state *vertical* PV gradients it could respond non-linearly to increases in latent heating.

# B

## ANOTHER APPLICATION OF OUR METHOD: STRATOSPHERE-TROPOSPHERE EXCHANGE

---

Stratosphere-troposphere exchange (STE) is important because it impacts the budgets of ozone and water vapour, which influence climate directly through their radiative properties (Gauss et al., 2003) or indirectly through their influence on atmospheric chemistry (Roelofs and Lelieveld, 1997; Kentarchos and Roelofs, 2003). Global climatologies indicate that STE is common in the vicinity of storm tracks (Škerlak et al., 2014). Reutter et al. (2015) constructed cyclone-centered composites to study STE in the vicinity of cyclones. They showed that during cyclone intensification and the mature stage, troposphere-to-stratosphere transport (TST) tends to occur close to the cyclone center, whereas stratosphere-to-troposphere transport (STT) occurs further to the southwest. During the cyclone's decay both STT and TST occur close to the cyclone center, in a region with a low tropopause.

With the novel Lagrangian PV budget construction method, we have the potential to investigate STE in detail for individual cases. It is possible to distinguish between the influence of the large scale cloud scheme, convection and radiation in explaining the STE. Here, we present some preliminary results for the cyclone studied in Chapter 4.

The dynamical tropopause in mid-latitudes can be defined as the 2 PVU isosurface (e.g., Holton et al., 1995). Through changing PV, parcels can cross the tropopause and thereby lead to cross-tropopause mass transport. For TST, a parcel needs to gain PV, whereas for STT a parcel needs to lose PV. For the reader who prefers a more dynamical PV perspective, one can link the occurrence of STE to the strengthening and weakening of troughs and ridges (see also section 7 in Hoskins et al., 1985). TST is associated with the weakening of ridges and the strengthening of troughs, whereas STT is associated with the strengthening of ridges and the weakening of troughs. These relations are summarized in Table B.1.

**Methods** The tropopause level is determined with the method developed by Škerlak et al. (2014). Note that this method prevents the erroneous attribution of low-level diabatically produced PV as belonging to the stratosphere. For details, see Fig. 1 in Škerlak et al. (2014). Backward trajectories are calculated from

	strengthening	weakening
ridge	PV- STT	PV+ TST
trough	PV+ TST	PV- STT

Table B.1: Relation between the strengthening and weakening of troughs and ridges and the occurrence of the two directions of stratosphere-troposphere exchange.

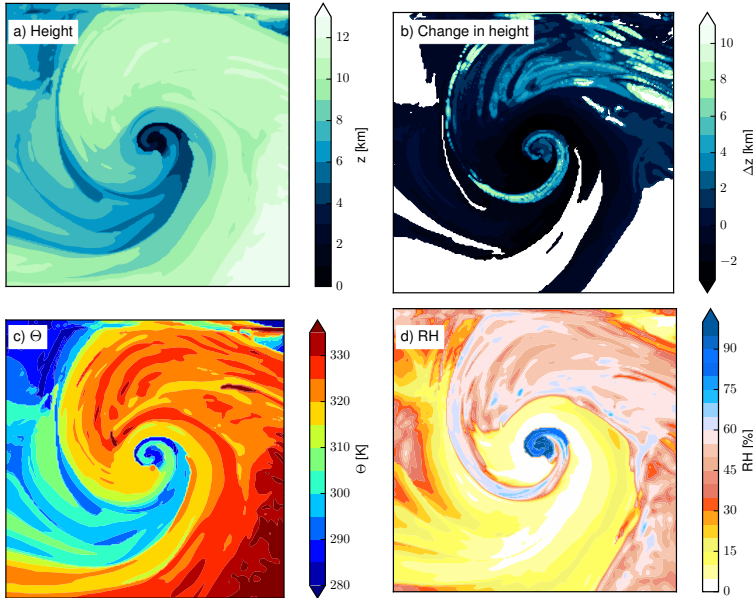


Figure B.1: The tropopause level surrounding the cyclone at 03 UTC 13 December, (a) height (in km), (b) height change (in km), (c) potential temperature (in K), (d) relative humidity (in %). In (b) the regions where the backward trajectory left the lateral boundaries of the model domain have been masked and are coloured white.

the tropopause at 03 UTC 13 December 2015 over 33 hours and a diabatic PV budget is constructed for the large-scale cloud scheme, radiation and convection as described in section 2.3. The starting heights of the trajectories are shown in Fig. B.1a. Note that close to the cyclone center the starting points are low ( $< 4$  km). This is related to diabatically produced PV which exceeds the 2 PVU value, but connects vertically to the stratospheric reservoir of high-PV air.

**Tropopause structure** Figure B.1c shows the potential temperature at the tropopause at 03 UTC 13 December (stage C2 as described in Chapter 4). Low potential temperature indicates a low (Figure B.1a) tropopause (a trough) and high values indicate a high tropopause (a ridge). The trough wraps up cyclonically,

and is therefore characterized as LC2 (Thorncroft et al., 1993).

The relative humidity (RH, shown in Fig. B.1d) is relatively high in the ridge, with values of around 50% in most regions and up to about 80% locally, in regions that also underwent strong ascent (Fig. B.1b). The sinking motions in the trough leads to relatively dry air with relative humidities between 10% and 20%. The tropopause level at the cyclone core is characterized by moist air (Fig. B.1d), that ascended from close to the surface to about 3-4 km height (Fig. B.1a,b). It will be shown later that this is diabatically generated high-PV air which connects to the stratospheric reservoir at this location.

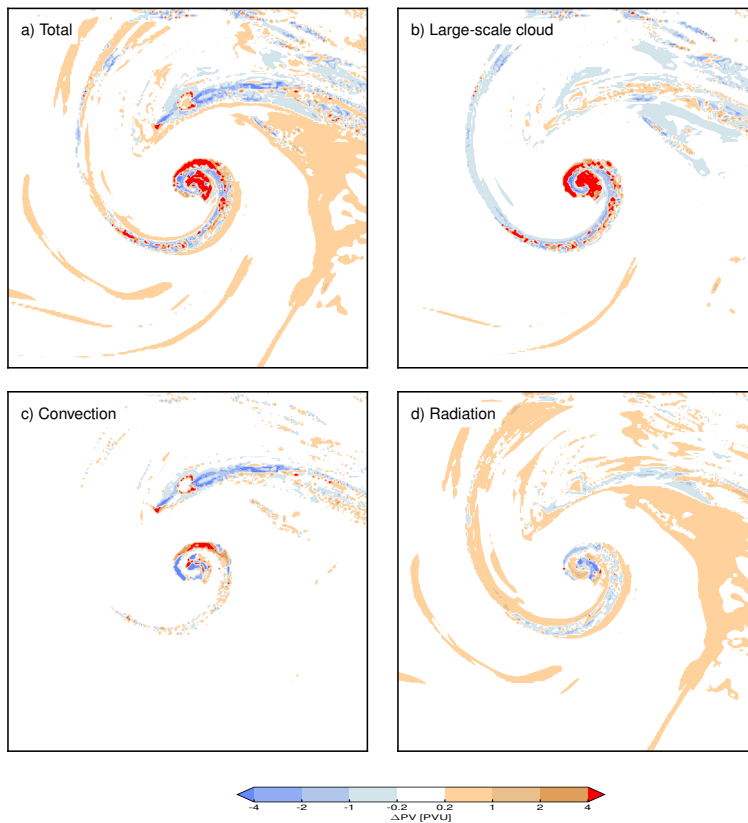


Figure B.2: Diabatic PV budgets at 03 UTC 13 December for the tropopause level shown in Fig. B.1, (a) total (b), large-scale cloud, (c) convection, (d) radiation. Note that red colors correspond to TST and blue color correspond to STT. Regions are masked as in Fig. B.1b.

**PV changes and associated STE** The total diabatic PV budget and associated STE at 03 UTC 13 December are shown in Fig. B.2a. Surrounding the cyclone center, strong TST (red) occurs in a region with a very low ( $< 4$  km) tropopause (Fig. B.1a) and high relative humidity of  $\sim 80\%$  (Fig. B.1d). To the east of the cyclone center, a larger area of weak TST (red) can be found in the ridge (Fig. B.1c). This region is moderately moist with about  $\sim 50\%$  relative humidity (Fig. B.1d). A band with STT (blue) can be found north of the cyclone center (Fig. B.2a). In this region, relative humidity is slightly higher with values between 50% and 80% (Fig. B.1d).

The TST surrounding the cyclone center is mainly due to the large-scale cloud scheme (Fig. B.2b) and to a lesser extent convection (Fig. B.2c). PV changes due to radiation (Fig. B.2d) generally oppose the PV changes due to the large-scale cloud scheme. The larger region of relatively weak STE (PV changes  $< 1$  PVU) to the east of the cyclone center (Fig. B.2a) is related to radiation (Fig. B.2d).

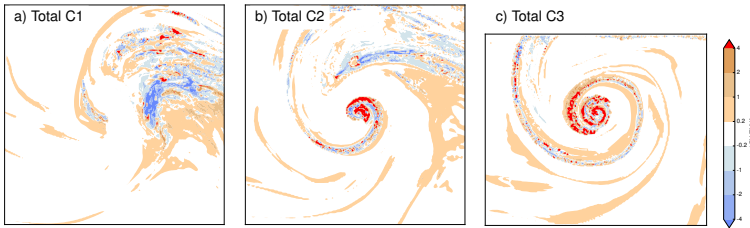


Figure B.3: Total DPV for (a) C1: 15 UTC 12 December, (b) C2: 03 UTC 13 December, (c) C3: 15 UTC 13 December.

**Time evolution of STE** The time evolution of the total diabatic PV budget at the tropopause level is shown in Fig. B.3. At 15 UTC 12 December (Fig. B.3a), both TST and STT take place in a broad area in the ridge that pushes northwards to the east of the cyclone center. In most areas, the absolute PV changes are smaller than 1 PVU. However, changes larger than 4 PVU can be found locally. As discussed above, at 03 UTC 13 December (Fig. B.3b), the strongest TST occurs close to the cyclone center, whereas STT occurs in a band to the north of the cyclone center. Another 15 hours later (Fig. B.3c) when the cyclone enters its decaying phase, TST is strong in a larger region along the spiral structure close to the cyclone center, with most activity just to the southwest of the cyclone center. STT has clearly weakened compared to the earlier stages.

**Summary** The PV budgets provide a detailed insight into the processes governing STE in the vicinity of this particularly strong cyclone. Most of our findings are consistent with the climatological study of Reutter et al. (2015) who analyzed STT and TST in cyclone-centered composites. Common findings are:

- STE occurs over the full life-cycle of the cyclone for strong cyclones
- During the intensification phase (Fig. B.3a) TST occurs downstream of the upper-level trough
- Most TST occurs to the southwest of the cyclone center in the decaying phase (Fig. B.3c)
- The pattern of TST is more axisymmetric with respect to the cyclone center when compared to the pattern of STT

In addition, here we could study the influence of the different diabatic processes on STE. It was shown that the large-scale cloud scheme is responsible for most STE, followed by convection. Radiation contributes less to STE. Further, whereas radiation acts weakly over larger areas, both convection and the large-scale cloud scheme contribute strongly but in more localized areas.

Even though the PV budgets provide insight into which processes contribute to STE in the vicinity of this particular cyclone, the accuracy of our method could be improved. A current limitation is the rather coarse vertical model resolution of around 800 m at 10 km height. This leads to errors in the trajectory positions as well as in the interpolation of variables onto the trajectories. For a more meaningful study, one would need a model having high vertical resolution around the tropopause, a sufficient temporal resolution and an output of the different physical tendencies.





# C

## ADDITIONAL FIGURES

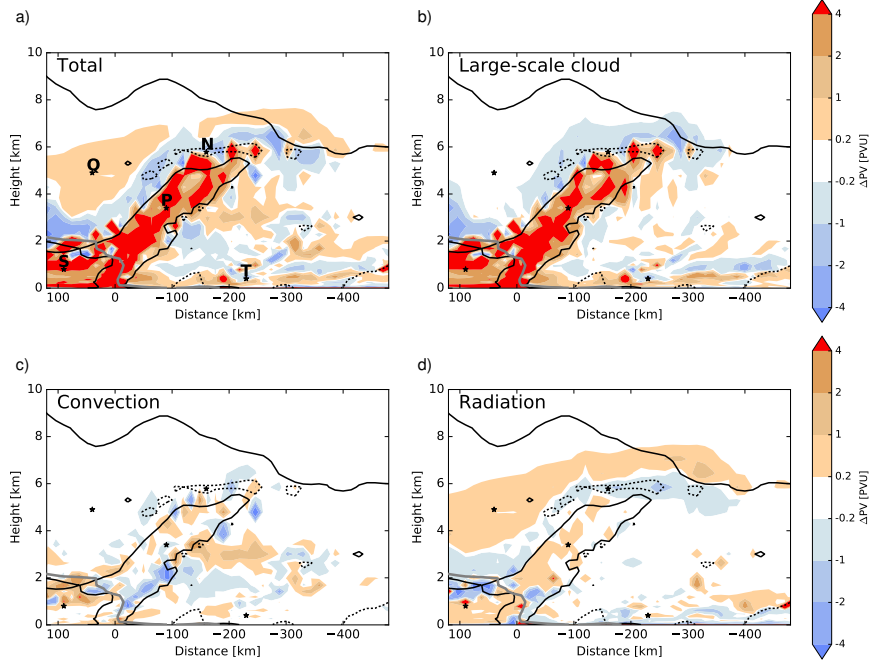


Figure C.1: A cross-section through the warm front at 15 UTC 12 December (stage C1) as shown in Fig. 4.7 showing the total DPV field (a) and its components, i.e. PV produced over the past 24 hours due to (b) large-scale cloud scheme, (c) convection scheme and (d) radiation.

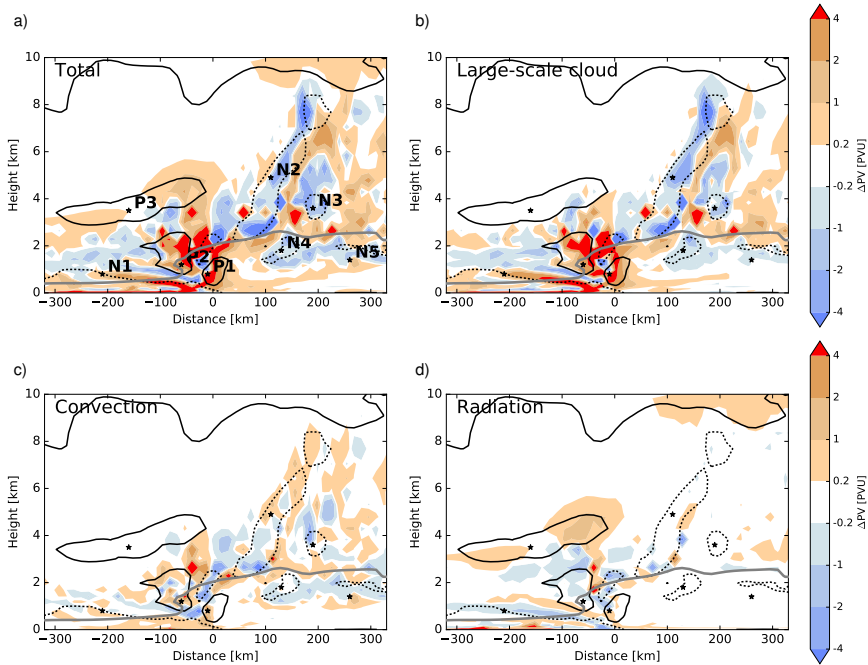


Figure C.2: A cross-section through the cold front at 15 UTC 12 December (stage C1) as shown in Fig. 4.7 showing the total DPV field (a) and its components, i.e. PV produced over the past 24 hours due to (b) large-scale cloud scheme, (c) convection scheme and (d) radiation.

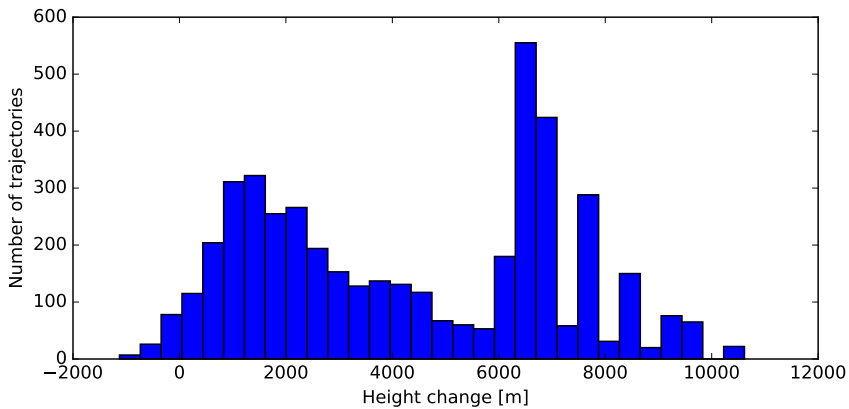


Figure C.3: Histogram showing the height change (horizontal axis) of the trajectories ending in the upper-level positive anomaly between 15 UTC 11 December and 15 UTC 12 December.

## BIBLIOGRAPHY

---

- Ahmadi-Givi, F., G. C. Graig and R. S. Plant (2004). **The dynamics of a midlatitude cyclone with very strong latent-heat release.** *Quart. J. Roy. Meteor. Soc.* 130.596, 295–323 (see pp. 6, 7).
- Anthes, R. A., Y.-H. Kuo and J. R. Gyakum (1983). **Numerical simulations of a case of explosive marine cyclogenesis.** *Mon. Wea. Rev.* 111.6, 1174–1188 (see p. 5).
- Arakawa, A. (2004). **The cumulus parameterization problem: past, present, and future.** *J. Climate* 17.13, 2493–2525 (see p. 1).
- Arakawa, A. and V. R. Lamb (1977). **Computational design of the basic dynamical processes of the UCLA general circulation model.** *Methods in computational physics* 17, 173–265 (see p. 14).
- Baehr, C., B. Pouponneau, F. Ayrault and A. Joly (1999). **Dynamical Characterization of the FASTEX cyclogenesis cases.** *Quart. J. Roy. Meteor. Soc.* 125.561, 3469–3494 (see p. 50).
- Baker, L. H., S. Gray and P. Clark (2014). **Idealised simulations of sting-jet cyclones.** *Quart. J. Roy. Meteor. Soc.* 140.678, 96–110 (see p. 26).
- Balasubramanian, G. and M. Yau (1994). **The effects of convection on a simulated marine cyclone.** *J. Atmos. Sci.* 51.16, 2397–2417 (see p. 25).
- Barth, M. C. and D. B. Parsons (1996). **Microphysical processes associated with intense frontal rainbands and the effect of evaporation and melting on frontal dynamics.** *J. Atmos. Sci.* 53.11, 1569–1586 (see p. 9).
- Bauer, P., A. Thorpe and G. Brunet (2015). **The quiet revolution of numerical weather prediction.** *Nature* 525.7567, 47–55 (see p. 1).
- Binder, H., M. Boettcher, H. Joos and H. Wernli (2016). **The role of warm conveyor belts for the intensification of extratropical cyclones in northern hemisphere winter.** *J. Atmos. Sci.* 73.10, 3997–4020 (see p. 8).
- Bjerknes, V. (1902). **Zirkulation relativ zu der Erde.** *Met. Z.* 19, 97–108 (see p. 2).
- Boutle, I. A., S. E. Belcher and R. S. Plant (2015). **Friction in mid-latitude cyclones: an Ekman-PV mechanism.** *Atmos. Sci. Lett.* 16.2, 103–109 (see p. 47).
- Browning, K. A. (2004). **The sting at the end of the tail: damaging winds associated with extratropical cyclones.** *Quart. J. Roy. Meteor. Soc.* 130.597, 375–399 (see p. 10).
- Browning, K. A., M. E. Hardman, T. W. Harrold and C. W. Pardoe (1973). **The structure of rainbands within a mid-latitude depression.** *Quart. J. Roy. Meteor. Soc.* 99.420, 215–231 (see p. 8).
- Browning, K. A., D. J. Smart, M. R. Clark and A. J. Illingworth (2015). **The role of evaporating showers in the transfer of sting-jet momentum to the surface.** *Quart. J. Roy. Meteor. Soc.* 141.693, 2956–2971 (see p. 10).
- Carlson, T. N. (1980). **Airflow through midlatitude cyclones and the comma cloud pattern.** *Mon. Wea. Rev.* 108.10, 1498–1509 (see p. 8).

- Chagnon, J. M., S. L. Gray and J. Methven (2013). **Diabatic processes modifying potential vorticity in a North Atlantic cyclone.** *Quart. J. Roy. Meteor. Soc.* 139.674, 1270–1282 (see p. 47).
- Chagnon, J. M. and S. L. Gray (2015). **A diabatically generated potential vorticity structure near the extratropical tropopause in three simulated extratropical cyclones.** *Mon. Wea. Rev.* 143.6, 2337–2347 (see p. 47).
- Charney, J. G. and M. E. Stern (1962). **On the stability of internal baroclinic jets in a rotating atmosphere.** *J. Atmos. Sci.* 19.2, 159–172 (see p. 4).
- Clark, P. A., K. A. Browning and C. Wang (2005). **The sting at the end of the tail: model diagnostics of fine-scale three-dimensional structure of the cloud head.** *Quart. J. Roy. Meteor. Soc.* 131.610, 2263–2292 (see p. 11).
- Clough, S. A. and R. A. A. Franks (1991). **The evaporation of frontal and other stratiform precipitation.** *Quart. J. Roy. Meteor. Soc.* 117.501, 1057–1080 (see pp. 8, 46).
- Clough, S. A., H. W. Lean, N. M. Roberts and R. M. Forbes (2000). **Dynamical effects of ice sublimation in a frontal wave.** *Quart. J. Roy. Meteor. Soc.* 126.568, 2405–2434 (see p. 8).
- Cooper, I. M., A. J. Thorpe and C. H. Bishop (1992). **The role of diffusive effects on potential vorticity in fronts.** *Quart. J. Roy. Meteor. Soc.* 118.506, 629–647 (see p. 33).
- Coronel, B., D. Ricard, G. Rivière and P. Arbogast (2016). **Cold-conveyor-belt jet, sting jet and slantwise circulations in idealized simulations of extratropical cyclones.** *Quart. J. Roy. Meteor. Soc.* 142.697, 1781–1796 (see p. 26).
- Coronel, B., D. Ricard, G. Rivière and P. Arbogast (2015). **Role of moist processes in the tracks of idealized midlatitude surface cyclones.** *J. Atmos. Sci.* 72.8, 2979–2996 (see pp. 2, 26, 47).
- Davies, H. C., C. Schär and H. Wernli (1991). **The palette of fronts and cyclones within a baroclinic wave development.** *J. Atmos. Sci.* 48.14, 1666–1689 (see p. 25).
- Davis, C. A. (1992a). **A potential-vorticity diagnosis of the importance of initial structure and condensational heating in observed extratropical cyclogenesis.** *Mon. Wea. Rev.* 120.11, 2409–2428 (see p. 6).
- Davis, C. A. (1992b). **Piecewise potential vorticity inversion.** *J. Atmos. Sci.* 49.16, 1397–1411 (see p. 4).
- Davis, C. A. (2010). **Simulations of subtropical cyclones in a baroclinic channel model.** *J. Atmos. Sci.* 67.9, 2871–2892 (see p. 25).
- Davis, C. A. and K. A. Emanuel (1991). **Potential vorticity diagnostics of cyclogenesis.** *Mon. Wea. Rev.* 119.8, 1929–1953 (see pp. 1, 6, 128, 129).
- Dearden, C., G. Vaughan, T. Tsai and J.-P. Chen (2016). **Exploring the diabatic role of ice microphysical processes in two North Atlantic summer cyclones.** *Mon. Wea. Rev.* 144.4, 1249–1272 (see pp. 10, 18, 46).
- Doms, G., J. Forstner, E. Heise, H.-J. Herzog, M. Raschendorfer, T. Reinhardt, B. Ritter, R. Schrodin, J.-P. Schulz and G. Vogel (2011). *"A description of the nonhydrostatic regional*

- COSMO model, part II: physical parameterization*". Tech. rep. Offenbach: Deutscher Wetterdienst, 161 (see pp. 14, 15).
- Emanuel, K. A. (1994). **Atmospheric convection**. Oxford University Press (see p. 11).
- Ertel, H. (1942). **Ein neuer hydrodynamischer Wirbelsatz**. *Meteorol. Z.* 59, 277–281 (see pp. 3, 4, 22).
- Forbes, R. M. and P. A. Clark (2003). **Sensitivity of extratropical cyclone mesoscale structure to the parametrization of ice microphysical processes**. *Quart. J. Roy. Meteor. Soc.* 129.589, 1123–1148 (see pp. 18, 47).
- Forbes, R. M. and R. J. Hogan (2006). **Observations of the depth of ice particle evaporation beneath frontal cloud to improve NWP modelling**. *Quart. J. Roy. Meteor. Soc.* 132.616, 865–883 (see pp. 9, 18).
- Gauss, M., G. Myhre, G. Pitari, M. Prather, I. Isaksen, T. Berntsen, G. P. Brasseur, F. Dentener, R. Derwent, D. Hauglustaine, et al. (2003). **Radiative forcing in the 21st century due to ozone changes in the troposphere and the lower stratosphere**. *J. Geophys. Res.* 108.D9, 4292 (see p. 141).
- Grams, C. M., H. Wernli, M. Boettcher, J. Čampa, U. Corsmeier, S. C. Jones, J. H. Keller, C.-J. Lenz and L. Wiegand (2011). **The key role of diabatic processes in modifying the upper-tropospheric wave guide: a North Atlantic case-study**. *Quart. J. Roy. Meteor. Soc.* 137.661, 2174–2193 (see p. 132).
- Gray, S. L., O. Martínez-Alvarado, L. H. Baker and P. A. Clark (2011). **Conditional symmetric instability in sting-jet storms**. *Quart. J. Roy. Meteor. Soc.* 137.659, 1482–1500 (see p. 11).
- Harrold, T. W. (1973). **Mechanisms influencing the distribution of precipitation within baroclinic disturbances**. *Quart. J. Roy. Meteor. Soc.* 99.420, 232–251 (see p. 8).
- Holton, J. R., P. H. Haynes, M. E. McIntyre, A. R. Douglass, R. B. Rood and L. Pfister (1995). **Stratosphere-troposphere exchange**. *Rev. Geophys.* 33.4, 403–439 (see p. 142).
- Hoskins, B. and P. Berrisford (1988). **A potential vorticity perspective of the storm of 15–16 October 1987**. *Weather* 43.3, 122–129 (see p. 5).
- Hoskins, B., M. McIntyre and A. Robertson (1985). **On the use and significance of isentropic potential vorticity maps**. *Quart. J. Roy. Meteor. Soc.* 111.6, 877–946 (see pp. 2, 129, 142).
- Hoskins, B. J. and N. V. West (1979). **Baroclinic waves and frontogenesis. Part II: Uniform potential vorticity jet flows-Cold and warm fronts**. *J. Atmos. Sci.* 36.9, 1663–1680 (see p. 25).
- Huang, H.-C. and K. A. Emanuel (1991). **The effects of evaporation on frontal circulations**. *J. Atmos. Sci.* 48.4, 619–628 (see pp. 9, 46).
- Huo, Z., D.-L. Zhang and J. R. Gyakum (1999). **Interaction of potential vorticity anomalies in extratropical cyclogenesis. Part I: Static piecewise inversion**. *Mon. Wea. Rev.* 127.11, 2546–2562 (see p. 6).
- Igel, A. L. and S. C. van den Heever (2014). **The role of latent heating in warm frontogenesis**. *Quart. J. Roy. Meteor. Soc.* 140.678, 139–150 (see pp. 2, 10).

- Joos, H. and H. Wernli (2012). **Influence of microphysical processes on the potential vorticity development in a warm conveyor belt: a case-study with the limited-area model COSMO.** *Quart. J. Roy. Meteor. Soc.* 138.663, 407–418 (see pp. 2, 9, 131).
- Kentarchos, A. S. and G. J. Roelofs (2003). **A model study of stratospheric ozone in the troposphere and its contribution to tropospheric OH formation.** *J. Geophys. Res.* 108.D12, 8517 (see p. 141).
- Kleinschmidt, E. (1957). **Dynamic meteorology.** In: *Handbuch der Physik.* Ed. by S. Flügge and J. Bartels. Springer, 1–145 (see pp. 4, 5).
- Kuo, Y.-H., M. A. Shapiro and E. G. Donall (1991). **The interaction between baroclinic and diabatic processes in a numerical simulation of a rapidly intensifying extratropical marine cyclone.** *Mon. Wea. Rev.* 119.2, 368–384 (see p. 6).
- Madonna, E., H. Wernli, H. Joos and O. Martius (2014). **Warm Conveyor Belts in the ERA-Interim Dataset (1979–2010). Part I: Climatology and Potential Vorticity Evolution.** *J. Climate* 27.1, 3–26 (see pp. 8, 132, 133).
- Manabe, S. (1956). **On the contribution of heat released by condensation to the change in pressure pattern.** *J. Meteor. Soc. Japan* 34, 308–320 (see p. 5).
- Marecal, V. and Y. Lemaitre (1995). **Importance of microphysical processes in the dynamics of a CSI mesoscale frontal cloud band.** *Quart. J. Roy. Meteor. Soc.* 121.522, 301–318 (see p. 46).
- Martínez-Alvarado, O., S. L. Gray, J. L. Catto and P. A. Clark (2012). **Sting jets in intense winter north-atlantic windstorms.** *Environ. Res. Lett.* 7.2, 024014 (see p. 11).
- Martínez-Alvarado, O., F. Weidle and S. L. Gray (2010). **Sting jets in simulations of a real cyclone by two mesoscale models.** *Mon. Wea. Rev.* 138.11, 4054–4075 (see p. 10).
- Methven, J. (2015). **Potential vorticity in warm conveyor belt outflow.** *Quart. J. Roy. Meteor. Soc.* 141.689, 1065–1071 (see pp. 132, 133).
- Montgomery, M. T. and B. F. Farrell (1991). **Moist surface frontogenesis associated with interior potential vorticity anomalies in a semigeostrophic model.** *J. Atmos. Sci.* 48.2, 343–368 (see p. 6).
- Moore, R. W. and M. T. Montgomery (2005). **Analysis of an idealized, three-dimensional diabatic rossby vortex: a coherent structure of the moist baroclinic atmosphere.** *J. Atmos. Sci.* 62.8, 2703–2725 (see p. 25).
- Neiman, P. J., M. A. Shapiro and L. S. Fedor (1993). **The life cycle of an extratropical marine cyclone. Part II: mesoscale structure and diagnostics.** *Mon. Wea. Rev.* 121.8, 2177–2199 (see p. 6).
- Parker, D. J. and A. J. Thorpe (1995). **The role of snow sublimation in frontogenesis.** *Quart. J. Roy. Meteor. Soc.* 121.524, 763–782 (see pp. 8, 45, 46).
- Persson, P. O. G. (1995). **Simulations of the potential vorticity structure and budget of FRONTS 87 IOP8.** *Quart. J. Roy. Meteor. Soc.* 121.525, 1041–1081 (see p. 132).

- Pinto, J. G., S. Zacharias, A. H. Fink, G. C. Leckebusch and U. Ulbrich (2009). **Factors contributing to the development of extreme North Atlantic cyclones and their relationship with the NAO.** *Climate Dynam.* 32.5, 711–737 (see p. 50).
- Pomroy, H. R. and A. J. Thorpe (2000). **The evolution and dynamical role of reduced upper-tropospheric potential vorticity in intensive observing period one of FASTEX.** *Mon. Wea. Rev.* 128.6, 1817–1834 (see p. 132).
- Reed, R. J., M. T. Stoelinga and Y.-H. Kuo (1992). **A model-aided study of the origin and evolution of the anomalously high potential vorticity in the inner region of a rapidly deepening marine cyclone.** *Mon. Wea. Rev.* 120.6, 893–913 (see p. 7).
- Reutter, P., B. Škerlak, M. Sprenger and H. Wernli (2015). **Stratosphere–troposphere exchange (STE) in the vicinity of North Atlantic cyclones.** *Atmos. Chem. Phys.* 15.19, 10939–10953 (see pp. 141, 145).
- Ritter, B. and J.-F. Geleyn (1992). **A comprehensive radiation scheme for numerical weather prediction models with potential applications in climate simulations.** *Mon. Wea. Rev.* 120.2, 303–325 (see p. 20).
- Rivière, G. and A. Joly (2006). **Role of the Low-Frequency Deformation Field on the Explosive Growth of Extratropical Cyclones at the Jet Exit. Part I: Barotropic Critical Region.** *J. Atmos. Sci.* 63.8, 1965–1981 (see p. 50).
- Roach, W. T. and M. E. Hardman (1975). **Mesoscale air motions derived from wind finding dropsonde data: The warm front and rainbands of 18 January 1971.** *Quart. J. Roy. Meteor. Soc.* 101.429, 437–462 (see p. 72).
- Rodwell, M. J. and B. J. Hoskins (1995). **A model of the Asian summer monsoon. Part II: Cross-equatorial flow and PV behavior.** *J. Atmos. Sci.* 52.9, 1341–1356 (see p. 22).
- Roelofs, G. J. and J. Lelieveld (1997). **Model study of the influence of cross-tropopause O<sub>3</sub> transports on tropospheric O<sub>3</sub> levels.** *Tellus B* 49.1, 38–55 (see p. 141).
- Rossa, A. M., H. Wernli and H. C. Davies (2000). **Growth and decay of an extra-tropical cyclone's PV-tower.** *Meteor. Atmos. Phys.* 73.3-4, 139–156 (see p. 7).
- Rossby, C. G. (1937). **Isentropic analysis.** *Bull. Am. Meteorol. Soc.* 18, 201–203 (see p. 132).
- (1940). **Planetary flow patterns in the atmosphere.** *Quart. J. Roy. Meteor. Soc.* 66, 68–87 (see p. 2).
- Sanders, F. and J. R. Gyakum (1980). **Synoptic-dynamic climatology of the “bomb”.** *Mon. Wea. Rev.* 108.10, 1589–1606 (see p. 55).
- Schemm, S. and H. Wernli (2014). **The linkage between the warm and the cold conveyor belts in an idealized extratropical cyclone.** *J. Atmos. Sci.* 71.4, 1443–1459 (see p. 26).
- Schemm, S., H. Wernli and L. Papritz (2013). **Warm conveyor belts in idealized moist baroclinic wave simulations.** *J. Atmos. Sci.* 70.2, 627–652 (see pp. 13, 26, 27, 30).
- Schultz, D. M. and J. M. Sienkiewicz (2013). **Using frontogenesis to identify sting jets in extratropical cyclones.** *Weather and Forecasting* 28.3, 603–613 (see p. 10).

- Shapiro, M. A. and D. A. Keyser (1990). **Fronts, jet streams, and the tropopause.** In: *Extratropical Cyclones: The Erik Palmén Memorial Volume*. Ed. by C. W. Newton and E. O. Holopainen. Amer. Meteor. Soc., 167–191 (see pp. 10, 29).
- Simmons, A. J. and A. Hollingsworth (2002). **Some aspects of the improvement in skill of numerical weather prediction.** *Quart. J. Roy. Meteor. Soc.* 128.580, 647–677 (see p. 1).
- Simmons, A. J. and B. J. Hoskins (1979). **The downstream and upstream development of unstable baroclinic waves.** *J. Atmos. Sci.* 36.7, 1239–1254 (see p. 25).
- Škerlak, B., M. Sprenger and H. Wernli (2014). **A global climatology of stratosphere–troposphere exchange using the ERA-Interim data set from 1979 to 2011.** *Atmos. Chem. Phys.* 14.2, 913–937 (see pp. 141, 142).
- Snyder, C. and R. S. Lindzen (1991). **Quasi-geostrophic wave-CISK in an unbounded baroclinic shear.** *J. Atmos. Sci.* 48.1, 76–86 (see p. 5).
- Sprenger, M. and H. Wernli (2015). **The LAGRANTO Lagrangian analysis tool – version 2.0.** *Geoscientific Model Development* 8.8, 2569–2586 (see pp. 20, 21).
- Stappeler, J., G. Doms, U. Schättler, H. W. Bitzer, A. Gassmann, U. Damrath and G. Gregoric (2003). **Meso-gamma scale forecasts using the nonhydrostatic model LM.** *Meteor. Atmos. Phys.* 82.1-4, 75–96 (see p. 13).
- Stoelinga, M. T. (1996). **A potential vorticity-based study of the role of diabatic heating and friction in a numerically simulated baroclinic cyclone.** *Mon. Wea. Rev.* 124.5, 849–874 (see p. 7).
- Szeto, K. K., C. A. Lin and R. E. Stewart (1988a). **Mesoscale circulations forced by melting snow. Part I: basic simulations and dynamics.** *J. Atmos. Sci.* 45.11, 1629–1641 (see pp. 9, 46).
- Szeto, K. K., R. E. Stewart and C. A. Lin (1988b). **Mesoscale circulations forced by melting snow. Part II: application to meteorological features.** *J. Atmos. Sci.* 45.11, 1642–1650 (see p. 9).
- Terpstra, A., T. Spengler and R. W. Moore (2015). **Idealised simulations of polar low development in an arctic moist-baroclinic environment.** *Quart. J. Roy. Meteor. Soc.* 141.691, 1987–1996 (see p. 26).
- Thorncroft, C. D., B. J. Hoskins and M. E. McIntyre (1993). **Two paradigms of baroclinic-wave life-cycle behaviour.** *Quart. J. Roy. Meteor. Soc.* 119, 17–55 (see pp. 25, 50, 144).
- Thorpe, A. J. and S. A. Clough (1991). **Mesoscale dynamics of cold fronts: structures described by dropsoundings in FRONTS 87.** *Quart. J. Roy. Meteor. Soc.* 117.501, 903–941 (see p. 72).
- Tiedtke, M. (1989). **A comprehensive mass flux scheme for cumulus parameterization in large-scale models.** *Mon. Wea. Rev.* 117.8, 1779–1800 (see p. 20).
- Uccellini, L. W. (1990). **Processes contributing to the rapid development of extratropical cyclones.** In: *Extratropical Cyclones: The Erik Palmén Memorial Volume*. Ed. by C. W. Newton and E. O. Holopainen. Amer. Meteor. Soc., 81–105 (see p. 2).



- Wernli, H. (1997). **A Lagrangian-based analysis of extratropical cyclones. II: a detailed case-study.** *Quart. J. Roy. Meteor. Soc.* 123.542, 1677–1706 (see p. 8).
- Wernli, H. and H. C. Davies (1997). **A Lagrangian-based analysis of extratropical cyclones. I: the method and some applications.** *Quart. J. Roy. Meteor. Soc.* 123.538, 467–489 (see p. 132).
- Wernli, H., S. Dirren, M. A. Liniger and M. Zillig (2002). **Dynamical aspects of the life cycle of the winter storm "Lothar" (24–26 December 1999).** *Quart. J. Roy. Meteor. Soc.* 128.580, 405–429 (see pp. 7, 50).
- Whitaker, J. S. and C. A. Davis (1994). **Cyclogenesis in a saturated environment.** *J. Atmos. Sci.* 51.6, 889–908 (see p. 25).
- Whitaker, J. S., L. W. Uccellini and K. F. Brill (1988). **A model-based diagnostic study of the rapid development phase of the Presidents' Day cyclone.** *Mon. Wea. Rev.* 116.11, 2337–2365 (see p. 5).



# ACKNOWLEDGEMENTS

---

I enjoyed the help, support and accompany of many people while doing my PhD. Specifically I want to thank Heini Wernli for giving me the opportunity to do this PhD and guide me so well during the project. The meetings we had were always very motivating, and I value a lot the great freedom you gave me during my project. I was lucky to have Hanna as my supervisor, it was great how you always managed to motivate me, and our meetings were very helpful and motivating. Many thanks to the technical support from Michael Sprenger and Nicolas Piaget with the Dyntools and Dypy libraries that I used a lot. I acknowledge the Swiss National Science Foundation (Project 200020\_146834) for funding my project, MeteoSwiss for providing the COSMO model, and ECMWF for providing the ECMWF analysis data. Thanks to Nick Pullen for providing the  $\LaTeX$ template (<https://github.com/nstjhp/thesisFinal>) that I used. I appreciated the help provided by Sebastian Schemm with the baroclinic channel model. Thanks to Maxi Boettcher for the valuable discussions we had.

Many thanks to my great office mates Franziska, Marina, Alex, Remo and Raphael, for creating a great (working) atmosphere. And thanks to all my (former) colleagues, it was great to share with you our enthusiasm for the weather and have spontaneous discussions.

During my time in Zurich, I happily lived in a "WG" with Nicky, Philipp, Vera, Silvan and Helen, thanks to you for the pleasant and warm atmosphere at home. Further I enjoyed a lot the activities with friends in Zurich and the support from my friends in the Netherlands: "de Natuurko's", "137", "de Lichte 8+ 2009", "L.H.D. Vanir" and "USKO". Of particular importance for me, was the support from my family, my parents, my sister and from Laure, for always being there for me. Mici!



# CURRICULUM VITAE

---

## **Bas Crezee**

born on 24 February 1988 in Rotterdam, The Netherlands

### **Education and working experience**

- 09/2013 – 05/2017    PhD in Atmospheric Sciences  
Institute for Atmospheric and Climate Science (IAC)  
ETH Zurich, Switzerland
- 12/2012 – 07/2013    Research internship  
Geophysical Institute  
University of Bergen, Norway
- 09/2011 – 09/2013    Master in Physics and Climate Science  
Utrecht University, The Netherlands
- 09/2006 – 12/2009    Bachelor studies in Physics and Astronomy  
Leiden University, The Netherlands
- 08/2000 – 08/2006    Gymnasium & Bilingual education, Penta College C.S.G.  
Jacob van Liesveldt, Hellevoetsluis, The Netherlands

### **Teaching assistant at IAC**

- 2015–2016    Radiation and Climate Change (M. Wild)
- 2014    Inter-annual variability and prediction (C. Appenzeller)
- 2013–2015    Dynamics of large-scale atmospheric flow (H. Wernli)

### **Conferences and workshops**

- 06/2016    Young Researchers Meeting, Aeschi, Switzerland
- 04/2016    European Geosciences Union (EGU) General Assembly, Vienna, Austria
- 10/2015    Cyclone Workshop, Monterey, USA
- 06/2015    International Union of Geodesy and Geophysics (IUGG) General  
Assembly, Prague, Czech Republic
- 06/2015    Young Researchers Meeting, Aeschi, Switzerland
- 05/2015    PANDOWAE Final Symposium, Karlsruhe, Germany

- 11/2014 Swiss Meteorological Society Annual Meeting, Zurich, Switzerland
- 08/2014 WWRP Open Science Conference, Montreal, Canada
- 06/2014 Latsis Symposium, Zurich, Switzerland
- 03/2014 COSMO User Seminar, Offenbach, Germany

### **Student supervision**

André Piquerez (MSc): *What determines the ascent of a warm conveyor belt – Sensitivity experiments with the ECMWF global model*, co-supervisors: M. Böttcher and H. Wernli, May 2015.

Yasmin Roskopf (MSc): *A high-resolution numerical case study of mesocyclones associated with a cold air outbreak in the Ross Sea, 24-28 June 2010*, co-supervisors: L. Papritz and H. Wernli, April 2015.

Raphael Portmann (MSc): *The fate of stratospheric PV cutoffs*, co-supervisors: J. Quinting and H. Wernli, March 2016.

Sebastian Mooser (BSc), *Der Vergleich dreier unterschiedlicher Simulationen des Warm Conveyor Belt im Baroclinic Channel*, co-supervisor: Hanna Joos, Aug 2016.

### **Publications**

Crezee, B., H. Joos and H. Wernli, 2017. The microphysical building blocks of low-level potential vorticity anomalies in an idealized extratropical cyclone. *J. Atmos. Sci.* 74.5, 1402-1416.

Crezee, B., H. Joos, H. Wernli, 2017. The microphysical building blocks of low-level potential vorticity anomalies in a strong maritime extratropical cyclone, in preparation

Portmann, R., B. Crezee, J. Quinting, H. Wernli, 2017, The life cycle of two long lived PV cutoffs over Europe, in preparation

Quinting, J.F., B. Crezee, H. Wernli, 2017. On the direct and indirect role of diabatic processes in upper-level PV frontogenesis, in preparation